AD-A174 599 ACTA AERODYNAMICA SINICA(U) FOREIGN TECHNOLOGY DIV 1/3
WRIGHT-PATTERSON AFB OH Z HANXIN ET AL 03 NOV 86
FTD-ID(RS)T-0367-86

UNCLASSIFIED F/G 20/4 NL

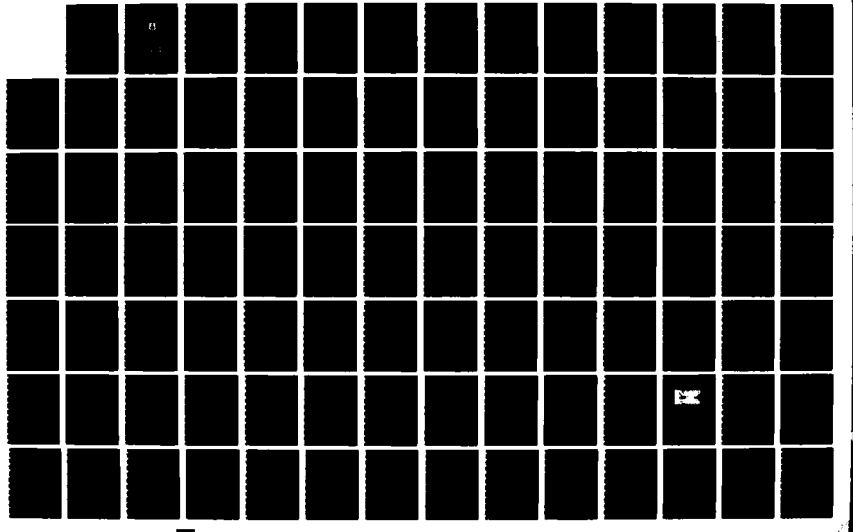

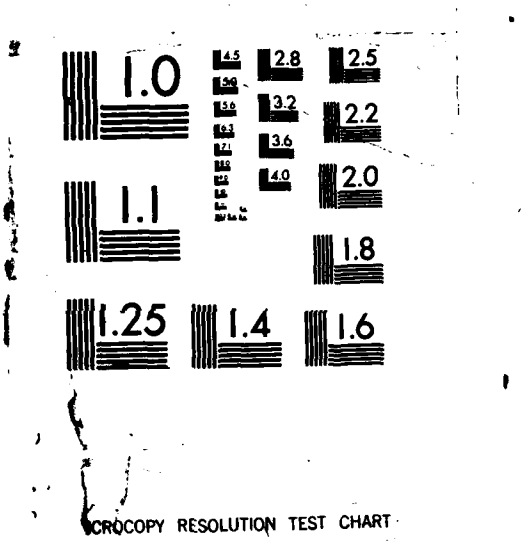
1.0
1.1
1.25
1.4
1.6
1.8
2.0
2.2
2.5
2.8
3.2
3.6
4.0
4.5
5.0
5.6
6.3
7.1
8.0
9.0
CROCOPY RESOLUTION TEST CHART

(2)

AD-A174 599

FTD-ID(RS)T-0367-86

FOREIGN TECHNOLOGY DIVISION

ACTA AERODYNAMICA SINICA

DTIC
ELECTE
DEC 2 1986
S D
B

DTIC FILE COPY

Approved for public release;
Distribution unlimited.

86 12 02 005

HUMAN TRANSLATION

FTD-ID(RS)T-0367-86 3 November 1986

MICROFICHE NR: FTD-86-C-002339

ACTA AERODYNAMICA SINICA

English pages: 262

Source: Konggi Donglixue Xuebao, Vol. 3, Nr. 1, 1985, pp. 1-116

Country of origin: China
Translated by: SCITRAN
F33657-84-D-0165
Requester: FTD/TQTA

PREPARED BY:

TRANSLATION DIVISION
FOREIGN TECHNOLOGY DIVISION
WPAFB, OHIO.

Partial contents:

Table of Contents

GRAPHICS DISCLAIMER

All figures, graphics, tables, equations, etc. merged into this translation were extracted from the best quality copy available.

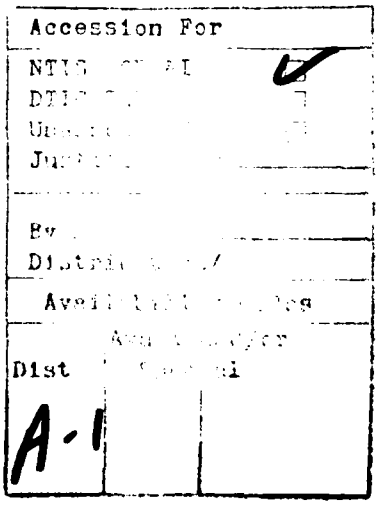

Separation Criteria for Three Dimensional Steady Viscous Flow and Flow Behavior Near Separation Line /1

Zhang Hanxin

(China Aerodynamic Research and Development Center)

Abstract

The separation criteria for a three-dimensional steady viscous flow are given in this paper. The flow behavior near the separation line was investigated. It is pointed out that for any flow described by NS equations, the separation line is the "convergent asymptotic line" of the wall limiting streamline. Moreover,it, itself, is also the limiting streamline. The beginning and end of the separation line were also studied in this work. It is pointed out that either an open or closed type separation line[1] extends towards infinity from the beginning and ends at a focal point or a node. It cannot end at a saddle point. Corresponding conclusions were also obtained for the attachment line. Finally, a method to determine the position of the line of separation is discussed.

I. Introduction

It is of important significance to study the separation of flow of a viscous gas for the design of aircrafts, guided missiles and hypersonic flying vehicles. One of the important

issues is to determine the beginning of separation and the position of the boundary of the separation region. This is the so-called separation criteria and separation line characteristics. With regard to this problem, there are many theories, experimental studies[1,2,3] and comprehensive reviews[4,5]. Nevertheless, just as Brown and Stewartson[4] and Williams[5] stress, an agreement has not yet been reached in this area. Eichelbrenner and Oudart[6], Maskell[1], and Wang Guozhang[3] believed that the separation line is an envelope of the wall limiting streamline. Legendre[7], Lighthill[2], Hunt[8], and Tobak and Peake[9-11] believed, however, that the separation line is a "convergent asymptotic line" of the neighboring wall limiting streamline. Moreover, it, itself, is also a limiting streamline.

In this paper, an attempt is made to clarify this problem based on theoretical considerations. Through studying the separation flow, the criteria for the separation of three-dimensional steady viscous flow are established. On this basis, the flow behavior near the separation line is analyzed. In addition, we will prove that the separation line is a convergent asymptotic line of its neighboring limiting streamline. Moreover, it, itself, is also a limiting streamline. Similar conclusions are obtained for attachment. In the paper, the beginning and development of the separation line, as well as the method to determine its position are also discussed.

II. Criteria for Flow Separation

When studying the separation of a three-dimensional steady flow on a fixed wall, Figure 1 is often used to explain the geometric significance of the separation line in the literature: (1) the separation line is the intersect of the separated flow surface and the object surface. (2) Fluids on both

Manuscript received on October 12, 1984

sides flow over the object, just as the separation flow surface. /2 The criteria for separation are established in the following based on this sense.

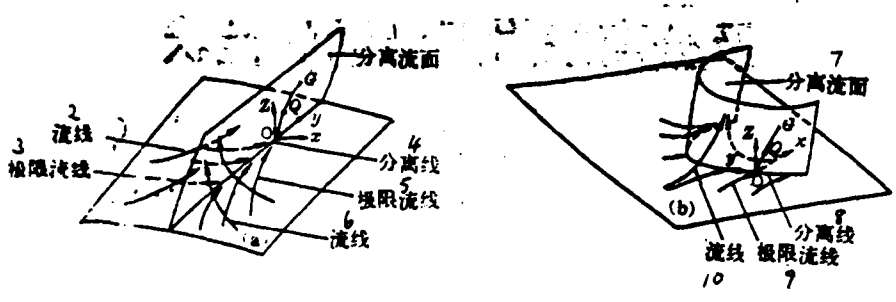

Figure 1. Separation Picture and Coordinate System

1. separation flow surface
2. streamline
3. limiting streamline
4. separation line
5. limiting streamline
6. streamline
7. separation flow surface
8. separation line
9. limiting streamline
10. streamline

1. Conditions for Separation Flow to Depart From Surface

Let us assume that x, y, z is an orthogonal coordinate where x and y axes are on the surface of the object and z-axis is in the normal direction. The corresonding scale indices are $h_1=h_1(x,y,z)$, $h_2=h_2(x,y,z)$ and $h_3=1$. It is also assumed that the equation of the separation flow surface is: $z=f(x,y)$, or

$$F(x,y,z)=z-f(x,y)=0 \tag{2.1}$$

Then, the unit normal vector of the separation flow is

$$\vec{n}=\frac{-\frac{1}{h_1}\frac{\partial f}{\partial x}\vec{e}_x-\frac{1}{h_2}\frac{\partial f}{\partial y}\vec{e}_y+\vec{e}_z}{\left[1+\left(\frac{1}{h_1}\frac{\partial f}{\partial x}\right)^2+\left(\frac{1}{h_2}\frac{\partial f}{\partial y}\right)^2\right]^{\frac{1}{2}}} \tag{2.2}$$

where $\vec{e}_x$, $\vec{e}_y$, $\vec{e}_z$ are unit vectors of the x, y, z axes. Furthermore, let us assume the velocity of the fluid is:

$$\vec{V}=u\vec{e}_x+v\vec{e}_y+w\vec{e}_z \tag{2.3}$$

Here, u, v, w represent the velocity components in x, y, z direction. Due to the fact that $\vec{V}$ intersects with the flow surface everywhere, therefore, $\vec{V}\cdot\vec{n}=0$. Based on equation (2.2) and (2.3), we get

$$\frac{1}{h_1}\frac{\partial f}{\partial x}=\frac{w-\frac{v}{h_2}\frac{\partial f}{\partial y}}{u} \tag{2.4}$$

On the other hand, the angle θ between the normal direction of the separation flow $\vec{n}$ and $\vec{e}_x$ is:

$$\cos\theta=\vec{n}\cdot\vec{e}_x=\left[1+\left(\frac{1}{h_1}\frac{\partial f}{\partial x}\right)^2+\left(\frac{1}{h_2}\frac{\partial f}{\partial y}\right)^2\right]^{-\frac{1}{2}}$$

We get

$$\left[\operatorname{tg}^2\theta-\left(\frac{1}{h_2}\frac{\partial f}{\partial y}\right)^2\right]^{\frac{1}{2}}=\frac{1}{h_1}\frac{\partial f}{\partial x} \tag{2.5}*$$

---

*Here, we only take the positive sign. The positive x direction points from the attached side to the separated side.

By substituting equation (2.4) into it, we get /3

$$\left[\operatorname{tg}^2\theta-\left(\frac{1}{h_2}\frac{\partial f}{\partial y}\right)^2\right]^{\frac{1}{2}}=\frac{w-\frac{v}{h_2}\frac{\partial f}{\partial y}}{u} \tag{2.6}$$

This is the equation determining the angle between the flow normal direction and the object normal direction. Now, let the separation line be the y axis (See Figure 1). It is necessary for $(\vec{n}.\vec{e}_y)_0=0$. The subscript "0" represents the values taken on the separation line. By using equation (2.2), we get

$$\left(\frac{1}{h_2}\frac{\partial f}{\partial y}\right)_0=0 \tag{2.7}$$

This is the geometry of the separation flow surface at the separation line.

Equation (2.6) is valid at any point on the separation flow surface outside the separation line. Let o be any point on the separation line. As shown in Figure 1, let OG be the intersect of the coordinate surface xoz and the separation flow surface and

Q be a point on it. Let us assume that the arc length of OQ is Δs. Let us study the limiting form of equation (2.6) when $\Delta s \to 0$. Under separation conditions, the flow surface suddenly lifts up from the object at the separation line. Hence, $(tg\theta)_0 \neq 0$. $(tg\theta)_0$ is obtained by using equation (2.7) and the left side of equation (2.6). However, due to the fact that there is no slipping on the object surface, the right side of equation (2.6) belongs to the "0/0" type. Thus, we get the following by L'Hospital method:

$$(tg\,\theta)_0 = \frac{\left(\frac{\partial w}{\partial s}\right)_0 - \left(\frac{\partial v}{\partial s}\right)_0 \left(\frac{1}{h_2}\frac{\partial f}{\partial y}\right)_0 - v_0\left[\frac{\partial}{\partial s}\left(\frac{1}{h_2}\frac{\partial f}{\partial y}\right)\right]_0}{\left(\frac{\partial u}{\partial s}\right)_0}$$

where

$$\left(\frac{\partial}{\partial s}\right)_0 = \left(\frac{\partial x}{\partial s}\right)_0 \left(\frac{\partial}{\partial x} + \frac{\partial z}{\partial x}\frac{\partial}{\partial z}\right)_0$$

represents the derivative in OG direction. Because Q is on OG, $(\partial z/\partial x)_0 = (h_1 tg\theta)_0$. Thus, the above equation becomes

$$\begin{aligned}(tg\,\theta)_0 = \Bigg\{ &\left(\frac{\partial w}{\partial x}\right)_0 + (h_1\,tg\,\theta)_0 \left(\frac{\partial w}{\partial z}\right)_0 - \left[\left(\frac{\partial v}{\partial x}\right)_0 + (h_1\,tg\,\theta)_0 \left(\frac{\partial v}{\partial z}\right)_0\right]\left(\frac{1}{h_2}\frac{\partial f}{\partial y}\right)_0 \\ &- v_0\left[\frac{\partial}{\partial x}\left(\frac{1}{h_2}\frac{\partial f}{\partial y}\right) + h_1\,tg\,\theta\,\frac{\partial}{\partial z}\left(\frac{1}{h_2}\frac{\partial f}{\partial y}\right)\right]_0\Bigg\} \\ &\times\left[\left(\frac{\partial u}{\partial x}\right)_0 + (h_1\,tg\,\theta)_0\left(\frac{\partial u}{\partial z}\right)_0\right]^{-1}\end{aligned} \tag{2.8}$$

Using the surface condition $u_0 = v_0 = w_0 = 0$, we get

$$\left(\frac{\partial u}{\partial x}\right)_0 = \left(\frac{\partial v}{\partial x}\right)_0 = \left(\frac{\partial w}{\partial x}\right)_0 = 0$$

Furthermore, based on the continuity equation we know that

$$\left(\frac{\partial w}{\partial z}\right)_0 = -\left\{\frac{1}{\rho h_1 h_2}\left[\frac{\partial(\rho h_2 u)}{\partial x} + \frac{\partial(\rho h_1 v)}{\partial y} + w\frac{\partial(\rho h_1 h_2)}{\partial z}\right]\right\}_0 = 0$$

Here, ρ is the density of the fluid. It is easy to find out from /4 equation (2.7) that the numerator of the right hand side of equation (2.8) is zero. Hence, it is required that $(tg\theta)_0$ should not be zero. Hence

$$\left(\frac{\partial u}{\partial z}\right)_0 = 0 \tag{2.9}$$

The expression for $(tg\theta)_0$ is further studied in the following. The origin of the coordinate can be chosen at o without losing generality because the actual flow described by NS equations has no Goldstein[12] singularity at the separation line. Therefore, u, v, w can be expressed by using Taylor series expansion near 0.

$$\begin{cases} u = \frac{1}{2}\left(\frac{\partial^2 u}{\partial z^2}\right)_0 z^2 + \left(\frac{\partial^2 u}{\partial x\,\partial z}\right)_0 xz + \cdots \\ v = \left(\frac{\partial v}{\partial z}\right)_0 z + \frac{1}{2}\left(\frac{\partial^2 v}{\partial z^2}\right)_0 z^2 + \left(\frac{\partial^2 v}{\partial y \partial z}\right)_0 yz + \left(\frac{\partial^2 v}{\partial x \partial z}\right)_0 xz + \cdots \\ w = \frac{1}{2}\left(\frac{\partial^2 w}{\partial z^2}\right)_0 z^2 + \cdots \end{cases} \tag{2.10}$$

Here, the surface condition, equation (2.9) and $(\partial w/\partial z)_0 = 0$ are utilized. In addition, f(x,y) and h_2 can also be expanded as:

$$f(x,y) = \left(\frac{\partial f}{\partial x}\right)_0 x + \left(\frac{\partial^2 f}{\partial x \partial y}\right)_0 xy + \frac{1}{2}\left(\frac{\partial^2 f}{\partial x^2}\right)_0 x^2 + \cdots \tag{2.11}$$

$$h_1 = (h_1)_0 + \left(\frac{\partial h_1}{\partial x}\right)_0 x + \left(\frac{\partial h_1}{\partial y}\right)_0 y + \left(\frac{\partial h_1}{\partial z}\right)_0 z + \cdots \tag{2.12}$$

In the derivation of equation (2.11), equation (2.7) was applied. By substituting equations (2.10)-(2.12) into equation (2.6), we

get the following after some re-arrangement.

$$(\mathrm{tg}\,\theta)_0 = \frac{\left(\frac{\partial^2 w}{\partial z^2}\right)_0 - 2\left(\frac{\partial v}{\partial z}\right)_0 \left(\frac{1}{h_1}\frac{\partial^2 f}{\partial x \partial y}\right)_0 \frac{x}{z}}{\left(\frac{\partial^2 u}{\partial z^2}\right)_0 + 2\left(\frac{\partial^2 u}{\partial x \partial z}\right)_0 \frac{x}{z}} \tag{2.13}$$

where z=f(x,y). Based on equation (2.11) and (2.5), we get

$$\frac{f(x,y)}{x} = \left(\frac{\partial f}{\partial x}\right)_0 + \cdots \tag{2.14}$$

$$\left(\frac{\partial f}{\partial x}\right)_0 = (h_1\,\mathrm{tg}\,\theta)_0 \tag{2.15}$$

$$\left(\frac{\partial^2 f}{\partial x \partial y}\right)_0 = \left[\frac{\partial}{\partial y}(h_1\,\mathrm{tg}\,\theta)\right]_0 \tag{2.16}$$

By substituting equation (2.15) into (2.14) and followed by substituting the result together with equation (2.16) into equation (2.13) and then letting x, y, z approach zero, we get

$$2\left(\frac{\partial v}{\partial z}\right)_0 \left(\frac{h_1}{h_2}\right)_0 \frac{\partial (h_1\,\mathrm{tg}\,\theta)_0}{\partial y} + \left[2\left(\frac{\partial^2 u}{\partial x \partial z}\right)_0 - \left(h_1 \frac{\partial^2 w}{\partial z^2}\right)_0\right](h_1\,\mathrm{tg}\,\theta)_0^{\cdot} + \\ + \left(\frac{\partial^2 u}{\partial z^2}\right)_0 (h_1\,\mathrm{tg}\,\theta)_0^2 = 0 \tag{2.17}$$

Because the origin o is arbitrarily chosen, this equation is valid at any point on the separation line. Thus, the equation to determine $\mathrm{tg}\theta_0$ is obtained. For a Newtonian fluid, based on NS equations, Newtonian laws, surface conditions and equation (2.9), we have

/5

$$\begin{cases} \left(\frac{\partial^2 u}{\partial z^2}\right)_0 = \left(\frac{1}{\mu}\ \frac{1}{h_1}\ \frac{\partial p}{\partial x}\right)_0 \\ \left(\frac{\partial^2 w}{\partial z^2}\right)_0 = \left(\frac{1}{\mu}\ \frac{\partial p}{\partial z}\right)_0 \\ \left(\frac{\partial^2 u}{\partial x \partial z}\right)_0 = \left(\frac{1}{\mu}\ \frac{\partial \tau_{zx}}{\partial x}\right)_0 \end{cases} \tag{2.18}$$

Here, μ is the viscosity index, p is pressure τ_{zx} is the normal component of the surface friction stress with respect to the separation line. By introducing

$$\begin{cases} f(y) = \dfrac{\left(\frac{\partial^2 u}{\partial z^2}\right)_0}{2\left(\frac{\partial v}{\partial z}\right)_0\left(\frac{h_1}{h_1}\right)_0} = \dfrac{\left(\frac{1}{\mu}\ \frac{1}{h_1}\ \frac{\partial p}{\partial x}\right)_0}{2\left(\frac{h_1}{h_2}\right)_0\left(\frac{\partial v}{\partial z}\right)_0} \\ g(y) = \dfrac{2\left(\frac{\partial^2 u}{\partial x \partial z}\right)_0 - \left(h_1 \frac{\partial^2 w}{\partial z^2}\right)_0}{2\left(\frac{\partial v}{\partial z}\right)_0\left(\frac{h_1}{h_2}\right)_0} = \dfrac{2\left(\frac{1}{\mu}\ \frac{\partial \tau_{zx}}{\partial x}\right)_0 - \left(h_1 \frac{1}{\mu}\ \frac{\partial p}{\partial z}\right)_0}{2\left(\frac{h_1}{h_2}\right)_0\left(\frac{\partial v}{\partial z}\right)_0} \end{cases} \tag{2.19}$$

the solution of equation (2.17) is

$$(\mathrm{tg}\,\theta)_0 = \frac{1}{(h_1)_0}\left\{ e^{\int_0^y g dy}\left[\int_0^y e^{-\int_0^y g dy} f(y) dy + \frac{1}{(h_1 \mathrm{tg}\,\theta)_{0i}}\right]\right\}^{-1} \tag{2.20}$$

where $(h_1 \mathrm{tg}\,\theta)_0$ represents the initial value of $(h_1 \mathrm{tg}\,\theta)_0$ when y=0. Because equation (2.9) is used, equation (2.20) indicates that $(\mathrm{tg}\,\theta)_0$ has a non-zero solution when equation (2.9) is satisfied. This means that the flow surface is lifted off the surface of the object.

2. Recirculation Conditions

In order to express the second characteristic of the separation flow shown in Figure 1, we investigated the flow behavior near the separation line. Its streamline equations are

$$\begin{cases} \dfrac{1}{h_1}\dfrac{\partial z}{\partial x}=\dfrac{w}{u} \\ \dfrac{h_2}{h_1}\dfrac{\partial y}{\partial x}=\dfrac{v}{u} \end{cases} \tag{2.21}$$

The first equation represents the flow characteristics in a cross-section perpendicular to the separation line. The second formula represents the sectional flow behavior parallel to the xoy plane. When $z \to 0$, it is the wall limiting streamline.

Let us substitute equation (2.10) into the first formula of equation (2.21). After neglecting higher order terms, we get

$$\frac{\partial z}{\partial x}=\frac{(h_1)_0\left(\dfrac{\partial^2 w}{\partial z^2}\right)_0 \cdot z}{\left(\dfrac{\partial^2 u}{\partial z^2}\right)_0 z+2\left(\dfrac{\partial^2 u}{\partial x \partial z}\right)_0 x} \tag{2.22}$$

Based on the theory of singular point for regular differential equations, when

/6

$$q=2(h_1)_0\left(\frac{\partial^2 w}{\partial z^2}\right)_0\left(\frac{\partial^2 u}{\partial x \partial z}\right)_0<0$$

the point o is a saddle point in a cross-section perpendicular to the separation line. When q>0, the point o is a nodal or focal singular point. Furthermore, due to the fact that the flow is away from the surface of the object separation, i.e., w>0, it is easy to find out from the third formula of equation (2.10) that $(\partial^2 w/\partial z^2)_0>0$. Hence, when q>0, $(\partial^2 u/\partial x \partial z)_0>0$. Thus,

$$R=-\left[\left(h_1\frac{\partial^2 w}{\partial z^2}\right)_0+2\left(\frac{\partial^2 u}{\partial x \partial z}\right)_0\right]<0$$

The node or focus o is unstable, which is obviously not the case shown in Figure 1. Therefore, the point o can only be a saddle point. Thus,

$$\left(\frac{\partial^2 w}{\partial z^2}\right)_0\left(\frac{\partial^2 u}{\partial x \partial z}\right)_0<0 \tag{2.23}$$

Because $(\partial^2 w/\partial z^2)_0>0$, therefore,

$$\left(\frac{\partial^2 u}{\partial x \partial z}\right)_0<0 \tag{2.24}$$

This is the criterion for the fluid coming from both sides of the separation flow surface to move outward with the separation flow. We call it the recirculation conditions.

3. Condition for Flow Separation

Based on the above discussion, the condition for determining flow separation on the separation line is

$$\begin{cases} \left(\frac{\partial u}{\partial z}\right)_s = 0 \\ \left(\frac{\partial^2 u}{\partial x \partial z}\right)_s <0 \end{cases} \tag{2.25}$$

Similarly, the condition for attachment of a separation flow in the attachment line is

$$\begin{cases} \left(\frac{\partial u}{\partial z}\right)_a = 0 \\ \left(\frac{\partial^2 u}{\partial x \partial z}\right)_a >0 \end{cases} \tag{2.26}$$

III. Flow Behavior Near Separation Line and Attachment Line

Now let us study the third formula in equation (2.21). When $z \to 0$, it gives the flow behavior. Based on the separation and attachment criteria given above, we have the following conclusions:

1. If $(\partial v/\partial z)_w \neq 0$, on the separation line, the separation line is a wall limiting streamline.

In reality, let us assume that the wall limiting streamline at a point o on the separation line is $x=x(y)$. In the following, we will find various derivatives of $x(y)$ with respect to y at point o. Based on the definition of the wall limiting streamline, the first order derivative is

$$\frac{h_1}{h_2}\frac{dx}{dy}=\frac{\partial u/\partial z}{\partial v/\partial z} \tag{3.1}$$

This equation is used to find its directional derivative along /7
the limiting streamline:

$$\begin{aligned}&\frac{h_1}{h_2}\frac{d^2x}{dy^2}+\left[\frac{\partial}{\partial y}\left(\frac{h_1}{h_2}\right)+\frac{\partial}{\partial x}\left(\frac{h_1}{h_2}\right)\frac{dx}{dy}\right]\frac{dx}{dy}\\&=\left(\frac{\partial^2 u}{\partial y\partial z}+\frac{\partial^2 u}{\partial z\partial x}\frac{dx}{dy}\right)\left(\frac{\partial v}{\partial z}\right)^{-1}-\left(\frac{\partial u}{\partial z}\right)\left(\frac{\partial^2 v}{\partial y\partial z}+\frac{\partial^2 v}{\partial x\partial z}\frac{dx}{dy}\right)\left(\frac{\partial v}{\partial z}\right)^{-2}\end{aligned} \tag{3.2}$$

Based on equation (2.9), on the separation line, $\partial u/\partial z=0$. Hence, $\partial^2 u/\partial y\partial z=0$, $\partial x/\partial y=0$. From equation (3.2), we get

$$\frac{d^2x}{\partial y^2}=0 \tag{3.3}$$

Similarly, we can prove that

$$\frac{\partial^n x}{\partial y^n}=0 \tag{3.4}$$

Here, n=2,3,4... which indicates that all derivatives of the limiting streamline x=x(y) are zero at point o. Therefore, this limiting streamline is the y axis; i.e., the separation line is a limiting streamline.

It is also possible to prove that this conclusion is correct from another angle. In reality, we can perform Taylor series expansion of ∂u/∂z and ∂v/∂z at point o:

$$\begin{cases} \dfrac{\partial u}{\partial z} = \left(\dfrac{\partial^2 u}{\partial x \partial z}\right)_o x + \cdots \\ \dfrac{\partial v}{\partial z} = \left(\dfrac{\partial v}{\partial z}\right)_o + \left(\dfrac{\partial^2 v}{\partial x \partial z}\right)_o x + \left(\dfrac{\partial^2 v}{\partial y \partial z}\right)_o y + \cdots \end{cases} \tag{3.5}$$

After substituting it into equation (3.1) and neglecting higher order small terms, we get:

$$\frac{dx}{\partial y} = Ax \tag{3.6}$$

where

$$A = \left(\frac{h_2}{h_1}\right)_o \left(\frac{\partial^2 u / \partial x \partial z}{\partial v / \partial z}\right)_o \tag{3.7}$$

Integrating equation (3.6) we get

$$x = \pm c e^{Ay} \tag{3.8}$$

Here, c is a constant of integration. It is possible to see that if the integration curve is required to pass through the point o (x=y=0), c=0. This means that the limiting streamline passing through o is x=0. Therefore, the separation line is a limiting streamline.

2. If ∂v/∂z=0, then the limiting streamlines in the neighborhood of the separation line converge toward the

separation line. Moreover, the separation line is the asymptotic line.

In reality, based on Conclusion 1, equation (3.8) is valid. As shown in Figure 2, let the x coordinate for the point A be ε. Then the limiting streamline passing through A is $x=\varepsilon e^{Ay}$. Near the surface of the object, $v>0$. Thus, the flow is in the same direction as the positive y axis direction. Because $v=0$ on the surface of the object, $\partial v/\partial z>0$. For the separation line, however, $\partial^2 u/\partial x\partial z<0$. Based on equation (3.7) we know that $A<0$. This indicates that the distance between the limiting streamline and the separation line decreases with increasing y. Moreover, when $y\to\infty$, $x\to 0$. This means that the limiting streamline is converging towards the positive y direction. If $v<0$, then the /8 flow direction agrees with the negative y direction. In this case, $\partial v/\partial z<0$ on the surface of the object. Therefore, for the separation line, the distance between the limiting streamline and the separation line decreases with decreasing y when $A>0$. In addition, when $y\to -\infty$, $x\to 0$. The limiting streamline converges in the negative y direction. The study shows that in all cases the separation line is the converging line of the neighboring limiting streamline.

3. If $\partial v/\partial z\neq 0$, in the neighborhood of the attachment line, the wall limiting streamline diverges using the attachment line as the asymptotic line (see Figure 3).

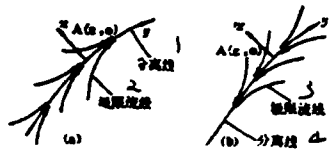

Figure 2. Behavior of Limiting Streamline Near Separation Line

1. separation line
2. limiting streamline
3. limiting streamline
4. separation line

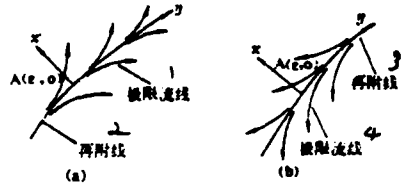

Figure 3. Behavior of Limiting Streamline Near Attachment Line

1. limiting streamline
2. attachment line
3. attachment line
4. limiting streamline

As shown in Figure 3, the equation for the limiting streamline passing through A is $x=\varepsilon e^{Ay}$. If $v>0$, then $\partial v/\partial z>0$. In the event of attachment, $\partial^2 u/\partial x\partial z>0$. Therefore, when $A>0$, the distance between the limiting streamline to the separation line increases with increasing y. When $y\to-\infty$, $x\to 0$. The limiting streamline diverges along the positive y axis. If $v<0$, then $\partial v/\partial z<0$ and $A<0$. When $y\to\infty$, $x\to 0$. The distance between the limiting streamline and the separation line increases as y decreases. This means that the limiting streamline diverges along the negative y axis. In summary, regardless of the situation, the limiting streamline near the attachment line diverges outward using the attachment line as the asymptotic line.

4. For a real flow satisfying the Newtonian friction law, the separation criterion is:

$$(\tau_{zx})_0=0, \quad \left(\frac{\partial\tau_{zx}}{\partial x}\right)_0<0 \tag{3.9}$$

The attachment criterion is:

$$(\tau_{zx})_0=0, \quad \left(\frac{\partial\tau_{zx}}{\partial x}\right)_0>0 \tag{3.10}$$

Furthermore, conclusions 1, 2 and 3 are also applicable to the friction line.

This is due to the fact that based on Newtonian law that on the surface of the object

$$\tau_{zx}=\mu\frac{\partial u}{\partial z}, \quad \tau_{zy}=\mu\frac{\partial v}{\partial z}$$

The friction line is the limiting streamline.

IV. Beginning and Development of the Separation Line

In general, the most upstream position of the separation line is the beginning of the separation line. Without losing generality, through a proper choice of the coordinate, there are two situations concerning the beginning of the separation line. One is a normal point where both friction components are non-zero. The other is a singular point where both friction components are simultaneously zero. Based on the theory that a unique solution to a first order normal differential equation always exists, the separation line starting from a normal point is the segment of the limiting streamline which passes through the starting point. The condition represented by equation (2.25) is met on it. Furthermore, $(\partial^2 u/\partial x \partial z)_w < 0$ distinguishes this segment from other neighboring limiting streamlines. This is the open type of separation[3] described by Wang Guozhang (see Figure 4a). The behavior of the separation line beginning from a singular point will be analyzed together with other singular points on the separation line.

/9

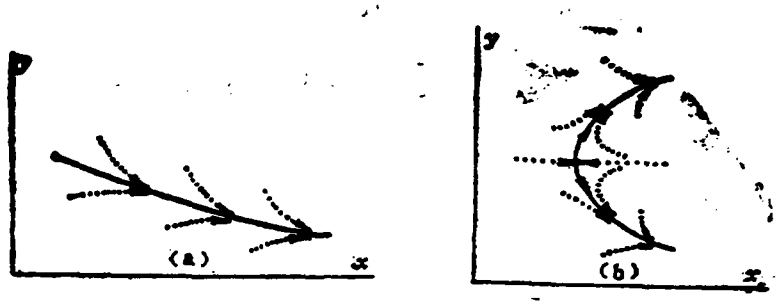

Figure 4. Behavior of Beginning of Separation Lines

An orthogonal coordinate x, y is chosen on the surface of the object. (Here, the y-axis needs not to be the separation line.) The equation of the limiting streamline can be written as:

$$\frac{dy}{dx}=\frac{h_1\frac{\partial v}{\partial z}}{h_2\frac{\partial u}{\partial z}} \tag{4.1}$$

Assume that s is a singular point on the separation line,

$$\left(\frac{\partial u}{\partial z}\right)_s=\left(\frac{\partial v}{\partial z}\right)_s=0$$

Let

$$\begin{cases} q_s=\left[\frac{\partial}{\partial y}\left(h_1\frac{\partial v}{\partial z}\right)\cdot\frac{\partial}{\partial x}\left(h_2\frac{\partial u}{\partial z}\right)-\frac{\partial}{\partial x}\left(h_1\frac{\partial v}{\partial z}\right)\cdot\frac{\partial}{\partial y}\left(h_2\frac{\partial u}{\partial z}\right)\right]_s \\ R_s=-\left[\frac{\partial}{\partial x}\left(h_1\frac{\partial u}{\partial z}\right)+\frac{\partial}{\partial y}\left(h_1\frac{\partial v}{\partial z}\right)\right]_s \end{cases} \tag{4.2}$$

Based on the theory of singularity in differential equations, when $q_s < 0$, it is a smaller point. When $q_s > 0$, the singular point is a node or a focus. Furthermore, when $R_s > 0$, it is stable and the limiting streamline points toward the singular point. When $R_s < 0$, it is unstable and the limiting streamline runs away from the singular point. Based on these results, the following conclusions can be obtained:

1. If the start of the separation line is a singular point, it must be a saddle point.

As a matter of fact, based on the second formula of equation (4.2) and the continuity equation we get

$$R_s = (h_1 h_2)_s \left(\frac{\partial^2 w}{\partial z^2}\right)_s \tag{4.3}$$

Because $\partial^2 w/\partial z^2 > 0$ during separation, therefore, $R_s > 0$. This indicates that if the singularity is a mode or focus, it will be stable. This is obviously not the beginning of the separation line because the direction of the limiting streamline at the beginning of separation is outward. In order to prove that the singularity is indeed a saddle point, let us choose the y-axis as the separation line. Because $\partial u/\partial z = 0$ along the y-axis, therefore /10

$$\frac{\partial}{\partial y}\left(h_1 \frac{\partial u}{\partial z}\right) = 0$$

Based on equation (4.2) we have

$$\begin{cases} q_s = \left[-\dfrac{\partial}{\partial y}\left(h_1 \dfrac{\partial v}{\partial z}\right) \cdot \dfrac{\partial}{\partial x}\left(h_1 \dfrac{\partial u}{\partial z}\right)\right]_s \\ R_s = -\left[\dfrac{\partial}{\partial x}\left(h_1 \dfrac{\partial u}{\partial z}\right) + \dfrac{\partial}{\partial y}\left(h_1 \dfrac{\partial v}{\partial z}\right)\right]_s \end{cases} \tag{4.4}$$

In addition, because it is located on the separation line, we have

$$\frac{\partial}{\partial x}\left(h_1 \frac{\partial u}{\partial z}\right)=h_1 \frac{\partial^2 u}{\partial x \partial z}<0$$

Furthermore, it is at the start of the separation line

$$\frac{\partial}{\partial y}\left(h_1 \frac{\partial v}{\partial z}\right)>0$$

Thus, $q_s < 0$ which corresponds to a saddle point. In this case, the separation line starts from the saddle point and propagates in both directions. Moreover, the two branches intersect tangentially at the starting point, forming a smooth curve extending on both sides and separating the incoming flow from the separation region (see Figure 4b). This is the so-called closed type of initial separation described by Wang Guozhang[3].

2. If in the developing process the separation line encounters singular points, they can only be nodal or focal points.

As a matter of fact, as the separation line enters a singular point, we have

$$\frac{\partial}{\partial y}\left(h_1 \frac{\partial v}{\partial z}\right)<0$$

However, based on equation (2.25)

$$\frac{\partial}{\partial x}\left(h_1 \frac{\partial u}{\partial z}\right)<0$$

Hence, based on the first formula in equation (4.4), $q_s > 0$. Thus, it is not possible to be a saddle point.

Furthermore, equation (4.2) can be used to analyze that the

singular point may be a nodal or focal point.

Similarly, the attachment line can be studied. It was found that it also might have two patterns. One starts from a normal point. The other begins from a node or a focus. It is not possible to start from a saddle point. The end is a singular point which must be a saddle point.

Finally, it should be pointed out that when $z \to 0$, at the singular point s(x=y=0), the second formula in equation (2.21) can be expressed as the following by using NS equations:

$$\cdot\left(\frac{h_2\,dy}{h_1\,dx}\right)_s = \frac{\frac{1}{2}\left(\frac{\partial^2 v}{\partial z^2}\right)_s z^2 + \cdots}{\frac{1}{2}\left(\frac{\partial^2 u}{\partial z^2}\right)_s z^2 + \cdots} = \frac{\left(\frac{\partial^2 v}{\partial z^2}\right)_s}{\left(\frac{\partial^2 u}{\partial z^2}\right)_s} = \left(\frac{h_1}{h_2}\right)_s \left(\frac{\partial p/\partial y}{\partial p/\partial x}\right)_s \qquad (4.5)$$

It is possible to see that the pressure p at point s is not an extremum; i.e., $(\partial p/\partial x)$ and $(\partial p/\partial y)$ are not simultaneously zero. Equation (4.5) gives a specific direction for the curve. Obviously, it is not the spiral singularity observed experimentally. Therefore, the necessary condition for the spiral singularity is that pressure is at its extreme at s.

V. Determination of Separation Line Position /11

In the literature, the position of the separation line is often determined by the two following methods. One is to find the converging asymptotic line or envelope of the wall limiting streamline[3,13]. Based on the above analysis, only the former has some basis for flows described by NS equations*. The other

is based on the minimum surface friction line and assumes that the separation line is the converging asymptotic line of the limiting streamline which is parallel to the minimum friction line. Then, through series expansion of the friction force equation, the position of the separation line is determined by taking the lower order terms[14]. Based on the separation criteria described in this paper, the assumption in this method can be dropped. Thus, the discussion in this paper provided a theoretical basis for this method. Furthermore, this method is also expanded.

This method, in principle, is applicable to the determination of the position of the attachment line.

VI. Simple Conclusions

In a real three-dimensional viscous flow described by NS equations, the Goldstein singularity no longer exists in the neighborhood of separation and attachment lines. Based on this characteristic, through the analysis above, we arrived at the following conclusions:

1. The criterion for flow separation is: on the separation line

$$\left(\frac{\partial u}{\partial z}\right)_0 = 0, \quad \left(\frac{\partial^2 u}{\partial x \partial z}\right)_0 < 0$$

The criterion for the attachment of a separated flow is: on the attachment line

$$\left(\frac{\partial u}{\partial z}\right)_0 = 0, \quad \left(\frac{\partial^2 u}{\partial x \partial z}\right) > 0$$

This is an extension of the two-dimensional Prandtl criterion.

2. The separation line is a limiting streamline. It is the converging asymptotic line for neighboring limiting streamlines. It is not the envelop of limiting streamlines.

3. The attachment line is a limiting streamline. It is a diverging asymptotic line for its neighboring limiting streamlines. The attachment line is not the envelope of limiting streamlines.

4. A separation line may have two starting modes. One begins with a normal point. In this case, the separation line is the segment of limiting streamline beyond the starting point. This is equivalent to the open separation described by Wang Guozhang[3]. The other type starts from a saddle point. The separation line is the boundary between the incoming flow region and the separation region. This is equivalent to the closed separation mentioned by Wang Guozhang. In addition to extending to infinity, a separation line may end at a node or a focus. If the beginning of a separation line is a singular point, it must be a saddle point.

5. An attachment line may also have two modes - normal point and singular point. However, it may only begin as a focus or a node. In adding to extending to infinity, it can only terminate at a saddle point.

6. It is possible to find the converging wall limiting streamline in order to determine the position of the separation line. It is also possible to start from the minimum friction line. The distance between the separation line and the friction

line can be found based on the separation criteria to determine the position of the separation line. Similar methods can be used to determine the position of the attachment line.

---

*In another paper[12] we already proved the envelope criterion is correct for a flow described by boundary layer equations.

Professor Liu Moji of Beijing Institute of Aeronautics and /12
Astronautics is acknowledged for his assistance.

References

[1] Maskell, E.C., RAE Rept. Aero. 2565, Nov. (1955).

[2] Lighthill, M.J., In Laminar Boundary Layers, ed. L. Rosenbead, pp. 1-113, London Oxford (1963).

[3] Wang, K.C., AIAA J. 10, pp. 1044-1050 (1972).

[4] Brown, S.N. and Stewartson, K., Ann. Rev. Fluid Mech. 1, pp. 45-72 (1969).

[5] Williams, J.C., III. Ann. Revg. Fluid Mech. 9, pp. 113-144, (1977).

[6] Eichelbrenner, E.A. and Oudart, A., ONERA Publ. 76, Chatillon, France (1955).

[7] Legendre, R., La Recherche Aeronautique, No. 54, 3-8 (1956).

[8] Hunt, J. C.R., Abell, C.J., Peterka, J.A., and Woo, H., JFM 86, Part 1, pp. 179-200 (1978).

[9] Tobak, M. and Peake, D.J., AIAA Paper 79-1480 (1979).

[10] Tobak, M. and Peake, D.J., AIAA Paper 81-1260 (1981).

[11] Tobak, M. and Peake, D.J., Ann. Rev. Fluid Mech. Vol. 14, pp. 61-85 (1982).

[12] Zhang Hanxin, Behavior of the Separation Line in Three-dimensional Steady Viscous Flow - An Analysis Based on Boundary Layer Equations. China Aerodynamic Research and Development Center Report, 1983.

[13] Tai, T.C., AIAA J. 19, 10 (1981).

[14] Hirschel, E.H. and Kordulla, W., Flugwiss, Z., Weltraumforsch 4, Heft 5 (1980).

Aerodynamic Calculation of Airfoil with Separation /13

Zhu Ziqiang, Chen Bingyong and Zhang Bingxuan
(Beijing Institute of Aeronautics and Astronautics)

Abstract

An aerodynamic computation for wing section with separation is presented in this paper. A vortex is used to simulate the separation wake boundary. The strength of this vortex sheet is rationally chosen. An "equivalent body" is formed by this separated wake vortex sheet and the attached flow region of the wing section. The iterative potential flow solution, which includes boundary layer effect, is used to solve this equivalent body. The shape of the separation wake boundary and the position of the separation point are determined in the iteration process. Two classical wings were calculated. The computational results are in good agreement with experimental data.

I. Introduction

In most aeronautical problems involving high Reynolds numbers, when the angle of attack is not too large and flow separation does not occur, the aerodynamic characteristics of a viscous flow around an object (such as a wing) can be calculated with sufficient accuracy through a potential flow calculation with boundary layer effect. Reference [1] presented the problem of calculating the mutual interaction between the potential flow

and the boundary layer. The computational results obtained in that paper were found to be in good agreement with the experimental data at small attack angles. With increasing attack angles, the difference gradually increases. This is due to local separation on the wing. As the attack angle gets larger, this separation expands from the rear towards the front. Hence, in order to rationally estimate the aerodynamic characteristics at large attack angles, it is necessary to take the effect of separation on the wing into consideration.

As the range of an attack angle used in aerospace expands, also in response to the need in designing high lift equipment, it is desirable to have a practical engineering calculation method which can account for the effect of separation. It should be capable of calculating the aerodynamic characteristics within the attack angle range up to near the maximum lift coefficient Cl_{max}, including the capability to provide a relatively accurate pressure distribution.

Jacob[2] first addressed this problem by empirically placing rational source and sink distributions in the trailing edge of the wing to simulate wake separation. Then, he employed the potential flow theory to solve the flow of this "equivalent body" with distributed sources. Results indicate that it is feasible to calculate the effect of separation wake by extending the streamline in the rear of the wing using source and sink. Masanori, Hayashi and Eiichi Endo[3] also used a similar method to calculate the Cl_{max} characteristics.

It is also possible to use a vortex sheet extending from the

wing as the separation wake boundary, instead of using a source and sink distribution. An "equivalent body" is formed by adding such a vortex sheet in front of the attachment flow region of the wing. The boundary of the separation wake and the position of the separation point are determined in the iterative process in finding the complete solution[4-7]. In addition, other authors took a step further to consider the flow in the separation wake. An extended jet mixing model was used as the solution of the flow inside the wake. Then, it is used simultaneously with the external equivalent potential flow solution to determine the boundary of the separation wake. In this case, iterations are still required. Consequently, another iterative step is added to complicate the entire process. The work load is significantly increased[6-7].

In this paper is an iterative method for calculating the aerodynamic force by using a vortex sheet to simulate the separated wake boundary. It is capable of taking the effect of separation and the wall boundary effect at the front of the wing into account. The intensity of the separation vortex sheet, to some extent, can be rationally selected based

Manuscript received on June 5, 1984, revision received on July 28.

on the pressure distribution in the separation wake area obtained /14
experimentally. Thus, the computational results would be in better agreement with the reality.

The author wishes to express his gratitude to Professor Lu Shijia for his concern and support.

II. Aerodynamic Simulation of Flow Around Wing with Separation Wake

Based on a great deal of experimental work on different wings at various attack angles, in the separation wake region, the pressure distribution in front of the trailing edge of the wing (such as in area A in Figure 1) is essentially constant. It is equal to the pressure at the separation point. Afterward, during the merge of the two flows, pressure will gradually increase to C_{pR} at the merging point R. C_{pR} is slightly less than the pressure at the stationary point. We choose the vortex sheet as the boundary of the separation wake region. In addition, based on the fact that this vortex sheet is a streamline, this streamline, together with the wing surface in front of the separation point where the flow is attached, is considered as an equivalent body. From the potential flow solution of the equivalent body which includes boundary layer effect, it is possible to obtain the pressure distribution on the wing. Due to the fact that the separation vortex sheet on the upper wing surface begins at the separation point of the boundary layer, the profile of the enclosed wake boundary and the position of the separation point must be solved by iterations as a part of the whole solution.

When there is a potential flow around the equivalent object, there should be two stationary points. We choose the merge point as the rear stationary point. This is equivalent to the situation that two vortex streamlines from the upper wing surface

and the trailing edge meet at the merge point; where the velocity should be zero and the corresponding vortex strength should be zero. Of course, the pressure is the stationary point pressure. Compared to the pressure at the point in a real flow, there is some difference, yet the difference is very small. The difference will not significantly affect the pressure distribution on the wing. In region A of the separation wake, we choose the pressure at the upper wing separation point and that at the lower wing trailing edge to be equal to the pressure. When solving the potential flow, we distribute vortices on the attachment flow wing surface and the separation boundary. Because under the condition that the object surface cannot be penetrated, the vortex intensity distribution γ on an enclosed vortex sheet without any singular points is equal to the velocity outside the surface. The condition that the pressure at the separation point on the upper surface is equal to that at the trailing edge of the lower surface is equivalent to the fact that the vortex intensities at these two places are equal. Furthermore, by referring to the direction of flow, it is possible to see that the vortex strengths are equal and the directions are opposite at these two places; i.e., $\gamma_{up, separation}=-\gamma_{low, trailing edge}$. This may also be called the extended Kuttar condition with separation.

Thus, the strength of the separation vortex sheet can be chosen as follows. In region A, the vortex sheet strength is equal to that at the separation point. In region B, it is decreasing with the square of distance downstream until $\gamma=0$ at

the point of merge (See Figure 1). At the upper boundary, $\gamma=-\gamma_1[1-(x_i/x_w)^2]$. Here, γ_1 is the vortex strength at the lower trailing edge. The shape of the separation vortex sheet, however, should be determined based on its streamline condition in iterations.

As for the calculation of the boundary layer displacement thickness effect of the attachment flow, similar to what was done in reference [1], the equivalent normal penetration velocity can be determined based on the boundary layer displacement thickness derived from the potential flow. It is only necessary to deploy a corresponding source distribution with strength $m=(d/dx)(u_e\delta^*)$ to simulate the boundary layer effect.

III. Calculation of Potential Flow

In order to facilitate the calculation, the upper and lower wing surfaces are divided into many equal and unequal elements. The polygon formed by these surface elements is used to approximate the profile of the original object. Considering that the aerodynamic characteristics near the trailing edge vary more rapidly at low flow velocities, the following unequal method is used to divide the surface elements:

$$x_i/c=\frac{1}{2}[1+\cos\theta_i] \qquad (1) \qquad /15$$

$$\theta_i=i\pi/n;\ i=0,1,2,\cdots\cdots,n$$

where the origin is located at the leading edge, x-axis is along the chord direction, z-axis is positive upward, and c is the chord length.

On small surface elements, linear strength vortex distribution is arranged. Its strength is determined by the boundary condition that no penetration is allowed at the control point of each element.

The induced velocity produced by any vortex segment B at any point in space can be calculated based on Biot-Savart equation:

$$\vec{V} = \frac{1}{2\pi} \oint_c \frac{\gamma(s)\,\vec{r}'}{r^2} ds \tag{2}$$

The normal induced velocity at point i due to the vortex distribution of the entire wing is:

$$V_{n_i} = \frac{1}{2\pi} \sum_{j=1}^{2n+1} A_{n_{i,j}} \gamma_j \tag{3}$$

where $An_{i,j}$ is the aerodynamic force effect coefficient.

If we choose a typical surface element j and control point i (such as shown in Figure 2), the vortex strength on the element is a linear function, i.e.,

$$\gamma(s) = \gamma_j + \frac{(\gamma_{j+1} - \gamma_j)}{l_j} s \tag{4}$$

Figure 1

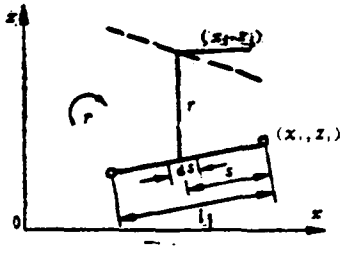

Figure 2

After substituting it into the Biot-Savart equation, we get

$$\vec{V}_{i,j}=\frac{1}{2\pi l_j}[\gamma_j(H_{1_{i,j}}\vec{i}-H_{3_{i,j}}\vec{j})+\gamma_{j+1}(H_{4_{i,j}}\vec{i}-H_{4_{i,j}}\vec{j})] \tag{5}$$

where $H_{1_{i,j}}$, $H_{2_{i,j}}$, $H_{3_{i,j}}$ and $H_{4_{i,j}}$, were defined in reference [1].

Comparing equation (5) to equation (3), we can write

$$\vec{A}_{i,j}=H_{3_{i,j-1}}\vec{i}-H_{4_{i,j-1}}\vec{j}+H_{3_{i,j}}\vec{i}-H_{3_{i,j}}\vec{j} \tag{6}$$

In addition, the normal velocity component of the incoming flow at point i is:

$$V_{\infty,i}=V_\infty[\cos\alpha\,\vec{i}+\sin\alpha\,\vec{j}]\cdot\vec{n}_i \tag{7}$$

In order to satisfy the boundary condition, we get the following matrix equation:

$$\frac{1}{2\pi}[A_n]\{\gamma\} = -\{V_{n\infty}\} \tag{8}$$

Based on this, it is possible to obtain the unknown vortex strength distribution: /16

$$\{\gamma\} = -2\pi[A_n]^{-1}\{V_{n\infty}\} \tag{9}$$

From equation (8) we know that the number of control points is one less than that of the unknown γ. In order to close the equations, the Kuttar condition can be used as a supplemental equation. In reference [1], several commonly used Kuttar conditions were compared. In this paper, because the effect of separation wake is considered, we adopt the following:

$$\gamma_{\text{up, separation}} = -\gamma_{\text{low, trailing edge}} \tag{10}$$

IV. Iterative Calculation to Consider Separation Wake Effect

Based on the aerodynamic model of separation wake discussed above, the specific steps for computation are:

(1) Make potential flow calculation for the wing first to obtain the potential flow pressure distribution.

(2) Calculate the boundary layer based on the pressure distribution obtained. In addition, the displacement thickness distribution and the separation point position on the wing are

also obtained.

(3) Assume an initial profile for the wake boundary.

(4) Adjust the wake boundary leaving the separation point unchanged. Based on the requirements that the wake boundary is a streamline and the solid wall attachment flow area is not penetrable (including the displacement thickness effect of the boundary layer), iterations are performed until the wake boundary variation becomes very small after two iterations. We call it internal iteration.

(5) The new pressure distribution thus obtained is different from the originally calculated pressure distribution in the boundary layer. It is necessary to re-calculate the boundary layer based on the new pressure distribution in order to obtain the new boundary layer displacement thickness distribution and the separation point position.

(6) Repeat steps (3)-(5) as the iterative calculation. We call this external iteration. It is carried out until the change of C_1 in two consecutive iterations is less than a specified number. The convergent solution at this attack angle is thus obtained.

In the calculation, because the separation point position varies, it is necessary to make geometric modification for each new separation point position in order to make the separation point locate at a corner of the surface element. Hence, we must

also modify a portion of the aerodynamic effect index matrix. In addition, the changing vortex sheet also requires the modification of the aerodynamic index matrix accordingly. However, only individual rows or columns are required to be modified. It is not necessary to repeat the calculation of the entire aerodynamic index matrix in order to save computing time. Thus, in every step of the iterative process, after modifying the aerodynamic effect index matrix, new vortex strength distribution and pressure distribution that satisfy the boundary condition of the wing surface can be obtained.

In the iteration, the third step is to provide an initial profile for the wake boundary. In this calculation, it is given according to the following. The wake boundary of the upper wing surface begins from the separation point. Furthermore, an initial direction is given (such as the median value between the incoming flow direction and the slope of the wing at that point). Similarly, the lower wing surface boundary is assumed to start from the trailing edge. An initial direction is also given. Furthermore, based on the width of separation at the trailing edge (also known as the wake altitude) and the empirical aspect ratio of the wake:

$$WF = \frac{\text{wake length}}{\text{wake altitude}} = \frac{L}{H} \qquad \text{(See Figure 3)}$$

it is possible to determine the initial wake length. Moreover, both upper and lower boundaries are assumed to be quadratic curves. Thus, the initial wake boundary can be determined. The aspect ratio of the wake, WF, is obtained from the empirical curve shown in Figure 4[4].

/17

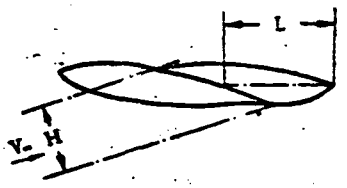

Figure 3

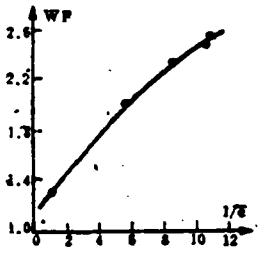

Figure 4

V. Calculation of Boundary Layer

The iteration technique only considers the displacement thickness effect of the boundary layer. It is not required to study the structure inside the boundary layer. Because the integral equation method is relatively simple and consumes much less time, it was chosen to calculate the boundary layer. The calculation of the boundary layer had been comprehensively introduced in reference [1]. The required formula and method were explained in detail. The following is a brief introduction of this method.

(1) Laminar Boundary Layer

Due to the fact that we are considering incompressible flows, the Thwaite method was chosen to calculate the laminar boundary layer on the wing.

(2) Estimation of Turning Point

The Granville method was adopted to determine the position of the turning point. Based on the local profile factor H in laminar boundary layer calculation, we used the criterion curve derived from stability theory to determine whether a point is unstable. If it is already unstable, it is necessary to use the turning criterion curve to determine whether it is a turning point. Otherwise, the calculation continues based on laminar flow condition.

(3) Turbulent Boundary Layer

The Nash method was chosen in this calculation. This is a better integral equation method recommended by the

two-dimensional incompressible turbulent boundary layer meeting held in Stanford in 1968. This method considers the "upstream history effect" of the turbulent boundary layer.

In this calculation, we assumed that separation began from H=1.8.

VI. Results and Discussion

In reference [1], we had already discussed some general problems, such as the effect of surface element division, surface element number and boundary layer calculation, in iterations. In this paper, the simulation of separation wake at large attack angles is discussed. In addition, two classical wings are calculated. The computational results are compared to the experimental data.

(1) There are many criteria capable of determining whether the separation wake boundary adjustment in internal iteration is convergent. In this work, it is determined by the difference of the boundary after two iterations. It was found that the boundary variation becomes very small after two adjustments. The maximum deviation is less than 1% chord length. Furthermore, the maximum is located downstream far away from the wing. Hence, its effect on the wing surface is relatively small. Based on the fact that the computed results of both wings are in good agreement with the experimental data, this type of error is /18 certainly allowable.

(2) The rate of convergence for the external iteration is

also very fast. At large attack angles, if we begin to calculate from the potential flow solution, the convergence requirement can generally be met in 5~6 iterations; i.e., after two consecutive iterations the change in $c_l \leq 1\%$. If we calculate the attack angle continuously, i.e., to use the convergent solution of the preceding attack angle to begin to solve the next one, a convergent solution can usually be obtained in 2~3 iterations.

(3) In air calculation, it was found that the initial direction of the separation wake boundary still has some effect. At small attack angles, it is feasible to assume that it is between the incoming flow direction and the wing slope direction at the point of separation. Nevertheless, with increasing attack angle, it should gradually move to the incoming flow direction to make the computational results close to experimental data.

(4) Figure 5 and Figure 6 show comparisons of experimental data to calculated results of the pressure distribution on the Model GA(W)-1 wing when the attack angles are 16.04° and 18.25°, respectively. The experimental data were obtained in reference [8]. From the figures we can see that they agree very well with the exception of the peak values at the leading edge. The position of separation points are also fairly close. Based on comparisons, the experimental data to calculated results when $\alpha=19.06^\circ$ and 20.05° do not agree as well as at other attack angles. In this case, the attack angle has already approached Cl_{max}. When the angle of attack is greater than 20°, the forward movement of the separation point on the upper wing surface is very large and sudden. Therefore, our simple model cannot reflect such violent changes of the flow pattern.

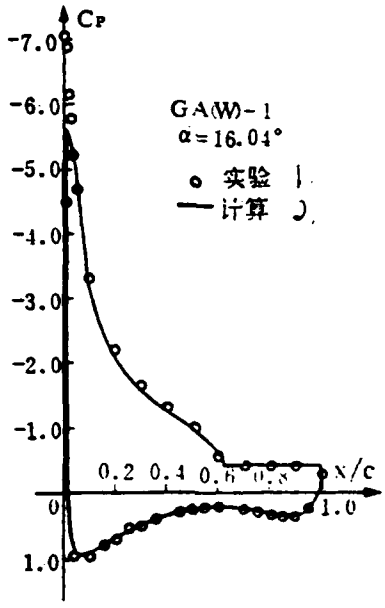

Figure 5

1. experimental
2. calculated

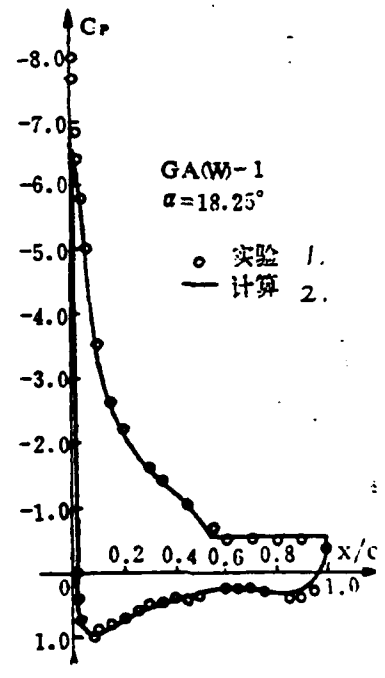

Figure 6

1. experimental
2. calculated

Figures 7 and 8 show comparisons of the calculated and experimental pressure distributions of the NACA 4412 airfoil. The experimental data were obtained from reference [9]. Based on these figures, they agree very well. The experimental data, however, do not show a clear position of the separation point and the separation region. This might be due to measurement errors because based on force measurements separation should exist on the wing.

/19

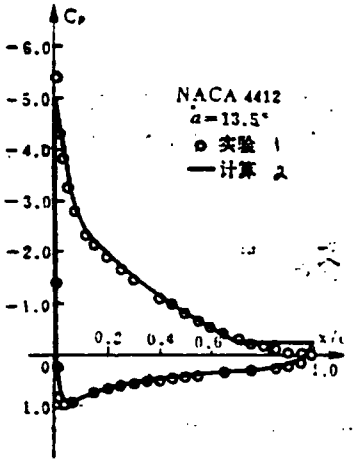

Figure 7

1. experimental
2. calculated

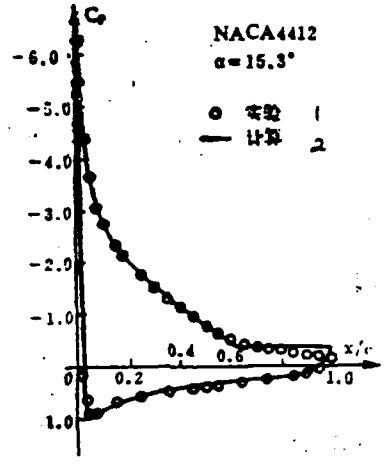

Figure 8

1. experimental
2. calculated

(5) Figures 9 and 10 show the experimental data and calculated results of $c_l \sim \alpha$ and $c_m \sim \alpha$ for two wing models, respectively. We can see that they agree well until Cl_{max}. This indicates that although this modeling which takes separation effect into account is simple and coarse, it is able to reflect the reality. However, the agreement is not as good beyond Cl_{max}, which indicates that this model is limited.

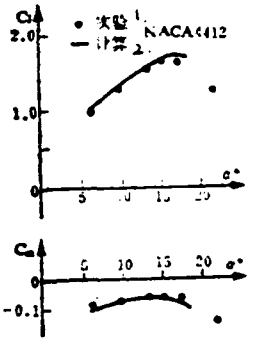

Figure 9

1. experimental
2. calculated

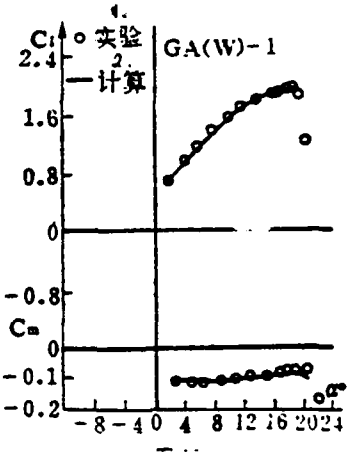

Figure 10

1. experimental
2. calculated

This paper presents an iterative solution for calculating the aerodynamic force on a wing with separation. An "equivalent body" formed by streamline displacement is used to replace the original geometric body. The potential flow theory is used to find solution for this equivalent body. It is capable of obtaining the aerodynamic characteristics of the entire wing until near Cl_{max}. The boundary of the separation wake, the displacement thickness of the boundary layer and the position of the separation point are iterated as a part of the whole solution. Calculations were done with two wing models. The results show that: /20

(1) It is feasible to use this streamline displacement equivalent body concept as an engineering model for separation wake. In the attack angle range up to cl_{max}, calculated results agree well with experimental data.

(2) The rate of convergence of this computation method is very fast, especially when calculating continuous attack angles.

(3) When the attack angle exceeds cl_{max}, this simple model cannot give us good results. It remains to be further improved.

References

[1] Zhu Ziqiang and Chen Yanqing, "Iterative Solution of Incompressible Viscous Flow Around Any Wing", Technical Report No. BH-B 566 of Beijing Institute of Aeronautics and Astronautics, (1980).

[2] Jacob, K., "Advancement of a method for calculating separated flows around airfoils with special consideration of profile drag", ESA TT-373. (1977).

[3] Masanori, Hayashi, Eiichi Endo, "Performance calculation for multi-element airfoil sections with separation", Transactions of the Japan Society for Aeronautics and space Vol. 20, No. 49 (1977).

[4] Rao, B.M., Dvorak, F.A. and Maskaw, B., "An analysis method for multi-component airfoils in separated flows", NASA CR-159300 (1980).

[5] Henderson, M.L., "A Solution to the 2-D separated wake modeling problem and its use to predict Cl_{max} of arbitrary airfoil sections", AIAA Paper 78-156 (1978).

[6] Gross, L.W., "The prediction of two-dimensional airfoil stall progression", AIAA Paper 78-155 (1978).

[7] Zumwolt, G.W., Elamgovan, R., "Computation of low speed flow past multi-element airfoils with large flow separation", ICAS-82-6.2.2.

[8] McGbee, R.J., Beasley, W.D., "Low Speed aerodynamic characteristics of a 17-percent-thick airfoil section designed for general aviation applications", NASA TND-7428 (1973).

[9] Pinkerton, R.M., "The variation with Reynolds number of pressure distribution over an airfoil section", NACA TR 613 (1938).

Numerical Simulation of Vortex Breakdown /22

Shi Xungang

(Beijing University)

Abstract

In this work, the breakdown of an isolated axisymmetric vortex embedded in a uniform flow is examined by numerically integrating the complete Navier-Stokes equations for an unsteady axisymmetric flow. The results show that: when the vortex is small, the vortex is stable. The solution approaches a steady flow. A quasi-cylindrical approximation is a good approximation for this type of flow. When the vortex strength is sufficiently high, the solution is unsteady. A re-circulation zone is formed near the axis. Its shape and internal structure resemble those of the multi-cell breakdown bubbles observed by Faler and Leibovich (1978). With appropriate combinations of flow parameters, the flow appears to be quasi-periodic after some time. Parallel calculations made with the quasi-cylindric approximation show that as far as predicting the breakdown of the vortex is concerned, both methods are in good agreement. They both show that in the relatively low Reynolds number range covered by this work, vortex breakdown is not closely related to Reynolds number. Furthermore, it is independent of the critical classification of the upstream flow.

I. Introduction

Since Peckham and Atkinson (1957) observed the breakdown of leading edge vortex of a sweepback wing at a large attack angle for the first time, various theories have been presented by a number of authors to explain the breakdown of the vortex; such as the critical flow theory by Squire (1960) and Bossel (1967, 1969), the finite transition theory by Benjamin (1962, 1967), the fluid dynamic instability theory by Ludwieg (1962) and the quasi-cylindrical approximation theory by Gartshore (1962, 1963), Hall (1965, 1966, 1967) and Mager (1972). Up until now, however, not a single theory has been widely accepted. There is considerable confusion among various theories as well as in comparison between theoretical and experimental results.

Based either on the critical flow theory or the finite transition theory, the flow upstream of the breakdown must be super critical. Hall (1967, 1972) and Ludwieg (1970) also pointed out that the vortex breakdown process described by quasi-cylindrical approximation is a process approaching the critical state from a super critical state. Thus, it seems to be a relatively popular viewpoint, i.e., vortex breakdown must begin from a super critical upstream flow. Nevertheless, Lavan, Nielsen, and Fejer (1969), Kopecky and Torrance (1973), and Grabowski and Berger (1976) numerically integrated the Navier-Stokes equations for a steady, axisymmetric flow and obtained the re-circulation zone consisting of axisymmetric breakdown bubbles similar to those observed experimentally, regardless of whether the upstream flow is

super critical or subcritical. This contradiction still remains to be classified.

On the other hand, their numerical results failed to show the double-cell structure inside the breakdown bubble as observed by Faler and Leibovich (1978) by laser flowmeter (See Figure 1). Furthermore, when

Manuscript received on June 22, 1984. Revised manuscript received on September 28.

the rotational velocity is sufficiently high, their calculations /23
could not even result in convergent solutions. This might be attributed to the fact that the assumptions they made are too rigorous. Leibovich (1978) believed that numerical results could not describe such double cell structure if the experimentally observed periodicity and asymmetry of the flow inside the breakdown bubbles were not considered.

In this work, their opinions are noted. Through numerical integration of the complete N-S equations for an unsteady axisymmetrical flow, we wish to be able to more closely describe the breakdown of an "axisymmetric" vortex. Based on economic consideration and computer limitation, the axisymmetric assumption is reluctantly kept. In order to facilitate the analysis and comparison, parallel calculations based on quasi-cylindrical approximation are also made. On this basis, the contradiction between theoretical and numerical results mentioned above is discussed.

II. Mathematical Model

In this paper, an isolated axisymmetric vortex embedded in an unbounded uniform flow is studied. Let us choose a cylindrical coordinate. The x-axis coincides with the axis of symmetry. Let us assume that the axial and circumferential velocity distributions on an "inlet cross-section" are given by the two following equations:

$$x=0;\ \begin{cases} u=1+a\,f(r) \\ w=\Gamma_0\,g(r) \end{cases}$$

where the velocity components and coordinates are rendered dimensionless by using the velocity of the uniform flow at infinity u_∞ and vortex core radius R. Figure 2 schematically shows their profiles. The initial axial velocity on the axis, $U_0=1+a$ and the velocity at infinity or the vortex strength Γ_0 are the two flow parameters.

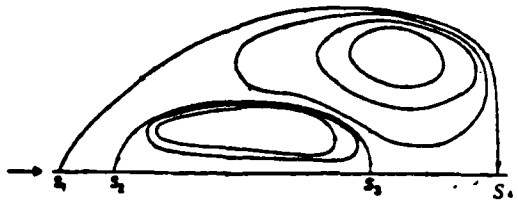

Figure 1. Flow Field Structure Inside an Axisymmetric Breakdown Bubble (Leibovich 1978)

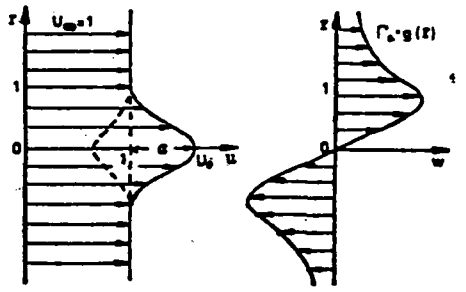

Figure 2. Initial Axial and Circumferential Velocity Distributions

If we introduce a local moment, $\Gamma = rw$

the circumferential vortex component $\Omega = \partial v/\partial x - \partial u/\partial r$

and the flow function Ψ,

then the dimensionless N-S equation for an unsteady, axisymmetric flow of a viscous, incompressible fluid can be re-written as a series of equations of Γ–Ω–Ψ.

/24

$$
\begin{cases}
\dfrac{\partial \Gamma}{\partial t} + u\dfrac{\partial \Gamma}{\partial x} + v\dfrac{\partial \Gamma}{\partial r} = \dfrac{1}{Re}\left[\dfrac{\partial^2 \Gamma}{\partial x^2} + r\dfrac{\partial}{\partial r}\left(\dfrac{1}{r}\dfrac{\partial \Gamma}{\partial r}\right)\right] \\
\dfrac{\partial \Omega}{\partial t} + u\dfrac{\partial \Omega}{\partial x} + v\dfrac{\partial \Omega}{\partial r} - \dfrac{v\Omega}{r} - \dfrac{\partial}{\partial x}\dfrac{\Gamma^2}{r^3} = \dfrac{1}{Re}\left\{\dfrac{\partial^2 \Omega}{\partial x^2} + \dfrac{\partial}{\partial r}\left[\dfrac{1}{r}\dfrac{\partial (r\Omega)}{\partial r}\right]\right\} \\
\dfrac{\partial^2 \Psi}{\partial x^2} + r\dfrac{\partial}{\partial r}\left(\dfrac{1}{r}\dfrac{\partial \Psi}{\partial r}\right) = r\Omega \\
u = 1 - \dfrac{1}{r}\dfrac{\partial \Psi}{\partial r}\ , \qquad v = \dfrac{1}{r}\dfrac{\partial \Psi}{\partial x}
\end{cases}
$$

where $Re=u_\infty R/\nu$. This is a series of parabolic equations. In terms of spatial coordinates alone, it is also elliptical. In order to obtain a unique solution, it is necessary to have the appropriate initial conditions and the boundary conditions along the entire boundary of integration.

The integration region is given as follows:

$$D=\{0\le x\le L,\ 0<r<+\infty\}$$

The outlet end of the boundary is chosen sufficiently for downstream at x=L, where L>>1. For example, we choose L=20

The conditions to have a unique solution are as follows:

Initial condition:

$$t=0;\ \Gamma=\Gamma_\infty rg(r),\quad \Omega=-af'(r),\quad \Psi=-a\int_0^r rf(r)dr \quad \text{在}D\text{中}$$

The boundary conditions in D are:

$$\begin{aligned}
&x=0: && \Gamma=\Gamma_\infty r\,g(r), && \Omega=-a\,f'(r), && \Psi=-a\int_0^r r\,f(r)dr;\\
&x=L: && \frac{\partial\Gamma}{\partial x}=0, && \frac{\partial\Omega}{\partial x}=0, && \frac{\partial^2\Psi}{\partial x^2}=0;\\
&r=0: && \Gamma=0, && \Omega=0, && \Psi=0;\\
&r\to+\infty: && \Gamma\to\Gamma_\infty, && \Omega\to 0, && \frac{\partial\Psi}{\partial r}\to 0.
\end{aligned}$$

The so-called quasi-cylindrical approximation is to assume

$$v\ll u,w \qquad \frac{\partial}{\partial x}\ll\frac{\partial}{\partial r}$$

Furthermore, the flow is steady. In this approximation, the above equations can be simplified as:

$$
\begin{cases}
u\dfrac{\partial \Gamma}{\partial x}+v\dfrac{\partial \Gamma}{\partial r}=\dfrac{r}{Re}\dfrac{\partial}{\partial r}\left(\dfrac{1}{r}\dfrac{\partial \Gamma}{\partial r}\right) \\
u\dfrac{\partial \Omega}{\partial x}+v\dfrac{\partial \Omega}{\partial r}-\dfrac{v\Omega}{r}-\dfrac{\partial}{\partial x}\dfrac{\Gamma^{2}}{r^{3}}=\dfrac{1}{Re}\dfrac{\partial}{\partial r}\left[\dfrac{1}{r}\dfrac{\partial (r\Omega)}{\partial r}\right] \\
u=1+\int_{r}^{\infty}\Omega dr \\
\Psi=\int_{0}^{r}r(1-u)dr \\
v=\dfrac{1}{r}\dfrac{\partial \Psi}{\partial x}
\end{cases}
$$

This is also a series of parabolic equations. After the initial /25
conditions at the initial cross-section x=0 and the boundary conditions at the axis, r=0, and at the outer edge $r\to+\infty$, are given, it is always possible to obtain a numerical solution along the x direction. The initial conditions are:

$$x=0:\quad \Gamma=\Gamma_0 rg(r),\quad \Omega=-af'(r)$$

The boundary conditions are:

$$
\begin{array}{lll}
r=0 & \Gamma=0 & \Omega=0 \\
r\to+\infty & \Gamma\to\Gamma_0 & \Omega\to 0
\end{array}
$$

However, the quasi-cylindrical approximation is no longer valid near the vortex breakdown point. The differential equations also become unsteady. Numerical calculations are no longer convergent from this point onward. Hence, the appearance of large axial gradient and computational divergence can be considered as a sign for vortex breakdown.

In order to make the infinite integration area in the r direction finite, and to ensure that the numerical solution has sufficiently high resolution in areas where the flow varies vigorously, two independent coordinate transformations are introduced for the radial and axial direction, respectively:

$$x = c(e^{b\xi} - 1) \qquad x : (0, L) \to \xi : (0, 1)$$

$$r = \tan\eta \qquad r : (0, +\infty) \to \eta : \left(0, \frac{\pi}{2}\right)$$

In the quasi-cylindrical approximation, only the radial transformation is required. The above differential equations, as well as the initial and boundary conditions, must be transformed correspondingly.

III. Computational Results and Discussion

The average implicit finite difference method developed by Crank-Nicolson was used to solve the simplified equations in quasi-cylindrical approximation. This technique is simple and efficient. The results show that axial velocity varies very slightly along the axis when Γ_0 is very small, e.g., Γ_0=0.63. If we continue to proceed downstream, axial velocity decreases initially and then rises gradually; approaching the incoming flow velocity $U \to 1$. The vortex is stable. As Γ_0 increases, axial velocity decreases more rapidly. When Γ_0 drops below a certain value, axial velocity drops abruptly to a value very close to 0 in front of a specific position. The calculation is no longer convergent afterward. As mentioned above, this position can be considered as the breakdown point. With increasing Γ_0, the breakdown point position continues to move upstream. An increase in U_0, however, will strengthen the stability of the vortex. The sumbols in Figure 3 represent a summary of calculated results obtained using the quasi-cylindrical approximation. Based on the

plot, with the exception of one point U_0=1.4 and Γ_0=0.8944, the conclusions on whether the vortex breaks down or not agree with those obtained by calculation with Re=100 and 200. The dot and line curve in the figure represents the vortex breakdown boundary.

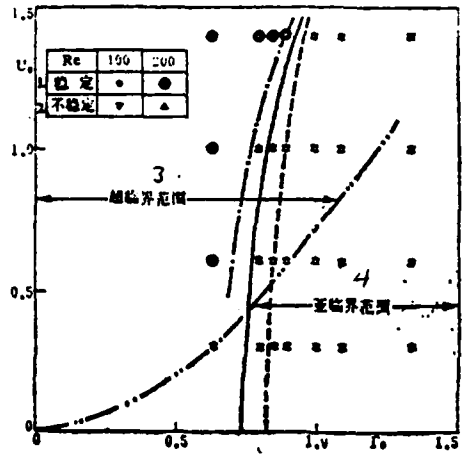

Figure 3. Summary of Calculated Results

1. stable
2. unstable
3. super critical region
4. subcritical region

An alternate direction iteration method was used to solve /26
the complete N-S equations. The results show that a stable flow predicted by the quasi-cylindrical approximation reaches a certain steady state after some time. The flow surface appears to be very smooth. The quasi-cylindrical approximation should obviously be valid in the entire flow field. A comparison of velocity distribution also shows that the flow fields obtained by two different methods are in good agreement. This indicates that the quasi-cylindrical approximation is appropriate for a stable vortex. In addition, the computer program designed for numerically integrating the complete N-S equations also underwent a thorough test.

When predicting vortex breakdown under quasi-cylindrical approximation, except for individual edge cases, the numeric solution of the complete N-S equations shows that the flow is unsteady. Figure 4 is an example. They are a series of cross-sections of an axisymmetric flow surface and a meridian plane. As time goes by, it first begins to bulge near the axis and then develops into an enclosed re-circulation zone. This re-circulation zone continues to grow into a so-called "double-cell" structure (See Figure 4). Its shape and internal structure are very similar to those of the breakdown bubble obtained by Faler and Leibovich (1978) with a laser flowmeter (See Figure 1). Under certain appropriate combinations of flow parameters, the flow exhibits some quasi-periodicity after some time. A new inner cell is continuously formed periodically at the tip of the breakdown bubble. It gradually intensifies and moves backward

with the flow. Then, itself or in combination with the cell formed earlier becomes a large bubble and flows downstream. Or, it could flow away alone. In Figure 4, b-d and e-g are very similar sequentially which can be considered as the periodicity of the solution.

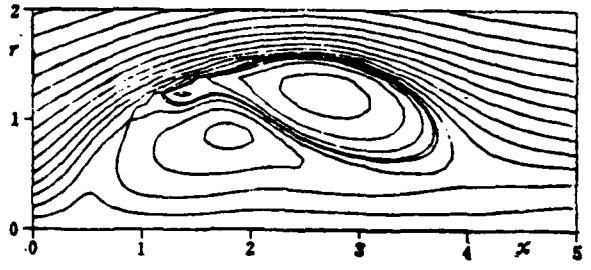

(a) t = 96

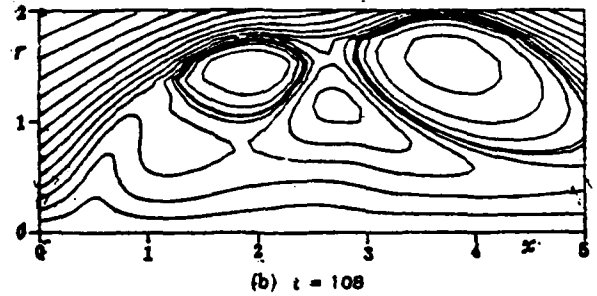

(b) t = 108

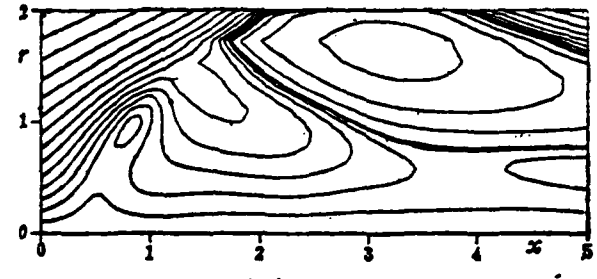

(c) t = 114

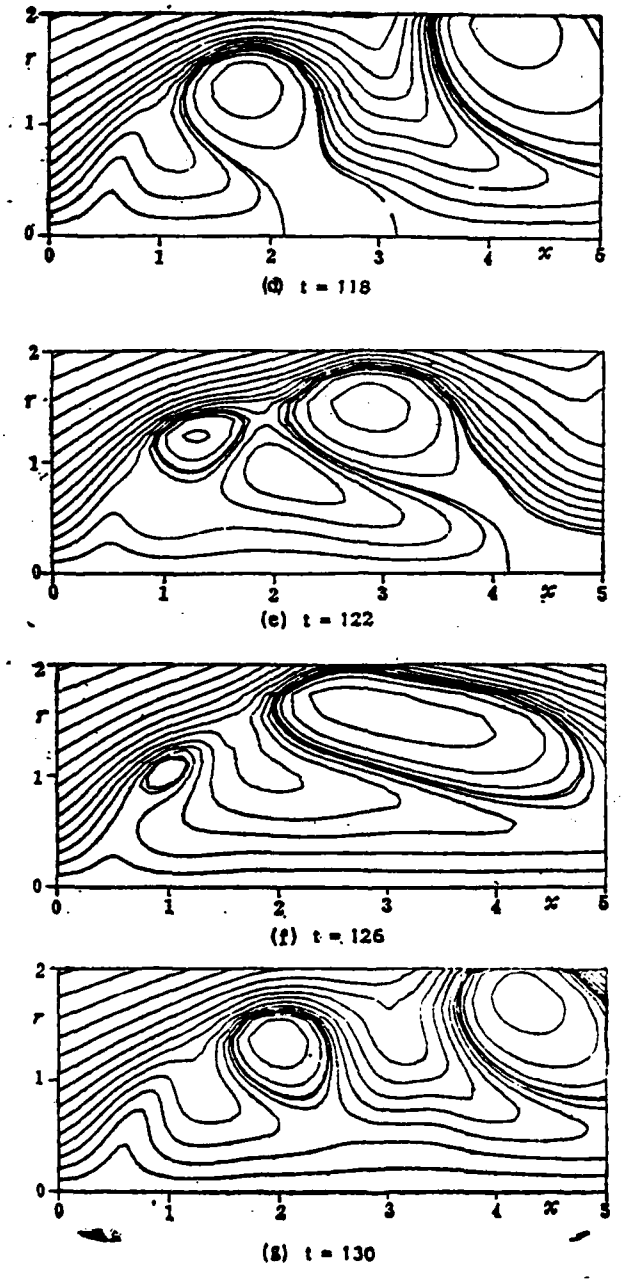

Figure 4. Evolution of Flow Surface of Breakdown of Axisymmetric Vortex (Re=200, U_0=1, Γ_0=0.8944

The periodicity of the unstable vortex flow in our numerical results is qualitatively in agreement with the experimental observation made by Sarpkaya (1971), and Faler and Leibovich (1978).

If we assume that the flow becomes unstable with respect to /28 any non-axisymmetric disturbance after the breakdown of the "axisymmetric" bubble, then the inner cells which periodically flow downstream might be the spiral wake following the breakdown of a bubble as observed in the experiment.

In agreement with the conclusions obtained with the quasi-cylindrical approximation, when the complete N-S equations are used in the calculation, as far as whether the vortex breaks down or not, the results totally coincide with those calculated based on Re=100 and 200. The solid line in Figure 3 represents the vortex breakdown boundary calculated based on the complete N-S equations for an unsteady flow. It is between the curve obtained based on the quasi-cylindrical approximation and the curve (dotted) obtained by Grabowski and Berger (1976) based on the N-S equation for a steady flow. However, they are very close.

Figure 3 also shows the critical curve (double dotted line) separating super critical upstream flow from subcritical upstream flow as obtained by Mager (1972) based on Benjamin's checking equation (1962). Based on the figure, just as Grabowski and Berger (1976) pointed out, many breakdown solutions were obtained with subcritical upstream conditions. It is not in agreement with Squire's critical flow theory and Benjamin's finite transition theory. Parallel calculations based on the

quasi-cylindrical approximation also proved that these subcritical upstream flows would definitely lead to vortex breakdown. The parabolic nature of the quasi-cylindrical approximation equations eliminates the possibility of the propagation of any disturbance upstream. Hence, the vortex breakdown thus calculated could not be explained based on the upstream propagation of disturbance. Several experiments conducted in pipes also indicate that when the flow remains unchanged and the rotation is strengthened, as the subcritical nature of the upstream flow is strengthened based on Mager's critical curve, only the breakdown point is moved up and the pattern is changed. It does not mean that the breakdown disappears. Therefore, the only conclusion we could reach is that vortex breakdown is indeed independent of the subcritical nature of the upstream flow.

IV. Conclusions

In this paper the breakdown of an isolated axisymmetric vortex embedded in a uniform flow was investigated through the numeric integration of the N-S equations at relatively low Reynolds numbers.

First, the N-S equations were simplified by the quasi-cylindric approximation. Its solution can be numerically determined step by step along the x-direction. The results show that it is an excellent approximation of the actual flow for a stable vortex. Any sudden deceleration of the axial flow and

divergence of the calculation can be considered as a sign for vortex breakdown. Furthermore, vortex breakdown is very sensitive to changes in vortex strength.

Then, the N-S equations for an unsteady axisymmetric flow are numerically integrated. If vortex breakdown does not take place, the solution will approach a steady state. Otherwise, the solution will remain unsteady. A re-circulation zone will appear near the axis. Its shape and internal structure are very similar to those of the breakdown bubble observed experimentally by Faler and Leibovich (1978). Under appropriate combinations of flow parameters, the flow will appear periodic after some time.

The results of both methods show that as far as the relatively low Reynolds numbers covered by our calculations are concerned, vortex breakdown is not very closely related to Reynolds number. Moreover, it is independent of the critical classification of the upstream flow.

References /29

[1] Benjamin, T.B., Journal of Fluid Mechanics, 14, (1962), 593-629.

[2] Benjamin, T.B., Journal of Fluid Mechanics, 28 (1967), 65-84.

[3] Bossel, H.H., Rep. AS-67-14, Ph. D. thesis. Univ. Calif., Berkeley (1967).

[4] Bossel, H.H., Phys. Fluids, 12, (1969), 498-508.

[5] Faler, J.H. and Leibovich, S. Journal of Fluid Mechanics, 86 (1978), 313-335.

[6] Gartshore, I.S., NRC Can. Aero. Rep. LR-343 (1962).

[7] Gartshore, I.S., NRC Can. Aero. Rep. LR-378 (1963).

[8] Grabowski, W.J. and Berger, S.A. Journal of Fluid Mechanics, 75 (1976), 525-544.

[9] Hall, M.G., Aero. Res. Counc. R. & M. 3467, (1965).

[10] Hall, M.G., Proc. Aeronaut. Sci. 7 (1966), 53-110.

[11] Hall, M.G., Proc. 1967 Heat Transfer Fluid Mech. Inst., 319-340, Stanford Univ. Press.

[12] Hall, M.G., Ann. Rev. Fluid Mech. 4 (1972), 195-218.

[13] Kopecky, R.M. and K.E. Torrance, Comput. Fluids, 1 (1973), 289-300.

[14] Lavan, Z., Nielsen, H. and Fejer, A.A. Phys. Fluids, 12 (1969), 1747-1757.

[15] Leibovich, S., Ann. Rev. Fluid Mech., 10 (1978), 221-246.

[16] Ludwieg, H., Z. Flugwiss., 10 (1962), 242-249.

[17] Ludwieg, H., Dtsch, Luft-u. Raumfahrt Rep. 70-40 (1970).

[18] Mager, A., Journal of Fluid Mechanics, 55 (1972), 609-628.

[19] Peckham, D.H. and Atkinson, S.A., Aero. Res. Counc. CP 508 (1957).

[20] Sarpkaya, T., Journal of Fluid Mechanics, 45(1971), 545-559.

[21] Squire, H.B., Aero. Dept., Imperial Coll., London, Rep. 102 (1960).

Environmental Study on Turbulent Boundary Layer Separation /30

Wei Qingding

(Department of Mechanics, Beijing University)

Introduction

Boundary layer separation, as well as effects such as stalling and choking, are very important problems. This is not only because great difficulties and losses of aircraft and various fluid equipment may be the result of stalling and choking, but also because such equipment is often in its optimum operating condition prior to stalling and choking. Therefore, it is very important to clearly grasp the mechanism of flow separation and to effectively predict and control separation. It is a very practical topic. Over the years, many researchers dedicated their work in this area. Considerable progress has been made in theory and application as well. The successful application of boundary layer control on aircraft is an example. Nevertheless, we cannot say that we clearly understand boundary layer separation, especially the separation of a turbulent boundary layer. Many studies just begin to become more in-depth. Due to the unsteadiness of turbulence and difficulties in dealing with three-dimensional and random problems, there are special difficulties in treating theoretical and experimental aspects of turbulent boundary layer separation. In terms of experimental research, there was almost no effective means to study the flow structure of turbulent boundary layer

separation before the 70's. In the early 50's, although Schubauer, G.B. and Klebanoff, P.S.[1] did some fine work using available measuring techniques, the understanding gained on the boundary layer was limited to the classical model. Not only the changing nature of turbulent boundary layer separation was not involved, but also the flow structure in the separation zone was touched. As flow visualization techniques, hot wire techniques and laser technique made progress, it was clear in the 60's that a turbulent boundary layer is very different from a laminar boundary layer. Laminar flow separation is always along a clear line-a two or three dimensional separation line. Turbulent flow separation, however, is a transient process, from weak to strong. Sandborn, V.A. and Kline, S.J. (1961)[2] called the former steady or defined separation and the latter the changing or intermittent separation. Nevertheless, they did not quantitatively describe the transient nature of turbulent flow separation. After the 70's, many researchers used techniques such as flow visualization, hot line and laser to do a great deal of delicate studies on the turbulent boundary layer separation zone to bring the experimental work on turbulent boundary layer into a new quantitative stage. Simpson[3-7] et al and Kline[8-10] et al have systematically worked in this area. Simpson, in particular, used laser, hot wire, and hot film techniques to systematically measure various flow parameters in the turbulent boundary layer separation zone. The author, under the guidance of Professor Hiroshi Sato[11-13], began to conduct a delicate investigation on the turbulent boundary layer separation zone by using hot wire

techniques such as a compound probe for wind speed and direction as well as by using a smoke flow visualization technique. In particular, the effect of velocity distribution of the main flow on turbulent boundary layer separation was investigated based on dynamic characteristics. In addition, the effect of large scale motion upstream on the intermittent separation of turbulent boundary layer was also studied. This paper briefly describes our work. In order to facilitate the comparison, the study done by Simpson et al is also appropriately introduced.

Manuscript received on June 20, 1984

II. Primary Methods in Studying Turbulent Boundary Layer Separation /31

1. Experimental Apparatus

The experimental apparatus should be able to fully develop a turbulent boundary layer and cause its separation at a negative pressure gradient. Our work was conducted in the 1m×1m×5m experimental section of a low velocity wind tunnel as shown in Figure 1. Due to the tripping wire, the flow creates a turbulent boundary layer over the plate which separates on the parabolic surface because of negative pressure. Upstream the plate, there are devices to create velocity and temperature cross-sections. The apparatus used by Simpson was a wind tunnel with a curved top plate such as the one shown in Figure 2. The curved wall was designed to create a pressure distribution similar to that on the wing cross-section. The turbulent boundary layer was formed by

the tripping effect of the dull leading edge of the plywood. These two specific devices and other published experimental apparatus are limited to the two-dimensional case.

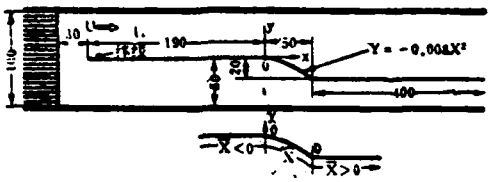

Figure 1. Longitudinal Cross-section of the 1m×1m×5m Low Velocity Wind Tunnel and Its Coordinate System

1. tripping wire

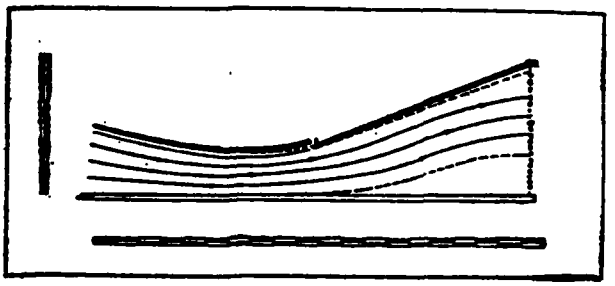

Figure 2. Schematic Diagram of the Experimental Section Used By Simpson to Study Turbulent Boundary Layer. Each major division is 10 inches.

2. Major Testing Equipment

Due to the complexity of the turbulent separation flow, the measuring apparatus must have a specific frequency response (ordinary frequency response at 10 KHz) and directivity (at least capable of recognizing forward reverse flows). Its interference to the flow field must be held at a minimum. Any conventional hot wire tachometer even equipped with an X probe cannot meet the directivity requirement. Simpson et al used laser to aid compound hot wire flow meter and a three wire probe as shown in Figure 3 to make the measurement. This method is simpler than using a laser in probe installation, spatial measurement and data processing. The cost is also lower. However, it cannot measure as close to the wall as the laser. Laser can measure as close as 0.001δ, while a three wire probe can only measure to 0.02δ.

No matter whether a laser or a hot wire is used, a computer /32 is needed to process the data rapidly. In our experiment, we used an on-line real time data processing system.

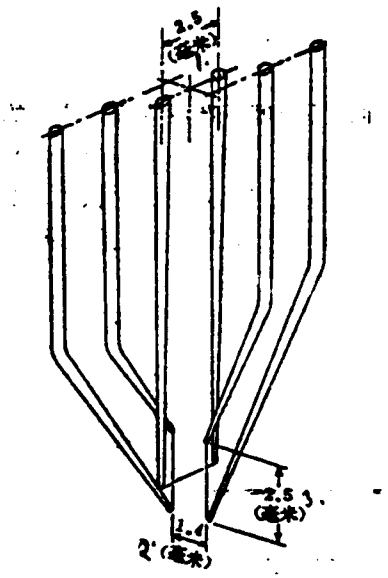

Figure 3. Three-wire Wind Speed Wind Direction Probe

1. mm
2. mm
3. mm

Flow visualization techniques are important in studying the separation of a turbulent boundary layer. Due to the fact that a turbulent flow field is a random three-dimensional unsteady flow field, a laser or hot wire flow meter which measures a point can only provide some instantaneous or statistical information at that point. A flow visualization technique, however, can be used to obtain the flow pattern of the entire field. Accurate flow visualization results can also provide quantitative information. In our experiment, we used a smoke method. In addition, we used a multi-channel short exposure photography technique and a controllable condition method to improve the objectivity and

controlability (to select characteristic flow patterns) of flow visualization.

III. Major Experimental Results

1. Statistical Quantity Describing Intermittent Separation of Turbulent Boundary Layer.

The separation of a turbulent boundary layer is intermittent. In the separation area, separation and attachment take place alternately. This can be reflected by the intermittent reverse flow in the flow extremely close to the wall surface. The probability of back flow represents the degree of separation. Let us define a statistical average-back flow rate R_n,

$$R_n = \lim_{T\to\infty} \frac{T_n}{T_p + T_n}$$

where,

$$T_p = \sum \Delta t_{pi}, \quad 0 \le t \le T$$

$$T_n = \sum \Delta t_{ni}, \quad 0 \le t \le T$$

Δt_{pi} and Δt_{ni} are the time intervals over which forward and backward flow occur at the point of measurement, respectively. They are determined by the forward and backward flow signals obtained by the three-wire wind speed wind direction probe (See Figure 4).

Based on the frequency histogram measured with laser, Simpson defined a similar quantity γ_p. It represents the

probability for forward flow. When there is not backward flow, $\gamma_p=1$.

Figure 5 shows the backward flow rate distribution measured when the incoming flow is a 3m/s uniform flow. Figure 6 shows Simpson's results based on an 18m/s uniform flow. These results are similar. There is no back flow upstream, i.e., $R_n=0$, $\gamma_p=1$. At certain spots near the wall ($\hat{x}\approx$20cm in Figure 5 and x≈122.0 in Figure 6), intermittent backward flows of low probabilities begin to appear. Further downstream, the probability of backward flow increases ($R_n\uparrow$, $\gamma_p\downarrow$). The backward flow area in the vertical wall direction becomes thicker. In the deep separation region (around x=50cm in Figure 5 and x>150 in. in Figure 6), the probability for backward flow to occur is greater than 0.90.

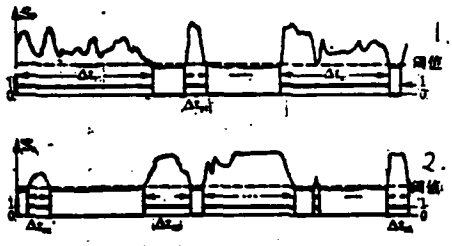

Figure 4. Forward Flow Signal S_p, Backward Flow Signal S_n, and 0-1 Square Wave Defined by Respective Threshold Values.

1. threshold value
2. threshold value

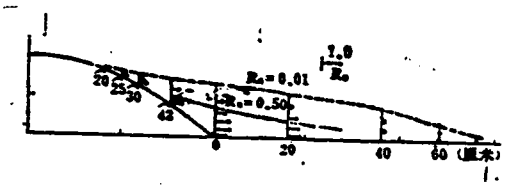

Figure 5. Distribution of Backward Flow Rate R_n at Various Cross-sections in the Separation Area when the Main Flow Wind Speed is 3m/s.

1. (cm)

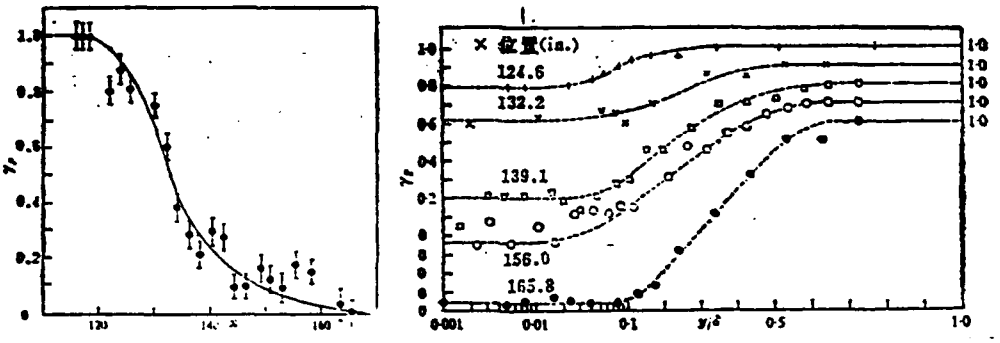

Figure 6. Forward Flow Rate γ_p Distribution in Turbulent Boundary Layer Separation Region Measured by Simpson.

(a) Distribution of γ_p in x-direction along wall surface at 0.25mm height
(b) Distribution of γ_p in five positions

1. position (in.)

2. Flow Visualization of Separation Area

Figure 7 shows the photograph of the flow in the separation region and its upstream area as shown by the smoke line method. The smoke lines are parallel to the wall and perpendicular to the flow. The smoke track shows the instantaneous wind speed distibution 6mm (0.075δ) away from the wall. We can see that

back flow begins to occur at x=12cm. There is not backward flow upstream from this position. Downstream from this position, the back flow region begins to expand gradually. This phenomenon is in agreement with that measured by a wind speed wind direction meter. Figure 8 shows the instantaneous backward flow region shown in Figure 7. We can see the transitional, intermittent and three-dimensional nature of turbulent boundary layer separation.

3. Average Velocity Distribution in Separation Region

In the boundary layer separation region, the direction and magnitude of the instantaneous velocity at every point vary continuously. The average speed we are measuring is the algebraic average of the forward and backward flow.

$$U(x,y)=\frac{1}{N}\sum_{i=1}^{N}U_i(x,y)$$

where N is the number of sampling points and $U_i(x,y)$ is the component of the instantaneous wind velocity on the x-y plane as measured by a wind speed wind direction meter which is positive for forward flow and negative for backward flow.

Figure 9 shows the average wind velocity distribution. As we can see that the backward flow rate is zero at curvature varying points on an average velocity cross-section. At points where the average velocity is zero, the backward flow rate is approximately 0.50. Figure 10 shows similar results obtained by Simpson.

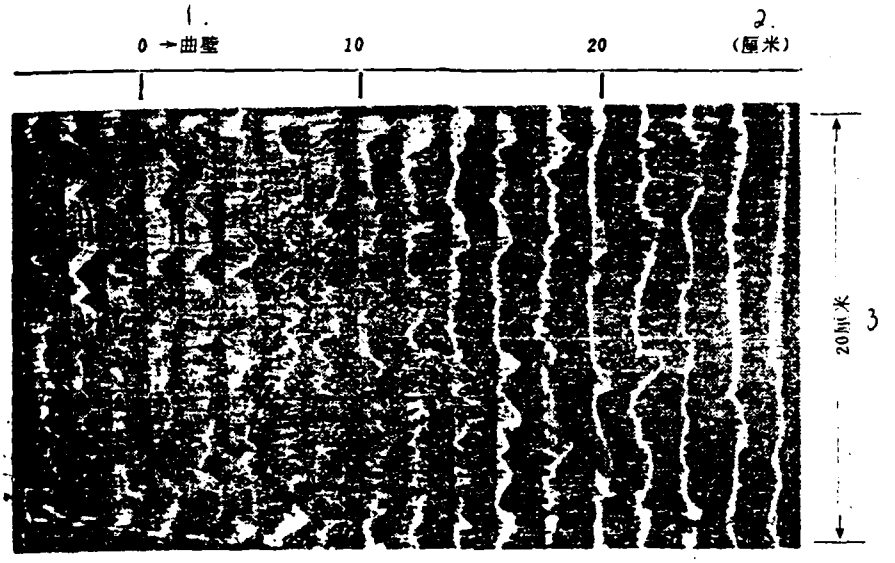

Figure 7. Flow Visualization of Turbulent Boundary Layer Separation Before and After Separation (Smoke Method, Smoke $y_w=0.075\,\delta$ from Wall)

1. curved wall
2. (cm)
3. 20cm

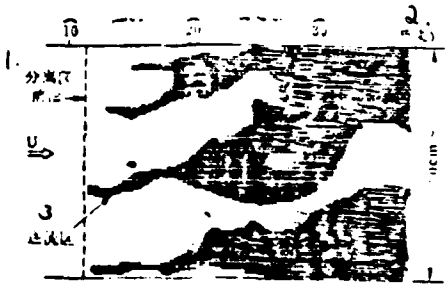

Figure 8. Instantaneous Separation Region in Turbulent Boundary Layer

1. leading edge of separation area
2. (cm)
3. backward flow area

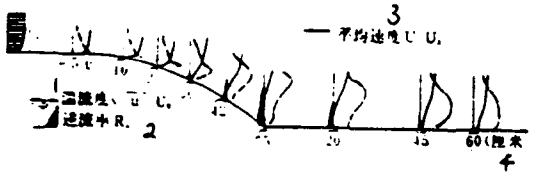

Figure 9. Distribution of Average Velocity, Turbulence and Back Flow Rate in Turbulent Boundary Layer Separation Region (U_b=3m/s)

4. Pulse Velocity Distribution in Separation Region

The curve shown in Figure 9 shows the typical turbulence distribution measured in separation area. As backward flow begins to appear, the corresponding velocity pulse is the maximum. Near the border of the backward flow region (R_n=0.01), velocity pulse is also the highest. Thus, the dimensionless pulse velocity is determined by the following equation:

$$u'(x,y)/U_1=\left[\frac{1}{N}\sum_{i=1}^{N}(U_i(x,y)-U(x,y))^2\right]^{\frac{1}{2}}/U_1$$

where U_1 is the incoming flow velocity.

/35

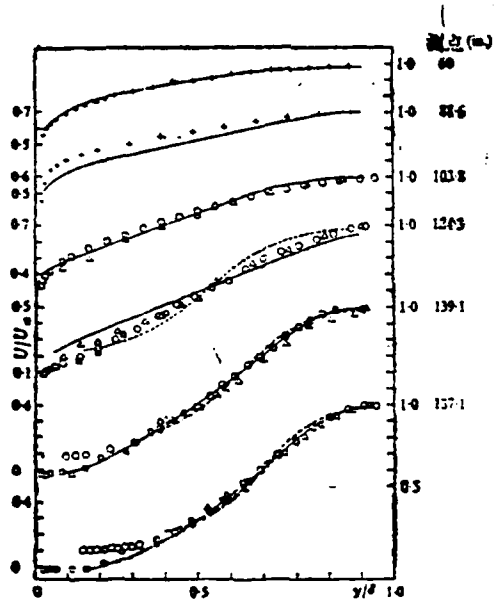

Figure 10. Mean Wind Speed Distribution in Turbulent Boundary Layer Separation Region Measured by Simpson Using Pitot Tube (+), Hot Film (O) and Laser (Δ,□)

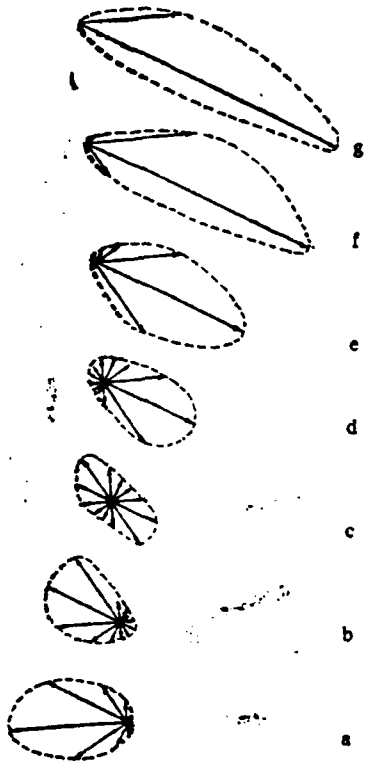

Figure 11. Wind Direction Distribution on xy Plane in Turbulent Boundary Layer Separation Zone ($x=\widehat{55}$,y corresponds to a. 1.0; b. 3.0; c. 5.0; d. 7.0; e. 9.0; f. 11.0; and g. 13.0 (cm), respectively)

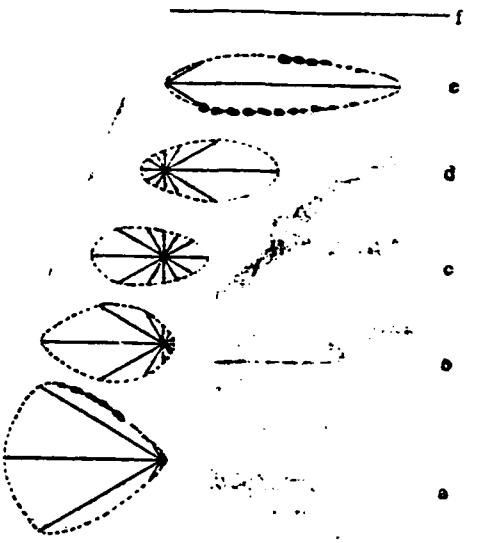

Figure 12. Wind Direction on xz Plane in Turbulent Boundary Layer Separation Zone (x=55,y corresponds to a. 1.0; b. 3.0; c. 5.0; d. 7.0; e. 11.0; and f. 15.0 (cm), respectively)

5. Wind Direction Probability Distribution in Separation /36 Zone

We used 5-wire and 8-wire probes to measure the wind direction probability distribution in the separation zone. Figures 11 and 12 show the wind direction distributions on x-y

and x-z planes, respectively. We can see that in the deeply separated region, the wind direction distribution range covers the entire sphere. Around R_n=0.5, the probability in any direction is very close.

6. Effect of Main Flow Velocity Distribution on Turbulent Boundary Layer Separation

Figure 13 compares the intermittent separation zones which correspond to five main flow velocity distributions (uniform flows at 1m/s, 3m/s and 5m/s as well as uniform positive and negative flows at 3m/s at the boundary layer). It is possible to see that the separation zone corresponding to the negative shear main flow is the smallest. The separation zone corresponding to the main flow with a positive shear flow is the largest. For uniform flows, the separation zone becomes smaller with increasing Re.

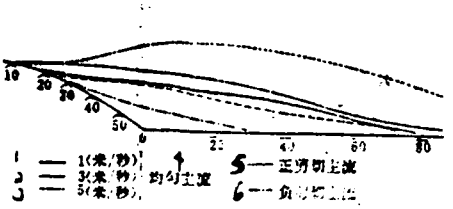

图 13 五种主流速度分布对应的湍流边界层分离区

Figure 13. Turbulent Boundary Flow Separation Zones Corresponding to Five Main Flow Velocity Distributions

1. 1(m/sec)
2. 3(m/sec)
3. 5(m/sec)
4. uniform main flow
5. positive shear main flow
6. negative shear main flow

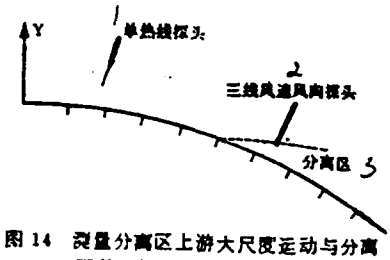

图 14 测量分离区上游大尺度运动与分离区前部间歇性分离相关关系的装置

Figure 14. Apparatus Used to Measure the Correlation Between Upstream Large Scale Movement and Intermittent Separation in the Front Section of the Separation Zone

1. single hot wire probe
2. triple hot wire wind speed and direction probe
3. separation zone

7. Effect of Large Scale Movement Upstream on Intermittent Separation of Turbulent Boundary Layer

Figure 14 is a schematic diagram of the apparatus used to measure the correlation between any large scale movement upstream from the separation zone and the intermittent separation in the

front section of the separation zone. A single hot wire probe was installed upstream. The velocity signal measured is U(t). A wind speed and direction probe was installed downstream in the separation zone. The backward flow signal to be detected is $S_n(t)$. A conditional sampling method was used. The time t_i at which a backward flow appears might be used as the base to measure the velocity signal in the time interval $[t_i-\Delta\tau_1, t_i+\Delta\tau_2]$ (See Figure 15). Figure 16 shows an example of the result of the measured conditional average speed. Based on the conditional sampling average velocity, it is possible to obtain the velocity cross-section changes in a specific time interval. Figure 17 shows the variation of the conditional average velocity on seven cross-sections along the straight and curved walls at seven time intervals within t=-11/30~0 sec. The solid lines represent the conditional average velocity and the dotted lines are the usual average velocity. The velocity in slanted line covered areas are lower than average. They are called "low velocity flow blocks".

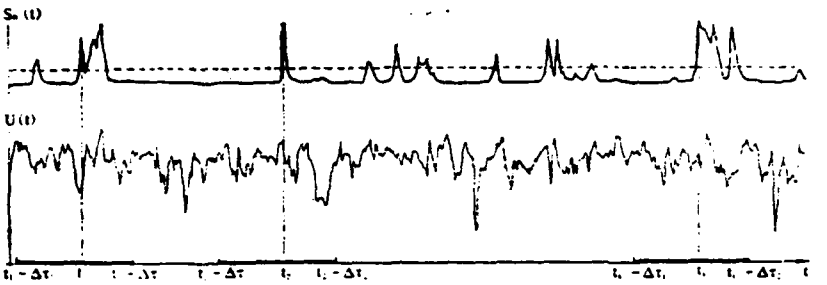

Figure 15. Sampling Conditional Signal $S_n(t)$ and Conditional Sampling Signal U(t)

Areas covered by crossed slanted lines are higher than average velocity areas - called "high velocity flow blocks". Based on /37 the figure, as time progresses, a low velocity flow block flows downstream following a high velocity flow block. When the low velocity block flows by the intermittent separation zone, backward flow occurs. We can thus conclude that any large scale movement upstream can affect intermittent separation. Low velocity flow block is one of the causes for inducing intermittent separation.

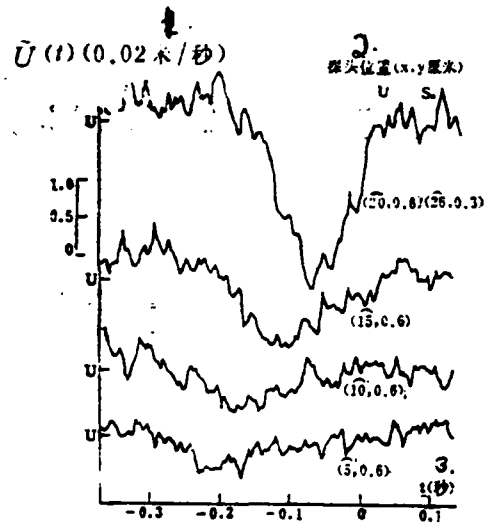

Figure 16. An Example of Conditional Average Wind Velocity

1. U(t) (0.02 m/sec)
2. probe position (x,y cm)
3. t(sec)

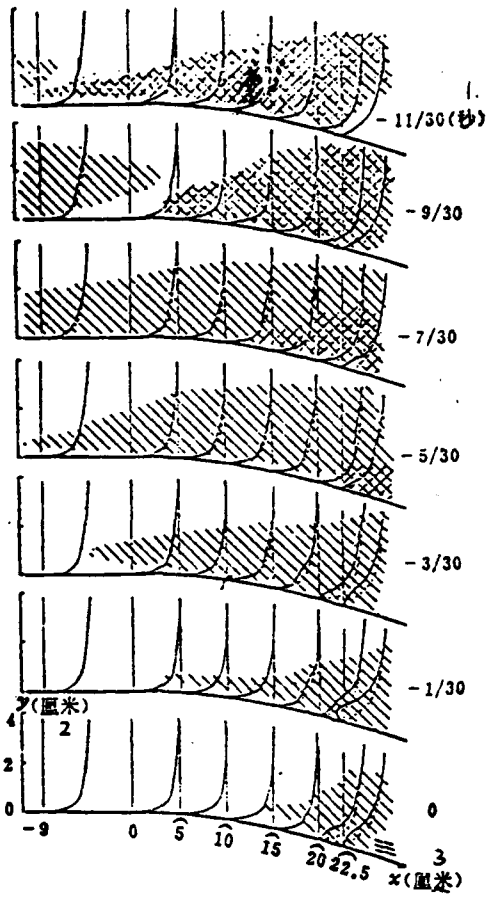

Figure 17. Experimental Results on the Correlation Between the Low Velocity Flow Block Upstream and the Intermittent Variation of the Leading Edge of the Separation Zone

1. (sec)
2. (cm)
3. (cm)

IV. Major Conclusions and Discussion

The separation of a turbulent boundary layer is intermittent, transitional and three-dimensional. It is possible to use forward and reverse flow rates to describe the extent of separation. The distributions of certain statistical averages such as average velocity and pulse velocity is related to the distribution of backward flow rate. The velocity distribution of the main flow will determine the ease of separation. Large scale upstream motion will affect the intermittent separation of tne turbulent boundary layer.

The primary objective to study turbulent boundary layer separation is to predict and control boundary layer separation. The purpose of the experiment is to clarify the physical nature of the flow phenomenon, and to provide effective theoretical models or empirical or semi-empirical formulas. Due to the complexity of the problem, these tasks are not yet accomplished.

References /38

[1] Schubauer, G.B. & Klebanoff, P.S., NACA Report 1030 (1951).

[2] Sandborn, V.A., Kline, S.J., Journal of Basic Engineering, September, P. 317 (1961).

[3] Simpson, R.L., Phys. Fluids Vol. 18, P. 1068-1069 (1975).

[4] Simpson, R.L., Strickland, J.H., Barr, P.W., J. Fluid Mech. Vol. 79, Part 3, P. 553 (1977).

[5] Simpson, R.L., Chen, Y.T., Shivaprasad, B.G.,J. Fluid Mech. Vol. 113, P. 23-51 (1981).

[6] Simpson, R.L., Chen, Y.T., Shivaprasad, B.G.,J. Fluid Mech. Vol. 113, P. 53-73 (1981).

[7] Shlloh, K., Shivaprasad, B.G., Simpson, R.L., J. Fluid Mech. Vol. 113, P. 75-90 (1981).

[8] Kline, S.J., Journal of the Aeronautical Sciences Vol. 24, P. 470 (1959).

[9] Kline, S.J., Journal of Basic Engineering, Trans. ASME, Series E, Vol. 81, P. 305 (1959).

[10] Kline, S.J., Runstadler, P.W., Journal of Applied Mechanics Vol. 26, Trans, ASME. Series E, Vol. 81, P. 166 (1959).

[11] Wei Qingding and Hiroshi Sato, Reverse Flow Rate in Turbulent Boundary Layer Separation Zone, Symposium of the 12th Annual Meeting of Japanese Fluid Dynamics Society, (1980, 10).

[12] Qing-ding Wei, Hiroshi Sato, The role of large-scale motions in the separation process of a turbulent boundary layer on a curved surface, structure of complex turbulent shear flow IUTAM Symposium Marseille (1982).

[13] Wei Qingding and Hiroshi Sato, Structure of Turbulent Boundary Layer Separation with Velocity Gradient in Main Flow, Journal of Japanese Fluid Dynamics Society, Vol. 1 (1982).

Turbulent Boundary Layer Characteristics In and Out of Separation Region Measured at Wing-Plate Junction at Low and Subsonic Speeds /39

Xin Dingding and Deng Xueying
(Beijing Institute of Aeronautics and Astronautics)

Abstract

This paper presents the three-dimensional turbulent boundary layer measurement made in and out of the separation region at the wing-plate junction at low and subsonic speeds. In the low speed experiment, the distributions of the three average velocity components and six turbulent stress components at ten stations along two lines were measured. At subsonic speeds, similar measurements were made at two stations in and out of the separation region. The results show that separation induces the formation of a horseshoe shaped vortex, which is an important factor affecting the behavior of the three-dimensional boundary layer in and out of the separation region. In addition, method to process experimental data is also discussed. Experimental results influenced by pressure gradient and streamline curvature were also analyzed.

Symbols

A,B,C,D,E,F	coefficients in equation (6) and (7)
c,h	coefficients in equation (3)

E_c	voltage output from linearizer
e_c	pulse of voltage output from linearizer
K	hot wire calibration index in equation (2)
M	local Mach number
M_∞	incoming flow Mach number
ΔM	deviation in Mach number distribution
P	static pressure of flow
T	static temperature of flow
u	local flow velocity
u_∞	incoming flow velocity
u_e	velocity at outer edge of boundary layer
u_{eff}	cooling rate of hot wire in equation (2) and (3)
u_x, u_y, u_z	velocity components along (x,y,z) axes
u_s, u_y, u_n	velocity components along (s,y,n) axes
U_T, U_N, U_B	velocity components along (T,N,B) axes
$\overline{(u_s' u_n')}$	$= \overline{(\rho' u_s' u_n')}/\bar{\rho}^2$, mass weighted shear stress
α, ψ, β	angles indicating the orientation of the hot wire (See Figure 3)
ρ	density of flow

superscript

(-)	time average or mean value
(')	fluctuation

subscript

A,B	output signals from hot wires A and B

Manuscript received on July 15, 1984.

The velocity of the flow along the plate is gradually decreasing due to the wing installed on the plate. The streamline is bent. The three-dimensional turbulent boundary layer thus created will eventually separate. A separation region will be formed at the junction of the wing and the plate. Separation will lead to the formation of a horseshoe shaped vortex to complicate the flow in this region. This complicated phenomenon often occurs on aircraft and other fluid equipment, affecting the performance of such devices. Flow separation and its effect on the flow itself will affect the behavior of the turbulent boundary layer in and out of the separation region. Nevertheless, we know very little about it.

In this area, Shabaka and Bradshaw[1] did some experimental work on the decay of the horseshoe vortex at low speeds. McMahon[2] measured the velocity and turbulence distribution of the junction at low speeds. The focus of this work is placed on the effect of separation on the turbulent boundary layer in and out of the separation region. The barrier method used by other people are plates with an elliptical leading edge. Moreover, the point of measurement is located far away from the leading edge and the local pressure gradient is zero. Hence, the behavior of turbulence measured does not include any pressure gradient effect. In this work, the straight wing used has a thickness ratio of 25% (See Figure 1). The purpose is to enhance the strength of the separation vortex to intensify its effect on the

turbulent behavior. Furthermore, due to the fact that a straight wing is used, the work can more truthfully reflect many practical situations.

In this work, two measuring cross-sections were chosen at low speeds. One is at 18.75% chord length. It is 135mm from the leading edge of wing and is perpendicular to the chord (See Figure 1). It is relatively far away from the leading edge and the upper and lower surfaces are parallel. Thus, the pressure gradient is very small. The other is on the line 45^{o} from the chord near the leading edge. The pressure gradient and curvature of streamline are relatively large over there. Five measuring stations were selected on each cross-section, to be located in and out of the separation region. At each station, the average velocity and the distribution of the six turbulent stress components of the turbulent boundary layer were measured. At subsonic speeds, a station was selected in and out of the separation region (See Figure 2) to determine the average velocity and turbulent stress.

AD-A174 599 ACTA AERODYNAMICA SINICA(U) FOREIGN TECHNOLOGY DIV 2/3
WRIGHT-PATTERSON AFB OH Z HANXIN ET AL 03 NOV 86
FTD-ID(RS)T-0367-86

UNCLASSIFIED F/G 20/4 NL

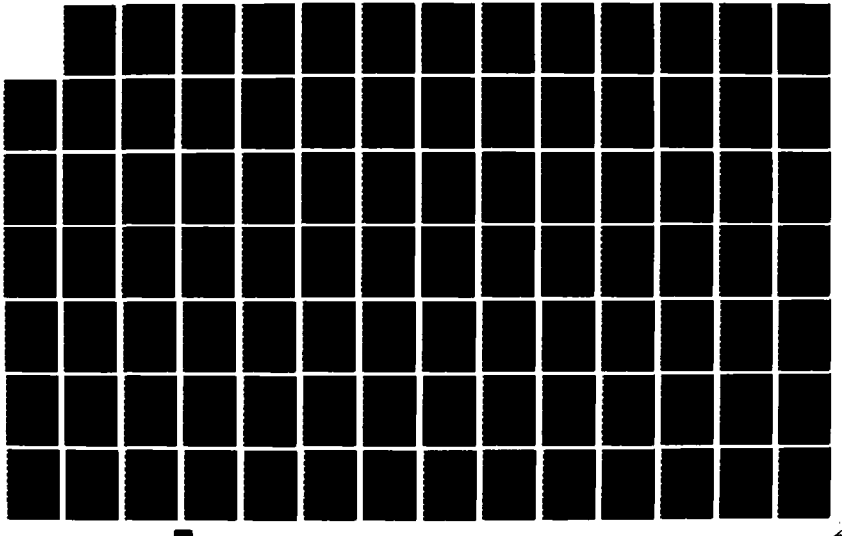

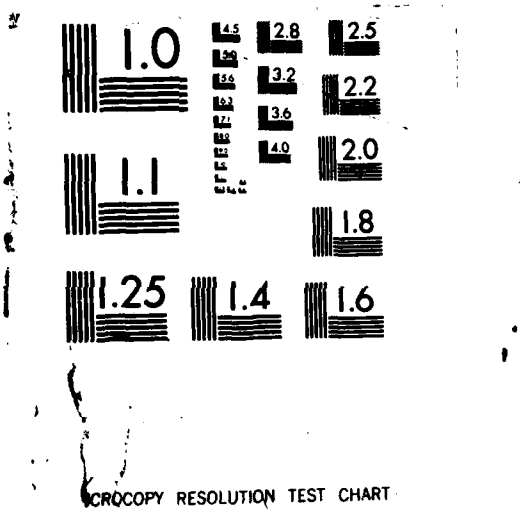
1.0
1.1
1.25
1.4
1.6
2.8
3.2
3.6
4.0
2.5
2.2
2.0
1.8
CROCOPY RESOLUTION TEST CHART

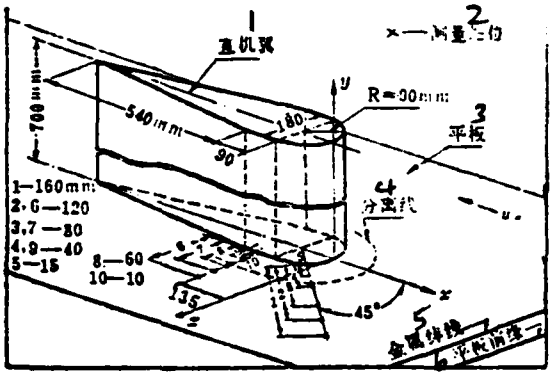

Figure 1. Installation of the Vertical Wing Model and Positions of Boundary Layer Measuring Stations at Low Speeds.

1. vertical wing
2. measuring station
3. plate
4. separation line
5. metal trip wire
6. plate leading edge

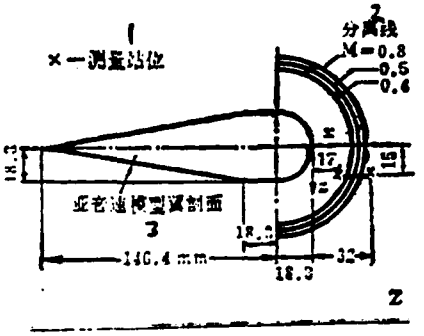

Figure 2. Wing Section of Subsonic Model and Location of Boundary Layer Measuring Stations

1. measuring station
2. separation line
3. subsonic mode wing section

II. Experimental Apparatus /41

Wind Tunnel

Low speed experiments were carried out in the 92x92cm section D-2 wind tunnel at Beijing Institute of Aeronautics and Astronautics. When the wind speed is 16m/sec, the turbulence in the center of the flow field is 0.5%. Non-uniformity of velocity pressure distribution is less than 0.7%. Deviation of flow direction is less than 0.5^{o}. The Reynolds number per meter is approximately $1x10^{6}$.

Subsonic experiments were done in the G-3 wind tunnel at Beijing Institute of Aeronautics and Astronautics. This is a blow down wind tunnel. Its subsonic and transonic speed experimental section is 53.5x37.5cm. The left and right walls are fixed. The upper and lower walls are open. At M=0.4, Re number per meter during the experiment is approximately $1x10^{7}$. The turbulence is $\approx$1%. The non-uniformity of M distribution is

$$\left|\frac{\Delta M}{M}\right| < 0.004$$

Vertical Wing Model and Measuring Plate

The head of the vertical wing on the measuring plate is semi-circular. It is immediately followed by a straight section from 12.5% to 25% chord length. Afterward, the thickness gradually decreases until the trailing edge. The plate used to make the measurements in low speed experiments was horizontally

installed at 22cm away from the lower wall of the wind tunnel. The top of the vertical wing model is right next to the upper wall of the wind tunnel. The bottom is immediately next to the measuring plate. The span of the subsonic model is equal to the width of the experimental section. The model was sandwiched tightly between two side walls. One of the side walls was used as the plate to measure the behavior of its boundary layer. When low and subsonic speed experiments were conducted, a 0.5mm metal trip wire was placed near the leading edge of the plate to ensure that a fully developed turbulent boundary layer exists on the plate.

Measuring Instruments

The average velocity and turbulence of the boundary layer were measured by an "x"-shaped dual hot wire probe. Using a turning mechanism, it was possible to move the probe up and down perpendicular to the plate in the process. The probe could also be moved around the point of measurement. This mechanism is driven by a step motor which can be operated outside the wind tunnel by using a controller. The minimum displacement controllable is 0.01mm. The minimum angle of rotation is 0.1^{o}.

Other instruments required in the measurements include: an anemometer and a barometer to measure wind speed and dynamic pressure, thermocouple thermometers to measure total temperature of the flow and wall temperature, and a Model TSI 1050 constant temperature hot wire anemometer and its accessories, such as linearizer, correlator and RMS voltmeter for hot wire

measurements. The experimental data were read on the RMS voltmeter or sent into a data acquisition system (Model XJ-200 scanner) which was connected to a computer. In high speed experiments, the data acquisition system can also gather the temperature of the stable section and the wall temperature of the experimental section with thermocouples as well as total pressure of the stable section, the static pressure on the wall in the experimental section and the static pressure at the measuring point. The data can then be processed by a computer (DJS-130) before the final results are made available.

III. Experimental Method

In order to measure the three velocity components and six turbulent stress components at a point in space with a hot wire probe, it is necessary to determine the orientation and position of the hot wire. To this end, three coordinate systems are introduced (See Figure 3): the wind tunnel coordinate system x-y-z which is fixed on the plate, the local wind direction coordinate system s-y-n, and the coordinate system T-N-B which is fixed on the hot wire. On the plate, the x-axis points at the incoming flow direction; s-axis points at the projection of the local current on the plate. The y-axis is perpendicular to the plate, pointing upward. T-axis is along the direction of the hot wire. N-axis is perpendicular to the hot wire in the plane formed by the T-axis and by the hot wire rotating axis. The included angle between the N-axis and y-axis is a. The included angle between s-axis and the hot wire projected on the s-n plane is ψ. The included angle

between s-axis and x-axis is β. Once the distribution of β along y-direction is known, it is possible to determine the s-axis direction along y. In order to measure β, an "x"-shaped hot wire /42 probe with α=0 should be used. The line equally dividing the angle between the two hot wires should coincide with the x-axis. The value of β can be calculated according to the following:

$$\beta = \mathrm{tg}^{-1}\left(\frac{E_{c_A} - E_{c_B}}{E_{c_A} + E_{c_B}}\right) \tag{1}$$

where Ec_A and Ec_B are the linearized voltage signals from the two hot wires. By choosing the proper ψ and α, components of average velocity and turbulence of each point in the T-N-B coordinate system along y-direction in the boundary layer can be obtained. Based on coordinate transformation, their components in the s-y-n coordinate system can then be obtained. Finally, they are transformed to the x-y-z coordinate system. Thus, the average velocity and turbulence at any point normal to the plate in the wind tunnel coordinate system can be obtained.

Specifically, experimental data are processed as follows. The effective velocity to cool the hot wire is introduced as U_{eff}. Then, the linearized voltage output is linear in relation with varying ρU_{eff}; i.e.,

$$E_c = \frac{\rho U_{eff}}{K} \tag{2}$$

where K is a proportionality constant which can be determined by calibrating the hot wire. Obviously, the cooling speed U_{eff}

ought to be a function of U_N, U_T and U_B. Here, let us introduce the expression used by Jorgensen[3]:

$$U_{eff}=(U_N^2+c^2U_T^2+h^2U_B^2)^{1/2} \tag{3}$$

where U_T, U_N and U_B are velocity components along T-N-B axes, respectively. Coefficients c and h still must be determined by calibrating the hot wire. If the orientation of the hot wire, α and ψ, is known, it is very easy to derive the relation between the velocity components U_T, U_N, U_B and their corresponding velocity components $u_s+u'_s$, $u_y+u'_y$, u'_n on the s-y-n coordinate system (where u_s and u_y are average values, and u'_s and u'_n are fluctuations). Based on equation (2), E_c can be expressed as

$$E_c=E_c[\rho(u_s+u'_s),\ \rho(u_y+u'_y),\ \rho u'_n;\ \psi,\alpha] \tag{4}$$

and

$$E_c=\bar{E}_c+e_c \tag{5}$$

where $\bar{E}_c$ and e_c are the mean and fluctuating voltage output from the linearizer, respectively. Let us take the time average of both sides of equation (4) and also take the time average of the square of both sides of equation (4), we get (after omitting higher order terms) the following:

$$\frac{K\bar{E}_c}{\rho}=u_t\sqrt{A}\left[1+\left(\frac{B}{2}-\frac{D^2}{8}\right)\left(\frac{u_s^2}{u_t^2}+\frac{\overline{u'^2_s}}{u_t^2}\right)+\frac{D}{2}\ \frac{u_s}{u_t}+\left(\frac{C}{2}-\frac{F^2}{8}\right)\frac{\overline{u'^2_s}}{u_t^2}+\left(\frac{E}{2}-\frac{DF}{4}\right)\frac{\overline{(u'_su'_n)_s}}{u_t^2}\right] \tag{6}$$

$$\frac{K^2\overline{e_i^2}}{\bar{\rho}^2} = u_i^2 A\left[\frac{\overline{u_i'^2}}{u_i^2} - \frac{D^2}{4}\frac{\overline{u_s'^2}}{u_i^2} + \frac{F^2}{4}\frac{\overline{u_n'^2}}{u_i^2} + D\frac{\overline{(u_i' u_s')_s}}{u_i^2}\right.$$

$$\left. + \frac{DF}{2}\frac{\overline{(u_s' u_n')_s}}{u_i^2} + F\frac{\overline{(u_i' u_n')_s}}{u_i^2}\right] \qquad (7)$$

where the average flow density $\overline{\rho}$ can be obtained based on $\overline{\rho}=\overline{P}/R\overline{T}$ by measuring the static pressure $\overline{P}$ and mean temperature $\overline{T}$. Parameters A, B, C, D, E and F are functions of ψ and α. All velocity fluctuating terms are mass weighted to the following definition[4]:

$$\overline{u_i'^2} = \overline{(\rho u_i')^2}/\bar{\rho}^2 \,, \overline{(u_i' u_j')_s} = \overline{\rho^2 u_i' u_j'}/\bar{\rho}^2 \qquad (8)$$

Similar definitions apply to terms with different subscripts (s,y,n). /43

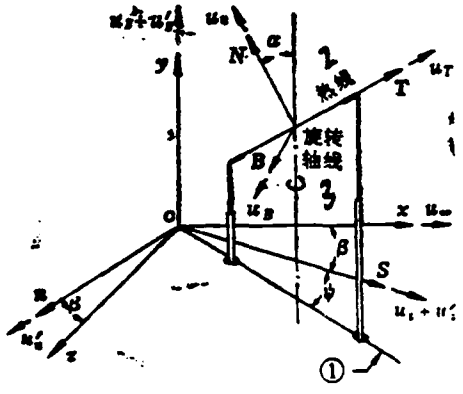

Figure 3. Wind Tunnel, Wind Direction and Hot Wire Coordinate Systems

1. projection of hot wire on s-n plane
2. hot wire
3. axis of rotation

There are eight unknowns in equation (6) and (7). Two of them are average velocity components: u_s and u_y (u_n=0). Six of them are velocity fluctuation related terms which take density variation into account (to reflect six turbulent stress terms):

$\overline{u_{s\rho}'^2}$、$\overline{u_{n\rho}'^2}$、$\overline{u_{y\rho}'^2}$ 和 $\overline{(u_s'u_n')_\rho}$、$\overline{(u_s'u_y')_\rho}$、$\overline{(u_n'u_y')_\rho}$

If different hot wires are used and proper ψ and α are chosen based on the feasibility to be installed in the wind tunnel, equation (6) and (7) can be simplified by various degrees. Thus, experiments can be performed with respect to certain ψ and α to solve equation (6) and (7) by using the values of $\bar{E}_c$ and $\overline{e_c^2}$ measured. The eight unknowns can thus be determined. Through coordinate transformation, the average velocity and turbulence along the wind tunnel coordinate system can be obtained:

u_s、u_y、u_z 和 $\overline{u_{s\rho}'^2}$、$\overline{u_{y\rho}'^2}$、$\overline{u_{z\rho}'^2}$、$\overline{(u_y'u_z')_\rho}$、$\overline{(u_z'u_s')_\rho}$、$\overline{(u_s'u_y')_\rho}$

It can be proven that, under similar conditions to derive equation (6) and (7), it is possible to get $\overline{u_{x\rho}'^2}$, $\overline{u_{y\rho}'^2}$ and $\overline{u_{z\rho}'^2}$ from $\overline{u_x'^2}$, $\overline{u_y'^2}$ and $\overline{u_z'^2}$. The correlation is

$$\overline{u_{s\rho}'^2}=\frac{1}{1+\alpha}\overline{u_{s\rho}'^2},\quad \overline{u_{y\rho}'^2}=\frac{1}{1+\alpha}\overline{u_{y\rho}'^2} \qquad \text{and} \qquad \overline{u_{z\rho}'^2}=\frac{1}{1+\alpha}\overline{u_{z\rho}'^2}$$

where $\alpha=(\gamma-1)M^2$ and the specific heat γ=1.4. As for the correlating experimental data, with the exception of shear at M=0.4, the rest are expressed by conventional turbulent stress terms.

IV. Analysis of Experimental Results

Based on the experimental results, near the separation region, the average speed and turbulent stress are both affected by the main vortex of separation. It is more apparent near the main vortex. In order to clearly illustrate this effect, the experimental curve was organized by x,y,z to directly reflect the actual position of the separation vortex.

(1) First, let us discuss the results measured on the x=135mm cross-section away from the leading edge of the wing. The pressure gradient of this cross-section is $dp/dx \approx 0$. /44 Moreover, the streamline is very straight. Therefore the experimental data obtained is not influenced by pressure gradient and streamline curvature. In this case, some of the characteristics of a uniform flow can be visualized from the velocity vector distribution projected on the cross-section (See Figure 4a). Based on the core position of the main separation vortex (vertical: y=13mm, spanwise: z=50mm) and the induced velocity caused by the separation vortex shown in this figure, we can see that the induced velocity increment is very large in the z-direction near the plate. This induced velocity causes high speed flow away from the wing to be rolled near the vertical wing. The boundary layer thickness is thus reduced. Also, low speed current near the wing is rolled away, causing the boundary layer to become thicker there, and, furthermore, the distribution in the y direction of u_x causes fluctuation in u_x distribution near the main vortex (See Figure 4b).

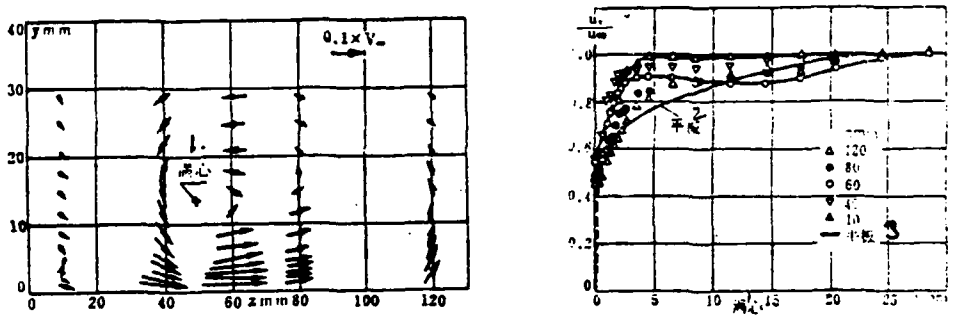

(a) (b)

Figure 4

(a) velocity component distribution on x=135mm cross-section
(b) $u_x/u_\infty \sim y$ curve at various stations at x=135mm

1. vortex center
2. plate
3. plate

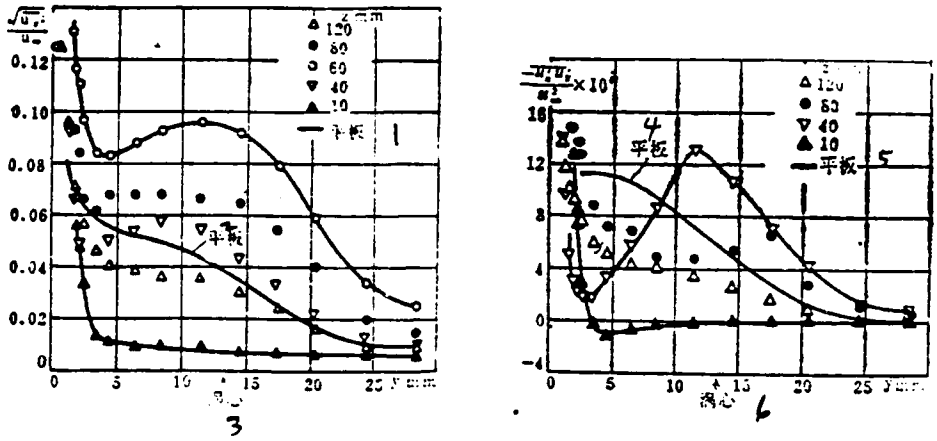

Figure 5. $\sqrt{\overline{u_x'^2}}/u_\infty \sim y$ and $-\overline{u_x'u_y'}/u_\infty^2 \sim y$ Curves at Various Stations at x=135mm

1. plate
2. plate
3. vortex center
4. plate
5. plate
6. vortex center

As for quantities expressing the variation of turbulent stress, $\sqrt{\overline{u_x'^2}}/u_\infty$ vs. y and $-\overline{u_x'u_y'}/u_\infty^2$ vs. y are plotted as examples in Figure 5 (See references [5] and [6] for other turbulent related curves). In the figure, results of the plate without the wing are also presented for comparison in order to see the effect of separation vortex on turbulent stress distribution. Near the main vortex (such as shown by the two curves z=40mm and 60mm), the curve shows a peak near the core (y=13mm). Near the vertical wing (such as shown by z=10mm), turbulence stress decreases

significantly. As compared to the results in reference [2], the peak turbulent stress obtained in this work is much higher. However, the turbulent stress near the vertical wing is much smaller compared to that in reference [2]. This should be related to the fact that the thickness of the model used in this experiment is larger so that the separation vortex strength is consequently higher. In conclusion, the induction of separation vortex causes the turbulence to increase near the main vortex. Consequently, far away from the main vortex, especially near the wing, the turbulence decreases. This phenomenon also appears in /45

$$\sqrt{\overline{u_y'^2}}/u_\infty, \sqrt{\overline{u_z'^2}}/u_\infty \qquad \text{and} \qquad -\frac{\overline{u_y' u_z'}}{u_\infty^2}, \; -\frac{\overline{u_x' u_z'}}{u_\infty^2}$$

vs. y curves (See reference [5]).

(2) Next, let us discuss the results obtained near the leading edge in a cross-section 45° from the chord. In this cross-section, the pressure gradient and streamline curvature are high. Hence, the results are significantly affected by pressure gradient and streamline curvature.

With regard to the average boundary layer flow velocity there, u_x/u_∞ vs. y and u_z/u_∞ vs. y curves are selected for interpretation. Figure 6 shows the distribution of the average velocity component along y-direction in stations at various distances ℓ. In this cross-section, it is obvious that the average velocity near the wing should be higher than that away from the wing. This result is apparently reflected by the group of curves of u_x/u_∞ and $u_z/u_\infty \sim y$. When y is small, (near the

plate), u_z/u_∞ curves vary in a wave form which is a result of the induction effect of the separation vortex. Based on the peak of the curve, the vortex core position is approximately located at y≈ 4mm. Similarly, the induction of separation vortex also causes $u_x/u_\infty \sim y$ curves to fluctuate near the vortex (such as shown by the curve at ℓ=40mm). The position of the vortex center should be located between ℓ=40 and 60mm. The distribution of experimental points on the $u_x/u_\infty \sim y$ curve is similar to that obtained with stations on the x=135 cross-section. Due to the effect of large pressure gradient and streamline curvature, it is even more different compared to the plate curve. Away from the wing (such as shown by curves at ℓ=120 and 160mm), the disagreement between those curves and the plate curve indicates that the velocity model is affected by the negative pressure gradient.

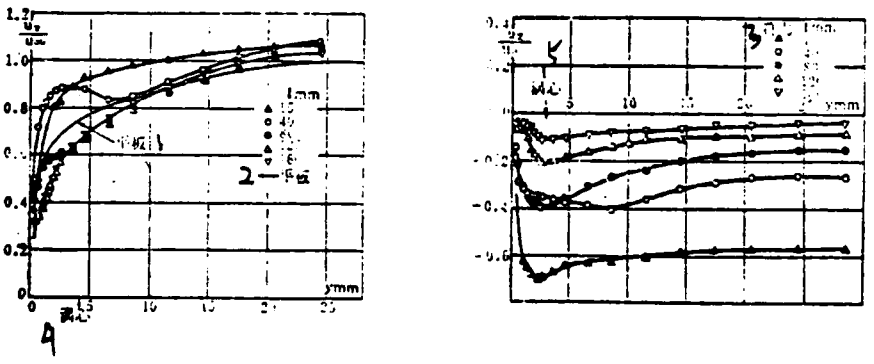

Figure 6. $u_x/u_\infty \sim y$ and $u_z u_\infty \sim y$ Curves Near the Leading Edge in a Cross-section 45° From the Chord.

1. plate
2. plate
3. symbol
4. vortex center
5. vortex center

As for quantities related to turbulent stress, distribution curves of $\sqrt{\overline{u_x'^2}}/u_\infty$ and $-\overline{u_x'u_y'}/u_\infty^2$ were selected and plotted in Figure 7. In the same figure, the experimental curve for the plate is also shown to compare the effect of the wing on turbulent flow behavior. From the figure we can see that the curves show peaks near the vortex center. In addition, the peaks are much larger than those obtained at the x=135mm cross-section. Based on this fact, we can conclude that the vortex has a stronger effect on shear stress. The difference between curves near the wing (such as 1=15mm) and the experiment plate curve is not as large as that at x=135mm. These phenomena show that the area affected by vortex is smaller near the leading edge. The range affected continues to expand, however, as we go further downstream. Hence, negative pressure gradient of the circulating flow has a great impact.

/46

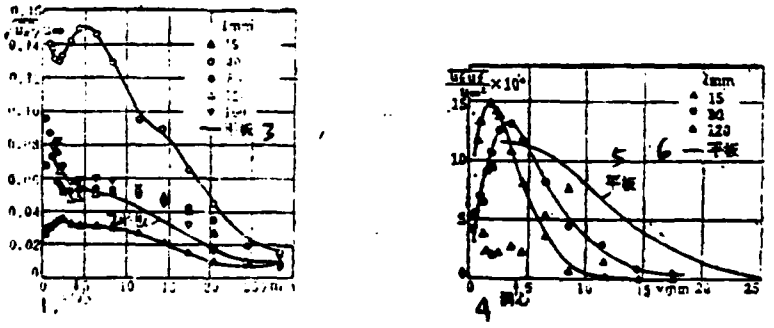

Figure 7. $\sqrt{\overline{u_x'^2}}/u_\infty \sim y$ and $-\overline{u_x'u_y'}/u_\infty^2 \sim y$ Curves Obtained at 45° from the Chord Near the Leading Edge

1. vortex center
2. plate
3. plate
4. vortex center
5. plate
6. plate

(3) In order to understand the changes in turbulent stress behavior in and out of the separation region at subsonic speeds, a station outside the separation region at x=32, y=15mm, and another station in the separation region at x=17, y=15mm (See Figure 2) were chosen to make measurements at subsonic speeds. At M=0.4, $\sqrt{\overline{u_x'^2}}/u_e$, $\sqrt{\overline{u_z'^2}}/u_e$ and $-(\overline{u_x'u_z'})\rho/u_e^2$ vs. y/δ curves were plotted as shown in Figure 8. Based on this figure, the separation vortex is approximately located at $y/\delta \approx 0.1$. Due to the effect of the separation vortex, turbulent stress increases rapidly and peaks there. This phenomena is basically the same as that at low speeds. Similarily, its effect on shear stress is higher quantitatively as compared to that on positive stress.

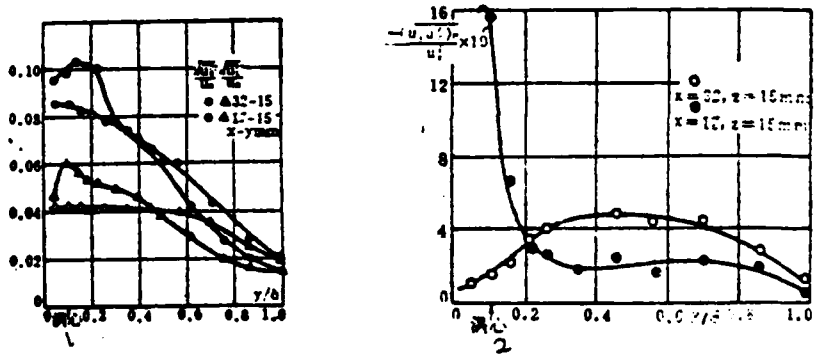

Figure 8. Distribution of Turbulent Stress Related Parameters at Two Stations In and Out of Separation Region at M_∞=0.4.

V. Conclusions

An "x"-shaped twin hot wire probe can be used to measure the boundary layer of separation flow at low and subsonic speeds through the proper choice of orientation angles ψ and α. Related characteristic data can be obtained by an appropriate data processing technique. The experimental results show that the horseshoe vortex caused by flow separation is an important factor affecting the three-dimensional turbulent boundary layer behavior in and out of the separation region.

(1) Effect of Separation Vortex on Mean Velocity Distribution.

The induction effect of the separation vortex causes the /47 boundary layer thickness to decrease inside the separation region, and it also causes the boundary layer thickness to increase out of the separation region. Near the separation vortex, the average velocity shows fluctuations. u_z increases rapidly near the plate. The effect of pressure gradient on average velocity is similar to that on the velocity distribution of the boundary layer of the plate.

(2) Effect of Separation Vortex on Turbulent Stress Distribution.

The separation vortex decreases the turbulent stress near the wing. It increases the turbulent stress near the vortex center and a peak exists. The effect of separation vortex on shear stress is higher than that on positive stress. Near the leading edge of the wing, the separation vortex effect is relatively concentrated around the vortex center. As we go further

downstream, the area affected by the vortex expands larger. The strength decreases and the peak drops. In this case, the negative pressure gradient has some effect.

(3) At subsonic speeds, the effect of separation vortex on turbulent stress distribution is the same as that at low speeds. The effect of the vortex on shear stress is also higher than that on positive stress.

Comrade Ma Shulin of Beijing Institute of Aeronautics and Astronautics also worked on this project. Senior Students Wang Yun and Lu Gan of Aerodynamics Major at Beijing Institute of Aeronautics and Astronautics of the Class of 1983 worked on the low speed experiments. Graduate student, Wang Chaoan worked on the high speed experiments.

References

[1] Shabaka, I.M.M.A. and Bradshaw, P., AIAA J. 19, 131 (1981).

[2] McMahon, H., Hubbartt, J. and Kubendran, L., NASA CR 3605 (1982).

[3] Jorgensen, F.E., DISA IB 11, 31 (1971).

[4] Cebeci, T. and Smith, A.M.O, Analysis of Turbulent Boundary Layers, Academic Press (1974).

[5] Hsing, T.D. and Teng, H.Y., AIAA Paper 84-1529 (1984).

[6] Xin Dingding and Deng Xueying, Technical Report of Beijing Institute of Aeronautics and Astronautics, BH-B 1241 (1984).

Effect of Winglet on Spatial Vortex of a Solid in Rotation at High Angle of Attack /49

Wang Zixing and Wu Genxing
(Nanjing Aeronautical Institute)

Abstract

This paper presents some experimental results on the mechanism of the effect of the winglet on the spatial vortex of a rotating body, The results show that, with the winglet, for a rotating body without skidding, the position of the spatial vortex is lowered because its strength is reduced. Hence, the asymmetric problem at high angle of attack is resolved somewhat by various degrees.

I. Introduction

Lateral force which occurs at high angle of attack without side skidding is primarily due to asymmetric vortices. In order to eliminate and delay the appearance of this undesirable lateral force, many researchers performed force measurements in wind tunnels and presented several solutions. For example, a strake in the front was used [3-6]. However, there is relatively little understanding on the vortex system. On the basis of reference [2], a fluorescent mini-tuft technique[1] was used in this work to clarify the spatial vortex and winglet vortex of a rotating solid in order to understand the role of the winglet in

eliminating asymmetric vortices.

Five different winglet types and arrangements were used to study the spatial vortex of a sharp rotating body at high angle of attack in the absence of side skid in a low speed wind tunnel. The results show that after being equipped with various winglets, the asymmetric vortices of the body of rotation at high attack angles can be suppressed to some extent. The best result was obtained with a small strake at high sweepback angles.

We also used the conventional oil flow pattern method to observe the changes of separation lines after winglets were attached to some models.

II. Experimental Apparatus, Model and Method

1. Experiments were carried out in a 0.75m opening wind tunnel. The wind speed was 30 m/sec. When the model diameter was used as the reference length, the Reynolds number $Re=1.2\times10^5$.

2. The position of the spatial vortex was determined with the assistance of a three coordinate displacement mechanism which was equipped with fluorescent tuft probes. Details of fluorescent tuft visualization technique and spatial vortex measurement are shown in reference [1]. The coordinate of the vortex trajectory was rendered dimensionless by using the length of the body of rotation as a reference.

3. The fuselage size of all five different models remains the same. The total aspect ratio is 7. The aspect ratio at the tip is 3.5. The rear part of the model is cylindrical. The

front of the model is pointed, made of a circular arc. The dimension and position of the winglet is shown in the figure below. The wing is Model NACA 64A 004. The installation angle of the wing surface (with the exception of Model 5) is 0°.

4. Experimentation began from 15° and ended at 60°.

Manuscript received on May 28, 1984. Revised manuscript received on September 5.

/50

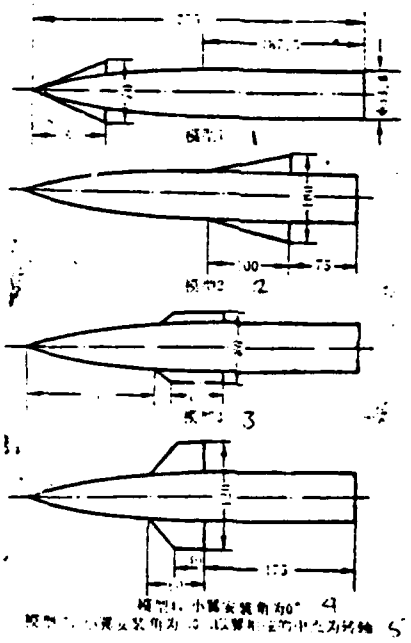

1. Model 1
2. Model 2
3. Model 3
4. Model 4. Winglet installed at 0°
5. Model 5. Winglet installed at 50°. The middle of the wing root chord is used as the axis of rotation.

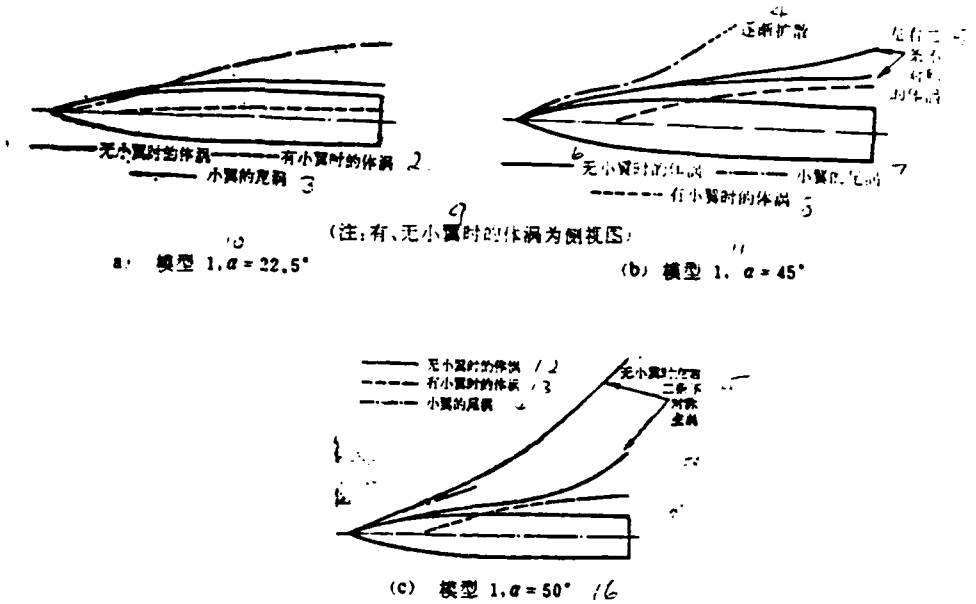

图 1

Figure 1

1. body vortex without winglet
2. body vortex with winglet
3. tail vortex of winglet
4. gradually diffusing
5. asymmetric body vortices
6. body vortex without winglet
7. tail vortex of winglet
8. body vortex with winglet
9. (Note: Body vortices shown without winglet are side views.)
10. Model 1, $\alpha = 22.5^{\circ}$
11. Model 1, $\alpha = 45^{\circ}$
12. Body vortex without winglet
13. body vortex with winglet
14. tail vortex of winglet
15. asymmetric vortices without winglet
16. Model 1, $\alpha = 50^{\circ}$

III. Results and Analysis

1. Small Strake Installed at the Front of a Slender Body (Model 1)

Figure 1 shows how the spatial vortices of a slender body vary with angle of attack with and without a small strake. With /51
a small strake, when the attack angle is not very large (such as $\alpha = 10^{\circ}$). because the tail vortex of the winglet is very close to the axis of the slender body, its induction effect delays the separation of the slender body. Consequently, spatial vortex did not form. When $\alpha = 22.5^{\circ}$, due to the presence of winglet, body vortex could only be formed behind the wing. Its strength is less than that of a wingless slender body. The position is also lower.

As the angle of attack increases ($\alpha > 30^{\circ}$), the wing vortex diffuses gradually. The position and strength of body vortices are obviously suppressed by the winglet so that they cannot develop into an asymmetric vortex system. The tail vortex of the winglet did not roll into the body vortex.

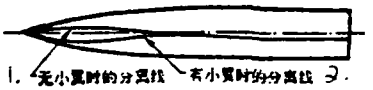

Figure 2. Separation Lines With and Without Winglet

1. separation line without winglet
2. separation line with winglet

Figure 2 was drawn based on oil flow pattern pictures. From the figure we can see that due to the presence of the winglet the position of separation is obviously lowered. The development of the body vortex was delayed.

On the rear part of the model, in addition to a pair of primary vortices, there are a pair of secondary vortices in opposite directions and a pair of relatively weak secondary vortices. In order to avoid confusion due to too many lines, the opposite secondary and secondary vortices are omitted. Only the primary vortices are shown.

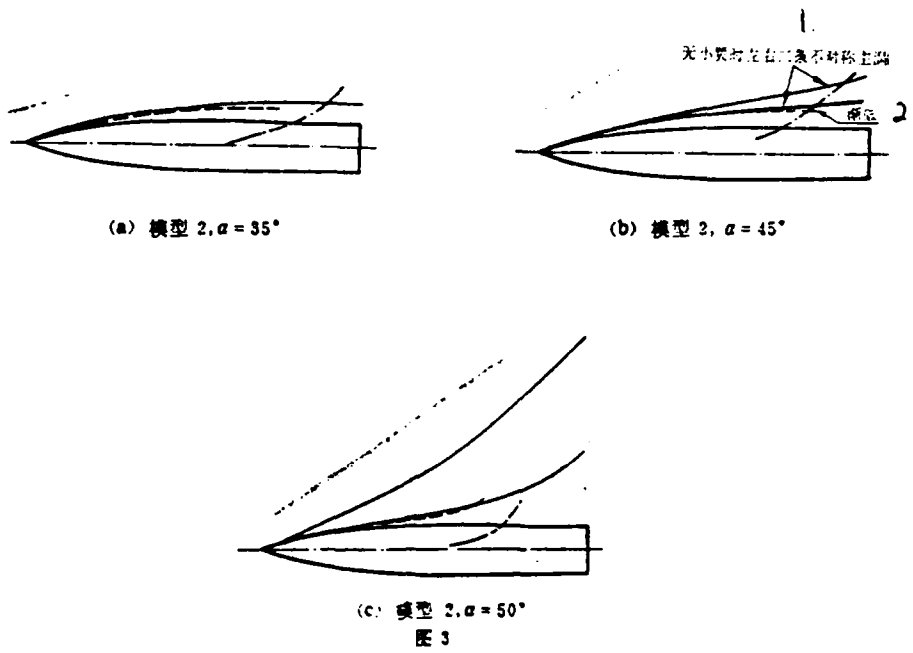

(a) 模型 2, $\alpha = 35°$ (b) 模型 2, $\alpha = 45°$

(c) 模型 2, $\alpha = 50°$

图 3

Figure 3

(a) Model 2, $\alpha = 35^{o}$ (b) Model 2, $\alpha = 45^{o}$ (c) Model 2, $\alpha = 50^{o}$

1. asymmetric pair of vortices without winglet
2. gradual breakdown

2. Small Strake Installed in Mid-Section of Slender Body (Model 2).

Based on Figure 3 we can see that when the attack angle is high (such as $\alpha > 22.5^{o}$), there are two strong front body vortices produced by the head of the body of rotation. In addition, due to the presence of the winglet, a very strong wing vortex exists in the mid-section. The body vortices are lowered by the wing

vortex. Because of the presence of the wing, the vortex generated by the slender body at the wing is not rolled into the front body vortex. Instead, it is rolled into a new body vortex behind the wing. Due to the influence of the wing vortex, the position and strength of the body vortex are suppressed significantly. Thus, the asymmetry of body vortex is alleviated. When the attack angle is greater than 50°, both wing and body vortices are breaking down. Hence, there are no asymmetric vortices. When $\alpha = 60^{\circ}$, wing vortex totally breaks down and body vortices exist only at the head. Due to the effect of the low pressure zone caused by the breakdown of the tail vortex of the winglet, it does not swing upward as in the case where there is no winglet. /52

Figure 4 shows the effect of the winglet on the separation line and on body vortices.

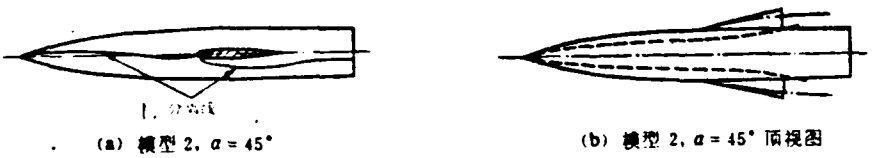

(a) 模型 2, $\alpha = 45^{\circ}$ (b) 模型 2, $\alpha = 45^{\circ}$ 顶视图

Figure 4

(a) Model 2, $\alpha = 45^{\circ}$ (b) Model 2, $\alpha = 45^{\circ}$ Top View

1. separation line

3. Trapezoidal Strake With Small Span Installed in Mid-Section of Slender Body

The situation with Model (3) is similar to that with Model (2). The winglet causes the body vortex to drop. When $\alpha = 30^{o}$, body vortices are merged. As α increases further, the wing vortex breaks down. Body vortices also break because of entering the breakdown zone. As compared to a triangular winglet, the separation breakdown of this type of winglet occurs at a smaller attack angle. Hence, it is less effective in eliminating the asymmetric vortices. However, it will not cause any asymmetry at all.

4. Small Trapezoidal Winglet Installed in the Middle of the Slender Body (Model 4)

The wing vortex produced by the winglet also significantly affects the body vortex to deflect it lower and to weaken it (because it cannot superimpose onto itself in an area where the winglet is). When $\alpha = 22.5^{o}$, the body vortex is induced by the wing vortex and disappears. The wing vortex moves downstream. When $\alpha = 30^{o}$, the wing vortex breaks down. The right and left body vortices are symmetric. They also gradually begin to break down (See Figure 5).

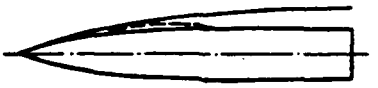

Figure 5

Model 4, $\alpha=30^{\circ}$, Wing vortex already broken down, symmetric body vortices

5. Small Trapezoidal Wing Installed in the Middle of the Slender Body at an Angle (Model 5)

Because it was found experimentally that separation also began at $\alpha=30^{\circ}$ with Model 4, in this test the winglet was installed at -30°. When $\alpha=35^{\circ}\sim 40^{\circ}$, due to the fact that the attack angle of the winglet is only $5^{\circ}\sim10^{\circ}$, the wing vortex was relatively weak. It had little effect on the body vortex. At $\alpha=45^{\circ}$, the wing vortex became stronger. The body vortex was induced downward. As α increased further, the wing vortex intensified more. The body vortex disappeared. Based on this result, as long as the actual attack angle of the winglet is not greater than 30°, it can effectively suppress the asymmetric separation vortex system of a slender body at large attack angles in the absence of side skidding.

IV. Conclusions

This paper introduced a study of separation vortex systems of five types of slender bodies with winglets in a low speed wind tunnel using a fluorescent tuft technique. A intuitive understanding on the effective suppression of the development of asymmetric vortex systems by the winglet was obtained.

1. A winglet, in addition to being capable of suppressing the development of body vortex (partly because there is no input and partly because the separation position is lowered) near itself (shaded area towards downstream), when its spatial vortex has considerable strength, can effectively attract the separation vortex of the slender body so that it will not be deflected upward to develop into an asymmetric vortex system. Thus, the undesirable lateral force can be avoided in the case side skidding is absent. /53

2. Separation occurs when the attack angle of the winglet is too high. Although this is unfavorable for drag, the spatial vortex is sucked into the separation zone. Thus, it is not possible to develop into an asymmetric vortex system.

3. Any bulge on either side of the slender body can reduce, delay or eliminate the formation of an asymmetric vortex system because its tail vortex can, to some extent, suppress and attract the separation vortex of the slender body.

References

[1] Wu Genxing and Wang Zixing, Symposium of China Society of Mechanics on "Flow Field Visualization Techniques and Their Applications" (1982).

[2] Wu Genxing, Wang Zixing and Tian Shizhong, Technical Report No. 1647 of Nanjing Aeronautical Institute (1983, 6).

[3] Keener, E.R., Chapman, G.T., Cohen, T. and Taleghani, J., NASA TMX-3437.

[4] AIAA Paper No. 79-1819.

[5] AIAA Paper No. 80-0181.

[6] J. of Spacecraft and Rockets Vol. 17, No. 6.

[7] J. of Aircraft Vol. 16, No. 11.

On the Investigation of Separated Flow in the Base

Bian Yinqui (Institute of Mechanics) and
Dong Changquan (Beijing Institute of Information and Control)

I. Introduction

Separated flow in the base is an important topic in aerodynamics. In engineering applications, the primary work is to calculate the pressure and heat flow in the base in order to provide a qualitative as well as quantitative description of the flow field structure. Due to the complexity of the base flow field itself, there are not enough experimental data especially in hypersonic range. Methods for theoretical analysis have not yet been perfected. In particular, the study of heat transfer in the base is far behind as compared to the study of pressure in the base. This is because the heating process cannot be reasonably treated easily under the condition that the base flow field structure is not known. Some empirical methods are subject to limitations. Direct solution of the complex N-S equations by numerical methods has not yet reached the level of providing reliable design data. Hence, designers are caught in the middle when choosing the base heat flow data. Based on the nature of the flow field, the flow in the base has many things in common with the separated flow. Similar analytical treatments and numerical methods can also be referenced either way. Regardless whether it is under the influence of an external flow or due to geometric changes on the surface, the flow is separated when a

high pressure area appears. In addition, a re-circulation zone is formed near the wall. Later, the flow rejoins the surface. Similarly, separated flow in the base also includes an external inviscid flow, a free shear layer and a re-circulation zone. The free shear layer is similar to the surface boundary layer. The difference is that both boundaries of the shear layer are unknown. Figure 1 shows a schematic diagram of the separated flow in the base.

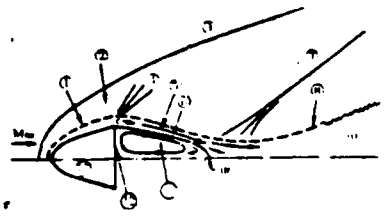

Figure 1. Schematic Diagram of Base Separated Flow

1. boundary layer
2. inviscid flow region
3. shock wave
4. expansion wave
5. free shear layer
6. boundary streamline
7. trailing shock wave
8. turning region
9. expansion core
10. rear stationary point
11. re-circulation region
12. base region
13. dull body

The study of engine jet is another base flow problem. The special feature of a jet flow field is that it is usually a turbulent flow. Furthermore, it is a mixture of chemically reacting gases. A schematic diagram of the jet is shown in Figure 2. The contents of the study include chemical kinetics, turbulent modeling, and numerical simulation.

A simplified analysis usually has the following assumptions: the exit flow field is symmetric with respect to the parallel axis. If the base diameter is much larger than the nozzle diameter, the base re-circulation zone will not significantly affect the entire jet structure. In addition, it is also assumed that there is no radial pressure gradient. Furthermore, some complicated factors are also not considered; such as the effect of shock wave, thermal relaxation of condensed particles and velocity relaxation. Thus, the jet is just as an ordinary stream. Equations with boundary layer conditions are used; including mean shear layer equations using velocity, temperature and composition as variables. In China, a few organizations have started some experimental work. There is very little theoretical analysis done. Work done abroad only began in recent years[1-3].

Manuscript received on July 16, 1984.

Generalized separated flow in the base should also include /55 the study of the complicated wake formed due to the detachment of the vortex. The flow around a dull body has a wide range of applications. There are topics in this area in aeronautics, aerospace, ocean engineering and wind load of tall buildings. There is no profound understanding on the mechanism of vortex detachment behind a dull body. Nevertheless, experimental work is way ahead of theoretical analysis. Back in the sixteenth century,, before fluid dynamics was established as a discipline, the famous Italian painter and scientist, Leonardo da Vinci (1452-1519) drew pictures showing the re-circulation and vortex of flows toward a plate, around a column and around a triangular beam[4],[5]. It can be considered as the earlier record noting the observation and study of vortex detachment. Earlier in this century, Planck took some photographs of the wake vortex motion around a circular beam [6]. These are qualitative descriptions based on flow field visualization. There was very little theoretical analysis in earlier days. As testing techniques were developed and computers became available, together with a strong background in applications, a great deal of progress was made in areas involving the vortex formation mechanism behind the dull body and the interaction of vortices [7]-[9]. Let us use the flow around a circular column as an example, it is the most widely studied topic in fluid dynamics experimentally, theoretically and in computation. The geometry of a two-dimensional circular column is very simple. However, even in a steady flow, the near wake flow field varies in a complex manner

in various Reynolds number ranges. The mechanisms for vortex detachment, vortex interaction and vortex streak formation are not yet known. Figure 3 shows the experimental results obtained over the years[10]. It represents the stationary point pressure coefficient C_{pb} vs. Re.

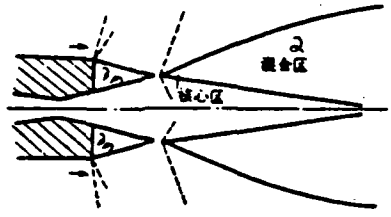

Figure 2. Schematic Diagram of Engine Jet

1. core area
2. mixing area

A-B (Re=1-50): The entire flow field is a steady laminar flow.

B-C: If Re>50 and the flow remains to be steady and laminar, based on theoretical analysis, C_{pb} varies along the curve B-C.

B-D (Re=50-200): the actual situation does not follow B-C. Although the flow field still remains laminar, the wake begins to oscillate periodically.

D-E (Re=200-1500): Turbulence begins to appear and periodic oscillation moves downstream.

E-F (Re=1500-2×10^5): The turning point moves forward along the free shear layer. The turning process develops into turbulent flow from periodic oscillation.

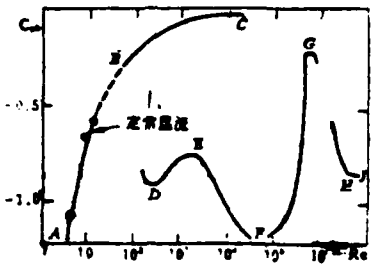

Figure 3. Pressure Coefficient at Stationary Point Behind Circular Column

1. steady laminar flow

F-G ($Re=5x10^5\pm$): In this region, the drag index falls drastically due to rising base pressure. The turning point is very close to the separation point. The flow always starts with laminar separation. After forming a bubble zone on the surface due to attachment, it becomes turbulent separation.

The pressure coefficient plot is somewhat typical. However, it is significantly affected by the turbulence of the main flow, the roughness of the surface and other factors. It is not possible to discuss this problem in depth here. Similar topics were also discussed in the "Meeting on Separation Flow and Vortex Motion" and reference [9] was introduced. In this paper, we will briefly introduce the experimental research and theoretical analysis on the base flow of flight vehicles in Section II. In Section III, we will concentrate on solving N-S equations with /56 numerical methods.

II. Brief Introduction to Experimental Research and Analytical Methods on Base Flow

Most base pressure experiments are done at low Mach numbers ($M \leq 5$). There are few high Mach number experiments and even fewer of them are done in turbulent flow. Because it is difficult for ground simulation equipment to simultaneously satisfy the high Mach number and high Reynolds number requirement, a great deal of progress has been made continuously in the are of testing techniques. The experimental range can be extended to around $M=30$ and $Re=10^7 \sim 10^8$.

For slender cones, there are several parameters affecting the base pressure; including laminar or turbulent flow, Mach number and Re number of the incoming flow, geometric parameters of the cone (semi-conical angle θ_c and dullness R_N/R_b where R_N is the radius of the head and R_b is the radius of the base), specific wall temperature and the magnitude of the attack angle.

(1) Effect of Re: The state of the flow (laminar or turbulent) is an important factor determining the base pressure. In the case of laminar flow, the base pressure drops with increasing Re. In the case of turbulent flow, it is independent of Re. Nevertheless, some individual experiments found that base pressure was affected by Re.

(2) Effect of M: The experiment done by Zarin[11] showed that when $M \leq 4.5$, base pressure decreased as M increased. However, when $M \geq 4.5$, base pressure rose with increasing M. This shows that base pressure varies according to different patterns

at hypersonic and supersonic speeds.

(3) Effect of apex angle and dullness: As the dullness increases, the specific base pressure p_b/p_∞ increases. When M and dullness remain unchanged, base pressure increases with increasing apex angle.

The major variables affecting base pressure are introduced above. Their individual effect seems to follow a specific pattern. However, it is very hard to analyze the combined effects of these parameters. Some patterns may be obtained if shoulder parameters such as M_δ and Re_δ are used to treat the experimental data on base pressure because external should flow near the base and should directly affect base pressure. A detailed summary was made on this subject in reference [12].

Theoretical analysis on base flow is still based on the model proposed by Chapman et al. The Chapman-Karst method is semi-empirical which agrees with experimental results at low speeds. It is widely used. However, its disadvantages are obvious at high speeds. The boundary layer integral method developed later by Lees and Reeves[13],[14] is more successful. It does not rely on empirical constants. This method is also different from the conventional integration method. Due to the fact that the interaction between a viscous layer (free shear layer) and the external inviscid flow must be taken into consideration in studying base flow and a new unknown variable must be introduced as a section parameter in choosing the velocity section, it is necessary to add more equations. As a result, we have the integral equations of continuity, momentum

and moment. The three unknowns are the external Mach number M_e, momentum loss thickness θ and section parameter α. The equations are:

$$\frac{dM_e}{dx}=\frac{N_1}{D},\ \frac{d\theta}{dx}=\frac{N_2}{D},\ \frac{d\alpha}{dx}=\frac{N_3}{D} \qquad \text{(A)}$$

where D, N_1, N_2, and N_3 are functions of M_e, θ, α and x. This set of differential equations does not seem unusual. However, when we integrate over the direction of flow from an initial cross-section, it is not possible to consider the effect of downstream motion on that upstream. In reality, at D=0, the integration cannot proceed. It is necessary to repeatedly modify the initial value by iteration to continue. At D=0, it is the neck of the wake, which is a critical point. The critical point theory has been used to solve base flow for years. However, this /57 method is limited to a dull body with relatively low M at the shoulder [12].

The work done by Zhar Wenlong et al [15],[16] is included in engineering calculation of turbulent flow. The base heat flow analysis might be on the rough side. To treat this problem better, it is necessary to determine the mean heat flow with the aid of energy conservation after the relations among parameters in the re-circulation zone are understood. Meng's straight line method [17] was also used to calculate the base heating problem.

III. Numerical Method

Many authors[18]-[22] used numerical integration of the N-S equations to study base flow or other separation flows. Numerical methods can approximately be classified into three major types: 1. finite difference, 2. finite element and 3. integration relation or straight line method[17]. We believe that although C. Taylor et al recently used finite element method to calculate an incompressible flow field, the majority of numerical computations of base flow was done by using a finite difference method[23],[24]. In the following, we will discuss incompressible and compressible flows.

(A) Solving N-S equation for Incompressible Flow

The N-S equations expressed in original variables ($\vec{v}$, p) can be written as:

$$\frac{\partial \vec{v}}{\partial t} + \vec{v} \cdot \nabla \vec{v} = -\frac{1}{\rho} \text{grad } p + \nu \nabla^2 \vec{v} \tag{1a}$$

$$\text{div } \vec{v} = 0 \tag{1b}$$

Because it is not a single initial value problem and the time term $\partial p/\partial t$ is not included in (1b), the computation is somewhat difficult. In this case, the continuity equation and equation of motion are not simultaneous equations with respect to variables $\vec{v}$ and p. The continuity equation imposes constraints to the variable $\vec{v}$. It is a problem to be addressed. Earlier, the constraint div $\vec{v}$=0 was relaxed. In addition, D=div $\vec{v}$. The equation of motion becomes:

$$\frac{\partial D}{\partial t} = -\underbrace{\mathrm{div}\cdot(\vec{v}\cdot\nabla\vec{v})}_{0} - \nabla^2\frac{p}{\rho} + \nu\nabla^2 D \tag{2}$$

The difference equations of (1a) and 2) are

$$\vec{v}^{\,n+1}_{i,j} = v^{n}_{i,j} + \Delta t\mathcal{L}(\vec{v}, p) \tag{3}$$

$$D^{n+1}_{i,j} = D^{n}_{i,j} + \Delta t[-Q^{n}_{i,j} - (\delta_{xx}+\delta_{yy})(p/\rho)^{n}_{i,j} + \nu(\delta_{xx}+\delta_{yy})D^{n}_{i,j}] \tag{4}$$

where L is the difference operator for all terms except for the time and dependent terms in (1a). δ_{xx} and δ_{yy} are the second order difference operator. Now, $D^{n+1}_{i,j} = 0$ is used to meet the constraint condition. Equation (4) becomes the equation for p/ρ in the n^{th} layer, i.e.

$$(\delta_{xx}+\delta_{yy})(p/\rho)^{n}_{i,j} = \frac{D^{n}_{i,j}}{\Delta t} - Q^{n}_{i,j} + \nu(\delta_{xx}+\delta_{yy})D^{n}_{i,j} = -R^{n}_{i,j} \tag{5}$$

The computation procedure is as follows. Based on the known $Q^{n}_{i,j}$ and $D^{n}_{i,j}$, $R^{n}_{i,j}$ is determined by equation (5). Then, $(p/\rho)^{n}_{i,j}$ is determined. $\vec{v}^{\,n+1}_{i,j}$ is then calculated by substituting the results into equation (3). At this time, div $\vec{v}^{\,n+1} \neq 0$. The final result is obtained by repeated iterations. The equation of continuity is met by repeated iterations. Later, an artificial compression method was developed[25]. A time term is introduced into the continuity equation:

$$\frac{\partial p}{\partial t} = c^2\,\mathrm{div}\,\vec{v} = 0 \tag{6}$$

The above equation, although there is no physical meaning, is consistent with the equation of continuity for a compressible flow of c interpreted as the sound propagating speed. The value of c must be chosen to ensure that the solution is convergent to become a steady solution. Recently, another method was used in reference [26]. $\vec{v}$ and $\vec{w}$ were used as two variables. The two equations are: /58

$$\frac{\partial \vec{\omega}}{\partial t} + \vec{v} \cdot \nabla \vec{\omega} = \frac{1}{Re} \nabla' \vec{\omega}$$
$$\nabla' \vec{q} = -\nabla \times \vec{\omega} \qquad \text{(A)}$$

In order to make $\vec{v}$ and $\vec{w}$ satisfy the condition that their divergence is zero, a "potential correction" is added to each time layer.

(B) Numerical Solution of *N-S Equations for* Compressible Flow

As early as 1965, Brailovskaya[18] presented a two step explicit difference scheme with second order accuracy based on unsteady N-S equations. Allen and Cheng Singyi[19] improved it. Viscous terms were treated by using the method similar to the Dufort-Fronkel treatment to eliminate the time limitation due to stability requirement. Later, Brailovskaya[27] took the treatment in reference [19] into consideration and introduced an "artificial viscosity term" with second order accuracy in the equation of continuity. It has a "numerical smoothing" effect on the region where the flow field gradient varies greatly. In the smooth region, this term is near zero.

During the process of computing a steady problem based on

unsteady equations, the results obtained at any instance do not reflect the actual physical process. Only when $t \to \infty$, it approaches the steady solution. The advantage is that the amount of computer time required to obtain a convergent solution can be reduced. Dorodnitsyn[28] used an "artificial unsteady" method to improve the computing process. In view of the concept in reference [28], reference [29] introduced an adjusting factor in solving the N-S equations for a two-dimensional base flow. The results showed that the rate of convergence was improved.

The MacCormack scheme is famous due to the fact that it successfully calculated an inviscid shock wave containing flow and the interference between the shock wave and the boundary layer. In 1969, MacCormack's scheme[30] was an explicit two step format. The step length is seriously limited by the stability condition. Later, he introduced a mixed algorithm[31] which included the MacCormack explicit scheme and the corrected time splitting plan. The effectiveness of the computation was apparently improved. The expanded MacCormack scheme allows the use of any mesh to approximate any series of equations in a physical plane.

The following discussion is focused on the plan proposed by MacCormack in 1981[32]. This is a conditionless two step process starting from the conservative N-S equations:

$$\frac{\partial \vec{U}}{\partial t} + \frac{\partial \vec{F}}{\partial x} + \frac{\partial \vec{G}}{\partial y} = \frac{\partial \vec{F}_v}{\partial x} + \frac{\partial \vec{G}_v}{\partial y} \tag{7}$$

difference is taken in two steps:

$$\begin{cases} \Delta U^{n}_{i,j} = -\Delta t\left(\dfrac{\Delta_{+}F^{n}_{i,j}}{\Delta x} + \dfrac{\Delta_{+}G^{n}_{i,j}}{\Delta y}\right) - \Delta t\left(\dfrac{\Delta F^{n}_{v}}{\Delta x} + \dfrac{\Delta G^{n}_{v}}{\Delta y}\right)_{i,j} \\ \left(I - \Delta t\ \dfrac{\Delta_{+}|A|}{\Delta x}\right)\left(I - \Delta t\ \dfrac{\Delta_{+}|B|}{\Delta y}\right)\delta U^{\overline{n}}_{i,j} = \Delta U^{n}_{i,j} \\ U^{\overline{n+1}}_{i,j} = U^{n}_{i,j} + \delta U^{\overline{n}}_{i,j} \end{cases} \tag{8a}$$

/59

$$\begin{cases} \Delta U^{\overline{n}}_{i,j} = -\Delta t\left(\dfrac{\Delta_{-}F^{\overline{n}}_{i,j}}{\Delta x} + \dfrac{\Delta_{-}G^{\overline{n}}_{i,j}}{\Delta y}\right) + \Delta t\left(\dfrac{\Delta F^{\overline{n+1}}_{v}}{\Delta x} + \dfrac{\Delta G^{\overline{n+1}}_{v}}{\Delta y}\right)_{i,j} \\ \left(I - \Delta t\dfrac{\Delta_{-}|A|}{\Delta x}\right)\left(I - \Delta t\dfrac{\Delta_{-}|B|}{\Delta y}\right)\delta U^{\overline{n}}_{i,j} = \Delta U^{\overline{n}}_{i,j} \\ U^{\overline{n+1}}_{i,j} = \dfrac{1}{2}(U^{n}_{i,j} + U^{\overline{n}}_{i,j} + \delta U^{\overline{n}}_{i,j}) \end{cases} \tag{8b}$$

where $|A|$ and $|B|$ are matrices with positive eigenvalues $\lambda_{|A|}$ and $\lambda_{|B|}$. They are related to Jacobi matrix. $A=\partial F/\partial U$ and $B=\partial G/\partial U$. In addition, $\lambda_{|A|}$ and $\lambda_{|B|}$ include viscosity effect. The first terms in (8a) and (8b) are in the explicit MacCormack format. The second term is totally implicit. The coefficient matrix, however, is doubly diagonal. In order to facilitate direct computation, the conventional three diagonal chasing method for the implicit scheme is avoided to save the computational load in every step. In summary, the time step is greatly widened by (8a) and (8b). The Courant number could reach 10^2-10^3. However, we must point out two things: when Δt is chosen to satisfy the CFL

condition, the scheme will automatically be transformed to the explicit algorithm. Second, it is very important to add an approximate dissipating term in the process. When it is used to calculate flow in the base, special precautions must be taken in treating the boundary condition.

One of the major difficulties encountered in the implicit method is how to treat the non-linear convection term. The Beam-Warming implicit factor decomposition method[34] as expanded by Steger[33], where the non-linear convection term of the $(n+1)^{th}$ layer is calculated based on the linear function established by the Taylor series expansion of the $(n+1)^{th}$ layer and the n^{th} layer, can be used to calculate the viscous flow field in any shape. Reference [35] showed that this method is capable of accelerating the stabilizing process in calculating the base flow as compared to an explicit method. A great deal of computer time can be saved.

Steger pointed out that the non-linear term in the conservative Euler equations is a homogeneous function of U. This property actually allows the splitting of flow vectors $\vec{F}$ and $\vec{G}$ into subvectors by similarity transformation. The corresponding off-center difference direction is related to the eigenvalues of $\partial\vec{F}/\partial\vec{U}$ and $\partial\vec{G}/\partial\vec{U}$. The difference between this new algorithm and the Beam-Warming scheme is that the coefficient matrix of the linear equations thus derived is an upper (lower) triangle. Its inverse can be directly found. This means that the flow field has a subsonic region. It also provides reasonable results. In reference [36], this idea was used to

solve the inviscid portion of the N-S equations. The viscous part was computed using a method similar to that developed by Saul'yev[37]. The computation is as follows:

$$\begin{cases} \left[I+\frac{\theta\Delta t}{(1+\xi)}\nabla_{\xi}(A^{-}+A^{*})\right]\left[I+\frac{\theta\Delta t}{(1+\xi)}\Delta_{\xi}(B^{-})\right]\Delta\vec{U}^{*} \\ \qquad =-\frac{\Delta t}{1+\xi}(\delta_{\xi}^{+}F^{-}+\delta_{\xi}^{+}F^{+}+\delta_{\eta}^{-}G^{-}+\delta_{\eta}^{+}G^{+})^{n}+RHS \\ \left[I+\frac{\theta\Delta t}{(1+\xi)}\nabla_{\eta}(B^{-}+B^{*})\right]\left[I+\frac{\theta\Delta t}{(1+\xi)}\Delta_{\eta}(A^{-})\right]\Delta\vec{U}^{n+1}=\Delta\vec{U}^{*} \\ \vec{U}_{i,j}^{n+1}=\vec{U}_{i,j}^{n}+\delta\vec{U}_{i,j}^{n+1} \end{cases} \tag{9a}$$

$$\begin{cases} \left[I+\frac{\theta\Delta t}{(1+\xi)}\Delta_{\xi}(A^{-}+\hat{A}^{*})\right]\left[I+\frac{\theta\Delta t}{(1+\xi)}\Delta_{\eta}(B^{*})\right]\Delta\vec{U}^{**} \\ \qquad =-\frac{\Delta t}{(1+\xi)}(\delta_{\xi}^{+}F^{-}+\delta_{\xi}^{+}F^{+}+\delta_{\eta}^{-}G^{-}+\delta_{\eta}^{+}G^{+})^{n+1}+RHS \\ \left[I+\frac{\theta\Delta t}{(1+\xi)}\Delta_{\eta}(B^{-}+\hat{B}^{*})\right]\left[I+\frac{\theta\Delta t}{(1+\xi)}\Delta_{\eta}(A^{-})\right]\Delta\vec{U}^{n+1}=\Delta\vec{U}^{**} \\ \vec{U}_{i,j}^{n+1}=(\vec{U}_{i,j}^{n}+\vec{U}_{i,j}^{n+1}+\Delta\vec{U}_{i,j}^{n+1}) \end{cases} \tag{9b}$$

where A^{+} and A^{-} are the matrices formed by the positive and negative eigenvalues of $A=\partial\vec{F}/\partial\vec{U}$, respectively. B^{+} and B^{-} are the matrices formed by the positive and negative eigenvalues of $B=\partial\vec{G}/\partial\vec{U}$, respectively. A^{*} and B^{*} are matrices reflecting the effect of viscous terms. The asymptotic off-center difference of the convection term is related to the signs of the eigenvalues of A and B. This technique can improve the resolution of low viscosity areas. /60

Because the time step is vigorously limited by stability in an explicit method, even when various steps are chosen in different directions to calculate a high Re number flow, the cost is very high. It should be pointed out that there is nothing new in solving N-S equations with an implicit or hybrid method. However, it is rarely used to solve the flow in the base.

The hybrid scheme is to split the equations into several terms. Each term is approximated by an explicit or implicit difference operator. With respect to the step corresponding to each operator, the maximum time step Δt_M is allowed to be used. If the splitting is to categorize difference operators into two kinds: in Class A Δt_M is equivalent to Δt_a and in Class B Δt_M is equivalent to Δt_b, and $\Delta t_a << \Delta t_b$. In this case, the most meaningful thing to do is to treat Class A operators as implicit operators. Due to the fact that the explicit format which is rigorously limited by the stability condition, is replaced by the implicit approximation, plus the appropriate explicit approximation remains, it is much simpler than the full implicit scheme. It is particularly favorable for solving thin viscous layer problems. This method can be further simplified because the simpler the operator becomes, the easier the implicit treatment is. In reference [31], transversal derivatives were split into viscous-parabolic and inviscid-hypobolic parts. This treatment improves the effectiveness of the the computation.

In conclusion, numerical methods to solve N-S equations are under development. Their effectiveness and optimization process are improving. For example, Beam-Warming combined the stable

linear multi-step method with an approximate factor decomposition method to create the optimized ADI method. This type of technique is growing. The goal is to accelerate the rate of convergence, improve accuracy and strengthen effectiveness.

IV. Opinions on Developmental Trend of Numerical Methods for Separated Base Flow

(1) Implicit methods, such as those presented by Beam-Warming, Briley-McDonald[38] and MacCormack, are unconditionally stable when solving a pure initial value problem. However, it very difficult to calculate the stability with boundary conditions. Recently, Beam-Warming[39] cited an example to explain a more generalized stability analysis, including the effect of boundary conditions. Thus, some ambiguities are explained. The theoretical basis for this type of stability analysis is the theory of Kreiss-Osher-Gustaffson. The results show that unconditional stability algorithm agrees with the implicit boundary condition.

(2) In order to meet the requirements for a complicated flow such as a non-symmetric profile, especially in improving the resolution of the flow field near the base, it is necessary to rationally arrange the nodes. It is better to employ a body coordinate system or a multi-layer treatment[40]-[43].

(3) It is very cumbersome to calculate the shock wave and secondary shock wave for a complicated supersonic flow. It is very difficult to determine the shock wave position using the

capture method. The best approach is to combine these two methods. The shock wave allocation method should be used for strong shock waves or primary shock waves of influence. The relatively weaker secondary shock waves should be treated with the wave capture method.

(4) We should pay attention to combining numerical methods with theoretical analyses. For instance, the expansion mechanism of the shoulder should be properly employed in the base flow calculation. Three-dimensional automatic adjustment of nodes can be used in calculating the separated flow at high Re numbers. In a turbulent flow, theoretical analysis and experimental data can be used to determine the step length of nodal points. In /61
summary, it is very meaningful to apply the results obtained from theoretical analysis to improving the effectiveness of numerical methods.

References

[1] Mace, A.C.H. et al., J. Spacecraft & Rocket, 19, 6, 557-563 (1982).

[2] Jenson, D.E. & Wilson, A.S., Combustion & Flame, 25.1, 43-55 (1975).

[3] Jenson, D.E. & Spalding, D.B., Combustion & Flame, 39.3, 309-326 (1979).

[4] Popham, A.E., the Drawings of Leonardo da Vinci (1946).

[5] Kemp, M. Leonard, da Vinci, the Marvellow Works of Nature and Man (1981).

[6] Prandtl, L. & Tietjens, O., Appl. Hydro- and Aerodynamics (1934).

[7] Saffman, P.G. & Baker, G.R., Ann. Rev. Fl. Mech. Vol. 11 (1979).

[8] Sarpkaya, T. & Issasson, M., Mechanics of waves forces on offshore structure (1981).

[9] "Symposium of the 1984 Meeting on Separated Flow and Vortex Motion".

[10] Roshko, A. & Fiszdon, W., Problems of Hydrodynamics & Continum Mechanics. 606-619 (1969).

[11] Zarin, N.A., AIAA J. 4.4 (1966).

[12] Bian Yinqui et al, "References in Aerodynamics" No. 2 & 3 (1977).

[13] Lees, L. & Reeves, B.L., AIAA J., 2.11 (1964).

[14] Reeves, B.L. & Lees, L., AIAA J, 3.11 (1965).

[15] Chow, W.L. et al., AIAA J., 15.9 (1977).

[16] Lin, S.K. & Chow, W.L. AIAA J., 17.4 (1979).

[17] Meng, S.C.S., J. Comp. Phys., 15.3 (1974).

[18] Brailovskaya, I.Y. Soviet Physics-Daklady, 10.2 (1965).

[19] Allen, J.S. & Cheng, S.I. Phys. of Fluids, 13.1 (1970).

[20] Roache, P.J. et al., AIAA J., 8.3 530-538 (1970).

[21] Rose, W.C., AIAA Paper, 76-96 (1976).

[22] Zhang Hanxing et al, Journal of Mechanics, 4 (1981).

[23] Zhuang Feuggan et al, Progress in Mschanics, 1 (1983).

[24] Bian Yinqui, Progress in Mechanics, 1 (1983).

[25] Peyret & Taylor, Computational methods for fluid flow (1982).

[26] Ma Yenwen, Symposium of the Second National Computational Fluid Dynamics Meeting (1984).

[27] Brailovskaya, I.Y. et al., Intern Chemical Eng. 10.2, 228-232 (1970).

[28] Dorodnitsyn, A.A., Lecture Notes in Phys. Vol. 18 (1972).

[29] Ma Yenwen,Computational Mathematics and Applied Mathematics No. 3 (1978).

[30] MacCormack, R.W. AIAA Paper 69-354 (1969).

[31] MacCormack, R.W. NASA TMX-73129, (1976).

[32] MacCormack, R.W. AIAA Paper 81-110 (1981).

[33] Pullian T.H. & Steger, J.L., AIAA Paper 78-10 (1978).

[34] Beam, R.M. & Warming, R.F., AIAA J. 16.4 (1978).

[35] Dong Changquan, Journal of Aerodynamics, 4 (1982).

[36] Dong Changquan, Journal of Aerodynamics, 4 (1984).

[37] Richtmyer, R.D. & Morton, K.W., Difference Methods for Initial Problems (1967).

[38] Briley, W.R. & McDonald, H., J. Comp. Phys. 34.1 (1980).

[39] Warming, R.F. & Beam, R.M., Computational Fluid Dynamics SIAM-AMS Proc. Vol. 11 (1978).

[40] Lourbord, K., AIAA Paper 80-65 & 81-282.

[41] Mikhael, A.G., AIAA J. 18.8 (1980).

[42] Thompson, J.F., J. Comp. Phys., 47.1 (1982).

[43] Guo Yufa, Symposium of Second National Meeting on Numerical Methods in Fluid Dynamics, 1982.

Advances in Inverse Boundary Layer Techniques /63

Li Suxun

(Beijing Institute of Aerodynamics)

At the present moment, the complete time-dependent N-S equations are not widely in a wide variety of engineering applications. This is not just due to the lack of understanding of turbulent flow, lack of suitable turbulent models, or limitations imposed by economic conditions and computing capacity and speed. Instead, the physical phenomenon to be reflected in reality does not require such completeness, complexity and delicate detail. The results obtained by simplified N-S equations can already meet the requirements. Based on the physical problems, it is possible to simplify the equations, boundary conditions and initial conditions. Consequently, various simplified equations, such as the steady NS equation, low dimension number NS equation, Euler equation obtained by omitted viscous terms, potential equation, linearized equation, parabolic NS equations obtained by neglecting some viscous terms or a portion of the equations, and boundary layer equation, can be obtained. A variety of numerical methods were developed for these equations to form a new branch in computational fluid dynamics.

One of the most frequently encountered typical situation is a high Reynolds number flow field. In this case, the viscosity effect of the fluid is only apparent in a thin layer near the

surface. The scale of this thin layer is much smaller than the characteristic scale of the flow around it. Based on this physical fact, Prandtl presented the boundary layer concept. Momentum changes normal to the surface are not considered. Higher order viscous terms in the NS equations are completely omitted. Consequently, we get the boundary layer equation. The boundary layer equation is not only totally different from the NS equations in complexity, its mathematical nature is also altered. It has the characteristics of a parabolic partial differential equation. When the flow is attached, the results obtained based on boundary layer equations agree well with the data provided by the complete NS equations. In addition, they are consistent with experimental results. In use, the requirements for computer speed and capacity in solving boundary layer equations are less than those involved in solving complete NS equations. However, when flow separation occurs, singularity appears at the separation point when boundary layer equations are used. Goldstein[1] did a rigorous study on the properties of two dimensional, incompressible boundary layer equations at the point of separation. He pointed out that boundary layer equations are only applicable downstream and upstream from the separation point. At the separation point, the equations begin to exhibit singularity. Furthermore, the specific form of the square root singularity was derived. Since then, Stewartson (1958[2], 1969[3], 1970[4]), Kaplun (1967[5]), Messiter (1975[6]), Cousteix and Houdeville (1981[7]) also did further work. Dean (1950[8]) proved that there is not singularity near the separation point

for complete NS equations. The solution is still an analytical one. Therefore, the singularity is introduced by simplifying the NS equations.

The advantages of boundary layer equations are well recognized in practice. Is it possible to use them in some separated flow field? Because flow separation is frequently encountered, it is desirable to search for a new technique which not only preserves the advantages of boundary layer equations but also avoids the difficulties associated with separation point singularity. The inverse boundary layer technique is a new method developed with these ideas in mind.

Manuscript received on June 22, 1984. Revised received on September 27.

When the boundary layer concept is applied, the flow field /64 is divided into an inviscid flow region and boundary layer region. If we base the velocity distribution (or pressure distribution) at the outer fringe of the given boundary layer and non-flow conditions at the surface of an inviscid flow to solve the velocity distribution inside the layer and consequently derive other parameters (such as surface shear stress, displacement thickness, momentum thickness, etc.), then the method is usually called a forward method. As described before, at the point of separation, the equation is singular. Thus, the feasibility of progressing downstream is limited. Let us think if the boundary conditions are changed so that the shear stress

distribution (or boundary layer displacement thickness distribution) on the surface is given. Furthermore, its transition near the separation point is smooth so that the outer edge boundary layer velocity also becomes an unknown. It is then possible for boundary layer equations to exhibit no singularity at the point of separation. This is called the inverse method. It not only preserves the special features of boundary layer equation but also can be used to describe the characteristics of a flow field with a small separation zone. Therefore, it has received a lot of attention. Similar to the forward method, the inverse method is making progress in two directions: differentiation and integration.

A review of the history of the inverse method can predict future development trends. In 1966, Catherall and Mangler[9] first introduced this concept. Moreover, they employed the inverse boundary layer integral equation technique to successfully pass through the point of separation. In 1968, Reyhner and Flugge-Lotz[10] published their results of the study on the interference between a shock wave and the boundary layer in a compressible laminar flow. Differential equations were solved with the inverse method. They proposed the FLARE assumption to resolve the instability problem in numerical computation caused by the reverse flow in the separation zone. It should be pointed out that the numerical results on laminar flow separation bubbles in a paper published by Briley[11] in 1971 by using steady two-dimensional incompressible NS equations quantitatively described the flow field in the re-circulation

zone. The inverse in boundary layer thickness after separation not only serves as the basis for comparison for the inverse technique but also illustrates physically that the boundary layer concept is still applicable. Keller and Cebeci[12] in 1972 compared their work with Briley's results. They specified the shear stress distribution on the surface, began with boundary layer differential equations, and used the FLARE assumption to obtain successful results. In addition, Horton (1974[13]), Klineberg and Steger (1974[14]) gave examples to calculate two-dimensional laminar incompressible separated flow fields. Different difference schemes were given for attached flow, separated flow and mixed region. Carter (1974[15]), and Wornom (1975[16]) also presented corresponding difference schemes and obtained results for laminated flow with separation and re-attachment. Carter published computational results on the interference between a viscous flow and an inviscid flow in 1975[17]. By 1978, a unified Crank-Nicolson difference scheme[18] suitable for both forward and inverse methods was introduced. It is applicable to two-dimensional incompressible flows and compressible laminar and turbulent flows. Furthermore, in 1979-1981 this method was used in a transonic flow field with an interference zone between the shock wave and the boundary layer. A satisfactory iteration method was resulted[19,20]. Kuhn and Nielson (1973[21]) calculated the flow field in the rear part of an axisymmetric body with jet exhaust. Kawai (1977[22]) presented examples of calculating the compression angle in a compressible laminar flow. Williams (1975[23]), Whitfield and

Swafford (1975[24]) also obtained successful results. Cebeci (1975[25], 1976[26], 1979[27]) transformed the boundary layer equations into various forms. In addition, the accuracy was improved by iterations along the direction of flow. Satisfactory results were obtained in a variety of small separation regions. He not only introduced an algebraic turbulent model but also used the complicated two-dimensional turbulent model in the computation. It was successfully used in internal flow and trailing flow calculations. Until 1983, Agarwal et al[28] still based on a two-equation turbulent model to solve the two-dimensional and axisymmetric separation flow in a transonic flow by the inverse technique.

On the other hand, many worthwhile results were obtained by using this inverse technique to integrate boundary layer equations. Klemp and Acrivos (1972[29]), East, Smith and Merryman (1977[30]) calculated flow fields with smalI separation zones based on Green's roll-in method. Whitfield (1978[31]) improved the velocity model in the separation zone and obtained results on compressible turbulent layer integral equations by using the inverse approach. Swafford (1979[32]) introduced the analytical expression for the velocity model inside a two- /65
dimensional turbulent separation zone. Kline (1981[33]) used Cole's wall-wake law, their separation criteria, and experimental data to obtain various results. Based on various methods published, we can see that it is easier to be successful in calculating a viscous or inviscid flow by using the inverse method for integral boundary layer equations.

In practice, the iterative solution of the interference between a viscous flow and an inviscid flow receives a lot of attention. Amarante and Chang (1979[34]) conducted a calculation on the interference near the separation bubble of a laminar flow. Kwon and Pletcher (1979[35]), Veldman (1979[36], 1981[37]) showed the coupled solution for an incompressible laminar flow with strong interference. In recent years, when there is shock wave - boundary layer interference in a transonic flow field, the iterative solution of viscous and inviscid flows has been developed rapidly. The interference at the jet exhaust calculated by Kuhn (1979[38], 1980[39]), the steady transonic flow field around the wing estimated by Collyer (1979[40]) and the iterative calculation of three-dimensional time-dependent Euler equations and turbulent boundary layer equations by Whitfield (1980[24]) belong to the category of iteration based on the inverse method of integral boundary layer equations. Similar to earlier methods, it is required to provide a semi-empirical formula for frictional drag and momentum thickness (or shape factor). Carter[19,20], based on differential equations, used the inverse method for finite difference boundary layer equations coupled with iterations involving the complete potential flow equations to obtain results on the separated region. The method is simple. It converges rapidly and is applicable to flow fields with strong interference regions. In the iterative process involving a viscous and an inviscid flow, there are two commonly used methods. 1) The boundary velocity of the inviscid flow is allowed to be perturbed. 2) The boundary layer position

thickness (or its equivalent) is allowed to be perturbed. There are successful attempts either way.

Our understanding on three-dimensional separated flow is getting deeper. Flow visualization, topological analysis and various numerical computations directly promoted the investigations on the three-dimensional inverse technique. Work by Le Balleur (1981[41]), Stock (1980[42]), Formery (1982[43]), Blaise (1982[44]), Delery and Formery (1983[45]) reveals some early information in this aspect.

In recent years, work in this area began in China[46, 47, 48, 49]. It is still limited to some new studies on two-dimensional laminar and turbulent flow.

A review of this development process makes us feel that the mechanisms for some complicated flow motions in high Reynolds number flow fields are not yet well understood; including three-dimensional separation, influction separation, relation between separation and vortex formation, and turbulence models in and out of separation regions. For this reason, more assumptions are used in establishing a mathematical model. Despite the use of various equations and numerical computation, it is often difficult to obtain satisfactory results. Therefore, in exploring the flow mechanism, we must be able to identify various major influencing factors. We must offer some methods to verify theoretical models. In addition, some meaningful results can be obtained. It is required that these methods are not too complicated for engineering applications. Based on the fact that the inverse method discussed above is one of those methods, its

future is very bright throughout the world.

References

[1] Goldstein, S., Quart. J. Mech. Appl. Math., Vol. 1, Part 1, pp. 34-69 (1948).

[2] Stewartson, K., Quart, J. Mech. Appl. Math., Vol. II, pp. 399-410 (1958).

[3] Brown, S.N. and Stewartson, K., Ann. Rev. F. Mech., Vol. 1, pp. 45-72 (1969).

[4] Stewartson. K., J. Fluid Mech., Vol. 44, Part 2, pp.347-364 (1970).

[5] Kaplun, S., Fluid Mechanics and Singular Perturbations Edited by P.A. Lagerstron, L.N. Howard and C.S. Liu, Academic Press, New York.

[6] Messiter, A.F., AGARD CP-168 (1975).

[7] Cousieux, J. and Haudeville, R., AIAA J. Vol. 19, No. 8, pp. 176-185 (1981). /66

[8] Dean, W.R., Proc. Comb. Phil. Soc., Vol. 46, pp. 293-306 (1950).

[9] Catherall, D. and Mangler, K.W., J. Fluid Mech. Vol. 26, No. 1, pp. 163-182 (1966).

[10] Reyhner, T.A. and Flugge-Lotz, I., Int. J. Non-Linear Mech. Vol. 3, No. 2, pp. 173-199 (1968).

[11] Briley, W.R., J. Fluid Mech., Vol. 47, No. 4, pp. 713-736 (1971).

[12] Keller, H.B. and Cebeci, T., J. Compu. Physics, Vol. 10, pp. 151-161 (1972).

[13] Horton, H.P., AIAA J.Vol. 12, No. 12, pp. 1772-1774 (1974).

[14] Klineberg, J.M. and Steger, J.L., AIAA Paper 74-94 (1974).

[15] Carter, J.E., AIAA Paper 74-583, (1974).

[16] Carter, J.E. and Wornom, S.F., AIAA J. Vol. 13, No. 8, pp. 1101-1103 (1975).

[17] Carter, J.E. and Wornom, S.F., NASA SP-347, pp. 125-150 (1975).

[18] Carter, J.E., NASA TP-1208 (1978).

[19] Carter, J.E., AIAA Paper 79-1450 (1979).

[20] Carter, J.E., AIAA Paper 81-1241 (1981).

[21] Kuhn, G.D. and Nielsen, J.N., AIAA J. Vol. 12, No. 7, pp. 881-882 (1973).

[22] Kawai, N., 12th Int. Symp. on Space Technology and Science, Tokyo, Proc., pp. 147-152 (1977).

[23] Williams, P.G., Proc. 4th Inter. Conf. on Numerical Methods in Phy., pp. 445-451.

[24] Whitfield, D.L., Swafford, T.W. and Jacocks, J.L., AIAA Paper 80-1439 (1980).

[25] Cebeci, T., California State University at Long Beach Report TR-75-1 (1975).

[26] Cebeci, T., AD/A035693 (1976).

[27] Cebeci, T., Khalil, E.E. and Whitelaw, J.F., AIAA Paper 79-0284 (1979).

[28] Agarwal, R.K., Underwood, R.R. and Spaid, F.W., AIAA Paper 83-0453 (1983).

[29] Klemp, J.B. and Acrivos, A., J. Fluid Mech. Vol. 53, Part 1, pp. 177-191 (1972).

[30] East, L.F., Smith, P.D. and Merryman, P.J., RAE TR-77046.

[31] Whitfield, D.L., AEDC TR-78-42 (1978).

[32] Swafford, T.W., AEDC TR-79-99 (1979).

[33] Kline, S.T., Bardina, J. and Strawn, R., AIAA Paper 81-1220 (1981).

[34] Amarante, J.C.A. and Chang, I.D., AIAA Paper 79-1478(1979).

[35] Kwon, O.K. and Pletcher, R.H., J. Fluids Engineering, Vol. 101, No. 4, pp. 466-472 (1979).

[36] Veldman, A.E.P., NLP TR 79023 U (1979).

[37] Veldman, A.E.P., AIAA J. Vol. 19, No. 1, pp. 79-85 (1981).

[38] Kuhn, G.D., AIAA Paper 79-0303 (1979).

[39] Kuhn, G.D., AIAA Paper 80-0197 (1980).

[40] Collyer, M.R. and Lock, R.C., Aeronautical Quart. Vol. 30, pp. 485-505 (1979).

[41] Le Balleur, J.C., Le Recherche Aerospatiale, No. 3, pp. 161-185 (1981).

[42] Stock, H.W., AIAA Paper 80-1442 (1980).

[43] Formery, M., These de Marie Curie, Paris 6 (1982).

[44] Blaise, P., These de 3eme Cycle, Universite de Lille 1 (1982).

[45] Delery, J.M. and Formery, M.J., AIAA Paper 83-301 (1983).

[46] Li Suxun, Xu Shikun, Gu Yiqing, Study on Inverse Method for Boundary Layer Equations, Report presented in the Second National Computational Fluid Dynamics, 1984.

[47] Xu Dabong, Master's Thesis of Institute of Mechanics, Chinese Academy of Sciences.

[48] Jiang Qisheng, Master's Thesis, Beijing Institute of Aeronautics and Astronautics, 1984.

[49] Jia Ning, Master's Thesis, Nanjing Institute of Aeronautics and Astronautics, 1984.

Abstract

The inverse boundary layer techniques have been developed, which can be used to calculate the boundary layer with separation in subsonic, transonic and supersonic flow field.

A review and summary of inverse boundary layer methods are presented in this paper, including both laminar and turbulent, in 2D and 3D conditions, as well as viscous-inviscid interaction. It has been shown that the inverse techniques provided simple and efficient tools for the prediction of the boundary layer flow with separated region and will play an important role in future applications.

Study of Wing Leading Edge Vortex Breakdown /68

Lin Bingqiu

(Beijing Institute of Aerodynamics)

Abstract

This paper is divided into two parts. The first is about experimental observations of vortex breakdown in three aspects: vortex breakdown types, breakdown region structure and observation of leading edge separation vortex breakdown. All kinds of vortex breakdown phenomena of delta wing separation vortices visualized in the tube, water tunnel and low speed wind tunnel since its first discovery in 1957 are included. The difference between vortex and separated vortex breakdown structures. We point out more complicated factors affecting the breakdown of wing separated vortex. The second part is about the theoretical study of vortex breakdown. The current breakdown theories are divided into three branches; i.e., finite transition theory, hydrodynamic instability theory and vortex core theory. The development processes of these theories are summarized. Their advantages and disadvantages are compared.

Some interesting problems are presented. The results of our recent calculation on the separated vortex breakdown of a slender wing is presented.

I. Introduction

The vortex breakdown phenomenon was first found on the leeward surface of a delta wing[1]. Lambourne[2] successfully obtained two types of vortex breakdown patterns on the same photograph of the leeward surface of a delta wing. Because this phenomenon is closely correlated to the aerodynamic performance of an aircraft at large attack angles[3], it immediately attracted the attention of experimentalists and theoreticians. Investigations are centered around vortex breakdown mechanisms, forecast of conditions to cause breakdown and various types of breakdown.

Most of the experimental studies concerning breakdown mechanisms are performed in low speed circular wind tunnels. A vortex generator-fan is used to introduce the vortex into the pipe. As compared to separated vortex generated by a wing, it is even easier to control the influencing parameters with this method. Harvey[4] first used this type of apparatus to locate bubble breakdown. A series of experiments afterwards such as those reported in references [5] and [6] further proved that Reynolds number and vortex strength are the two most important initial parameters controlling the breakdown mode. Different combinations can result in six vortex disturbance modes. The impact is that two breakdown modes can be created on the wing: symmetric mode and spiral mode. They can also be created in a circular wind tunnel. This proves that the boundary condition of the separated vortex is primarily dependent on axisymmetry.

Vortex breakdown theories can be divided into three types: finite transition theory, hydrodynamic instability theory and vortex core theory. Although they are able to resolve a series of individual problems associated with vortex breakdown and in some cases arrive at the same conclusions, there is still a lot of controversy about them.

Recently, the detailed structure of the breakdown region was measured by laser technology in references [7] and [8]. For instance, reference [7] reported the bubble breakdown of a double circulation zone. If it is real, then even original axisymmetric N-S equations solved by numerical method such as the work done in references [9], [10] and [11] cannot truly reflect the breakdown mode. Defects in existing mathematical models are fully exposed.

Manuscript received on June 15, 1984, revised on September 19.

II. Experimental Observations /69

1. Vortex Breakdown Types

In Sarpkaya's experiment, besides seeing bubble breakdown and spiral breakdown, he also discovered a double spiral breakdown mode. Faler et al[7] conducted experiments over a wider range of Reynolds number. On the low Reynolds number side, they found the remaining three major disturbance modes. By gradually increasing Reynolds number or vortex strength, they sequentially divide the major disturbance modes into six types.

They are labelled as "6" (off-center shear of vortex), "5" (double spiral), "4", "3" (elliptical bubble in transverse cross-section), "2" (spiral), "1", "0" (single tail bubble, double tail bubble).

These experiments confirmed that the major disturbance mode is only related to the initial Reynolds number and vortex strength. The pressure gradient of the external flow only affects the position of the breakdown. Figure 1 shows the three breakdown boundaries obtained by Sarpkaya. In specific Re and Rc range, a dual steady state exists. It was called the lag zone by Sarpkaya. In this region, there is a tendency to spontaneous transformation from one mode to the other.

2. Detail Structure in Breakdown Region

Before laser speed measuring technique was available, the internal structure of the breakdown region could only be displayed through flow field visualization and theoretical analysis. In the past, it was believed that a bubble is a circulating region with two stationary points. However, based on the measurement made by Faler, there are two circulating regions inside a bubble type of breakdown. There are four stationary points on the center axis as shown in Figure 2. Between the first and second, as well as between the third and fourth stationary points, there are two circulation zones. The entire area is in a pulsing state. Figure 2 shows the results after taking an average. Measurements reported in reference [8] suggest that a spiral breakdown field vibrates periodically. Its

principal period is equal to the precession period of the spiral vortex.

All measurements mentioned above, indicate that every point in the breakdown region of the flow field is obviously unsteady. Furthermore, the entire breakdown position also drifts with the equilibrium position.

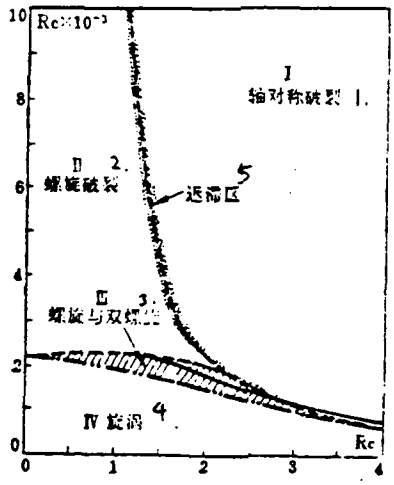

Figure 1. Boundaries of Various Vortex Breakdown Types

1. axisymmetric breakdown
2. spiral breakdown
3. spiral and double spiral
4. vortex
5. hysteresis

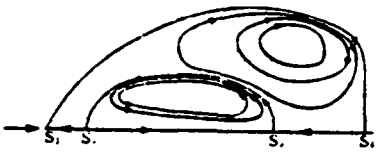

Figure 2. Double Circulation Zone in Bubble Breakdown

3. Observation of Breakdown of Leading Edge Separated Vortex

Wing separated vortex first breaks down downstream from the trailing edge[12]. As the attack angle increases, the breakdown position is gradually shifted toward above the wing. The aerodynamic performance deteriorates. Because the Reynolds number is pretty high, only bubble breakdown and spiral breakdown can be observed[2],[13]. The breakdown position is dependent on the combination of attack angle and sweepback angle. Figure 3 shows the results obtained in a water tunnel[14]. Increasing sweepback angle delays the breakdown and increasing attack angle moves the breakdown forward.

The two breakdown modes observed on separated vortex are /70 similar to those found on vortex generated in the pipe. The difference is that in the former case the bubble type does not have a secondary breakdown and the precession direction of the spiral is opposite to the spin direction while in the latter case they move in the same direction. It is worthwhile to point out that in the latter case, Reynolds number has an obvious effect on the breakdown type and position. In the former case, it is not as apparent.

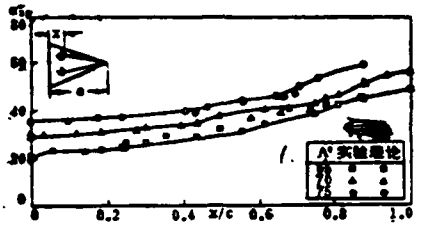

Figure 3. Effect of Attack Angle and Sweepback Angle on Delta Wing Separated Vortex Breakdown

1. experimental theory

Reference [15] employed a hot wire meter to measure the velocity distribution before and after the breakdown of wing leading edge separated vortex. The patterns obtained are very similar to those obtained in the pipe. The distribution is extremely close to axisymmetric. The phenomena leading to separated vortex breakdown is much more complex than those for a circular pipe vortex. One of the problems is vortex formation. The initial condition of a pipe vortex can be simulated by a correlation equation. However, the mechanism for the formation of separated vortex near the wing apex is still not understood. Next, a separated vortex is under the influence of a complicated external flow field. At large attack angles, it is very sensitive to the skid angle[16]. In supersonic range, separated vortex will not break. In transonic range, the initial breakdown

position begins to jump around.

III. Theoretical Studies on Vortex

To date, investigations on vortex motion and its breakdown are based on incompressible N-S equations:

$$\operatorname{div}(\rho\vec{V})=0 \tag{1}$$

$$\frac{\partial\vec{V}}{\partial t}+(\vec{V}\nabla)\vec{V}=-\frac{1}{\rho}\operatorname{grad}p+\frac{1}{\rho}\operatorname{div}\tau \tag{2}$$

Various simplified models are derived based on these equations.

1. Wave Propagation Theory. In an incompressible inviscid axisymmetric vortex motion, the finite transition theory applies. The force involved is the restoration force of a spring. Hence, a transverse wave of infinitesimal amplitude will propagate along the axis against the flow under a small perturbation.

Under the steady, incompressible, inviscid and axisymmetric assumptions, equations (1) and (2) are simplified into flow functions in cylindrical coordinate form:

$$\psi_{rr}-r^{-1}\psi_r+\psi_{zz}=r^2H'(\psi)-I'(\psi) \tag{3}$$

By letting $y=r^2/2$ and expanding for small perturbation, we get a second order differential equation for $\phi(y)$.

$$\phi_{yy}+\left(\frac{\gamma'}{2y}-\frac{U_{yy}}{U}+\frac{I_y}{2y^2U^2}\right)\phi=0 \tag{4}$$

Together with the boundary condition $\phi(0)=\phi(a)=0$, we have the Sturm-Liouville system. Based on Benjamin's definition, if all eigenvalues $\gamma^2>0$, then the flow is super critical. If an eigenvalue, such as γ_0^2 is negative, the flow is subcritical. $\gamma_0^2=0$ is the critical state.

Squire[17] first found the condition $\gamma_0^2=0$. He believed that the infinitesimal amplitude wave propagates from downstream to upstream. However, when it reaches the critical state, a stationary wave of infinite wavelength exists in the vortex, blocking the propagation of the perturbation wave. Hence, the energy accumulated causes the breakdown of the vortex.

Nevertheless, reference [18] proved that the stationary wave /71
velocity is pointing downstream. Hence, perturbation energy can only spread downstream. Equation (4) has two mutually conjugate solutions corresponding to the supercritical and subcritical states. If we define the flow force (momentum flow) as:

$$S=2\pi\int_0^R r(p+\rho u^2)\,dr$$

The supercritical flow force upstream is less than the subcritical flow force downstream. In order to balance the flow forces, breakdown must occur in between. Moreover, excess energy is consumed by the broken wake. Hence, vortex breakdown is a finite transition from a supercritical state to its conjugate subcritical state.

Bossel[19] overcame the defects in Benjamin's model. He assumed that the flow is a rigid rotation upstream. Under near critical conditions, a series solution of bubble breakdown was obtained. Liebovich et al[20] also obtained bubble breakdown

solution by employing the weak non-linear long wave theory. He pointed out that due to the finite transition of the linear theory, it was not possible to obtain critical state solution. It is a non-linear effect. In order to overcome singularity in the critical state, the flow function will undergo strange precession. A modified Korteweg-de Vries equation was obtained:

$$A_t = \epsilon(C_1 A A_x + C_2 A_{xxx}) + \delta^{\frac{1}{2}} C_1 (fA)_x + C_3 \mu A$$

It is an initial value problem. The resulting bubble solution is shown in Figure 4.

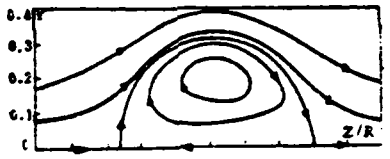

Figure 4. Single Circulation Zone in Bubble Breakdown

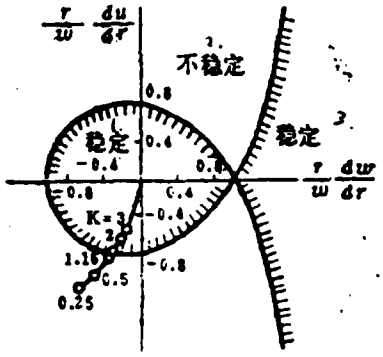

Figure 5. Vortex Stability Boundary

1. stable
2. unstable
3. stable

Certain additional conditions must be added to the two methods described above for finding the near critical state and critical state solution. They are suited for studying vortex in a circular pipe, including numerical solutions. However, they can only result in vortex bubbles with a single circulation region.

2. Hydrodynamic Instability Theory. Ludwieg[21], investigated the hydrodynamic stability of a fluid flowing between two concentric circular columns and then expanded his results to vortex core motion.

Let us consider an inviscid flow with an infinite Reynolds number. Furthermore, let us assume it is conical and the vortex core is infinitely slender. Let us use the perturbation method to solve simplified equations. The perturbation term is a spiral perturbation. Based on this, we get the stability criterion:

$$\left(1-\frac{r}{w}\frac{\partial w}{\partial r}\right)\left[1-\left(\frac{r}{w}\frac{\partial w}{\partial r}\right)^2\right]-\left(\frac{5}{3}-\frac{r}{w}\frac{\partial w}{\partial r}\right)\left(\frac{r}{w}\frac{\partial u}{\partial r}\right)^2>0$$

Figure 5 shows the stability boundary. When $K<1.16$, vortex breakdown occurs. K is called a velocity parameter. This theory believes that the initial spiral perturbation will eventually lead to vortex breakdown. This was proven in reference [22]. It stresses the effect of non-symmetry of the vortex and can only be used to analyze spiral breakdowns. However, this theory cannot take the axial gradient of the external flow field into account. On the other hand, spiral perturbation does not necessarily exist in the upstream flow causing vortex breakdown. Reference [23] pointed out that some theoretical analyses even proved that all incoming flow causing breakdown remained stable with respect to any perturbation. /72

3. Quasi-cylindrical Vortex Core Model. Hall[24] first established the quasi-cylindrical model. Based on analogy in two-dimensional boundary layer separation, as well as through a series of numerical calculations, vortex breakdown occurs when the quasi-cylindrical vortex core model becomes invalid.

Inside the vortex core, $v=\varepsilon u$ where u and w are of the same order of magnitude. If we further assume $Re^{-1}=O(\varepsilon)$, then the

vortex core model equations can be derived from equations (1) and (2)[25]:

$$\frac{\partial(rv)}{\partial r}+\frac{\partial(ru)}{\partial x}=0 \tag{5}$$

$$\frac{w^2}{r}=\frac{\partial p}{\partial r} \tag{6}$$

$$\frac{\partial(vwr^2)}{\partial r}+\frac{\partial(uwr^2)}{\partial x}=\frac{1}{Re}\frac{\partial}{\partial r}\left[r^2\left(\frac{\partial w}{\partial r}-\frac{w}{r}\right)\right] \tag{7}$$

$$\frac{\partial(vur)}{\partial r}+\frac{\partial(u^2r)}{\partial x}=-\frac{r}{2}\frac{\partial p}{\partial x}+\frac{1}{Re}\frac{\partial}{\partial r}\left(r\frac{\partial u}{\partial r}\right) \tag{8}$$

It is parabolic in nature. Hall solved these equations by a difference scheme. References [25]. [26] and [27] obtained solutions by integration. Mager[26] employed a relatively simple velocity distribution to obtain an analytical solution. The axial momentum equation (8) and radial momentum equation (6) are integrated, respectively, to obtain

$$a=a^*\pm[(\tau-\tau^*)/K_{11}]^{1/2} \tag{9}$$

$$a=(R\theta_1-K_{10})/K_{01} \tag{10}$$

where $\tau=R(\theta_1-0.25\ \ln R)$. Equation (9) is a parabolic equation. When $\theta_1>\theta_1^*=0.163989$, the upper branch is connected to the

lower branch. Equation (10) is a linear equation. θ_1^* can be considered as the critical dynamic loss. The intersect of curves described by equations (9) and (10) is the solution. When $\theta_1 > \theta_1^*$, there are two possible solutions. The upper branch solution corresponds to the supercritical state and the lower branch solution corresponds to the subcritical state. The "break-through" from the upper branch to the lower branch corresponds to Benjamin's finite transition; i.e., bubble breakdown. The intersect a is a singular point, corresponding to spiral breakdown.

References [25] and [27] relatively systematically investigated the effect of Reynolds number, initial vortex core speed and circulation, and external flow speed, pressure and circulation gradient. Consequently, the breakdown mechanism was further understood. The analysis done by either Benjamin or Mager on the breakdown addressed uniform external flow conditions. As for a non-uniform external flow vortex, even if it is in a supercritical state upstream, it will not break down if the external flow gradient is approximately controlled. Reference [28] calculated the delta wing separation vortex positions at $\Lambda=65^o$, 70^o and 75^o by using a double layer model which agreed well with experimental results as shown in Figure 3. Recently, some authors attempted to more precisely plot the detailed structure of the breakdown zone by taking non-symmetry or unsteadiness[28, 29] into account.

IV. Conclusions

Tube vortex and leading edge separated vortex can produce similar axisymmetric and spiral breakdowns. Based on this fact, axisymmetry is the primary factor affecting the breakdown /73
mechanism. The supercritical and subcritical criterion has already been widely applied to vortices inside a circular pipe to determine whether a breakdown will occur. Analytical method or numerical solution can approximately show the internal structure of a broken down bubble. However, it is unable to calculate the internal structure of a spiral breakdown. The vortex core model accurately predicts various breakdown positions. Furthermore, it can be used to calculate wing separated vortex breakdown. Although the primary property of the vortex is axisymmetric, it is necessary to perfect existing mathematical models to include non-axisymmetry, unsteadiness and compressibility effects.

References

[1] Peckham, D.H., Atkinson, S.A., ARC CP 508 (1957).

[2] Lambourne, N.C. and Bryer, D.W., ARC RM 3282 (1962).

[3] Lin Bingqiu, Progress in Investigations on Separated Vortex Breakdown of Aircraft at High Attack Angles, Aerodynamic Journal, 1982/4.

[4] Harvey, J.K., J. Fluid Mech., 14, 585 (1962).

[5] Turgut Sarpkaya, J. Fluid Mech., 45, 545 (1971).

[6] Faler, J.H., Leibovich, S., Physics of Fluid 20, 9 (1977).

[7] Faler, J.H., Leibovich, S., Physics of Fluid 86, (1978).

[8] Zhang Jinzheng, Naitian Maonan and Zhongchun Jialong, Journal of Nanjing Institute of Aeronautics and Astronautics, Special Issue on Fluid Mechanics, Vol. 41, 1981.

[9] Torrance, K.E. and Kopocky, NASA CR-1865.

[10] Grabowski, W.J. and Berger, S.A., J. Fluid Mech., 75 (1976).

[11] Uchida, S. et al. JSASS, 24, 63 (1981).

[12] Fennell, L.J., ARC RM 3805, (1977).

[13] Liu Moji, New Advances in Vortex Studies, Report in Technical Discussion Meeting on Separated Flow and Vortex Motion, 1984, 4.

[14] Erickon, L.E., AIAA 79-1530.

[15] Lin Liangsheng and Zhonggu Huicheng, NAL TR-423 (1975).

[16] Wentz, W.H. Jr. and Kohlman, D.L., J. Aircraft 8, 3 (1971).

[17] Squire, H.B., Aero. Dept., Imperial Coll., London, Rep. 102 (1960).

[18] Benjamin, T.B., J. Fluid Mech., 14 (1962).

[19] Bossel, H.H., Physics of Fluid, 12 (1969).

[20] Randall, J.D. and Leibovich, S., J. Fluid Mech., 58 (1973).

[21] Ludwieg, H., Z. Flugwiss., 12 (1964).

[22] Hummel, D., Z. Flugwiss., 13 (1965).

[23] Leibovich, S., Annual Review of Fluid Mech., 10 (1978).

[24] Hall, M.G., Progress in Aeronautical Science, 7 (1966).

[25] Lin Bingqiu, Journal of Aerodynamics, 3 (1981).

[26] Mager, A., J. Fluid Mech., 55 (1972).

[27] Lin Bingqiu, Journal of Aerodynamics, 2 (1983).

[28] Shi Xungan, Numerical Simulation of Vortex Breakdown, Report in Technical Discussion Meeting on Separated Flow and Vortex Motion, 1984, 4.

[29] Ma Huiyang, Isolated Wave Model of Spiral Vortex Breakdown, Report in Technical Discussion Meeting on Separated Flow Vortex Motion, 1984, 4.

Numerical Analysis of a 3-D Separated Flow /75

Ma Yanwen

(Beijing Institute of Aerodynamics)

1. Introduction

A missile encounters various separated flows in its flight. An important technique to study separated flow is to solve Navier-Stokes equations by numerical methods. A great deal of progress has been made in the numerical simulation of two-dimensional problems. However, there are difficulties in three-dimensional flows. In addition to flow complexity itself, we are also limited by computer capacity and speed. Computational methods are still yet to be improved.

A one-step difference scheme was used in reference [1] to calculate a simple three-dimensional separated flow. Their results are analyzed here. In this paper, the physical model is described first. The calculated results are then analyzed. In addition, the characteristics of the three-dimensional separated flow are discussed.

2. Physical Model

As shown in Figure 1, a wedge is standing vertically on a plate. Over the plate, there is a uniform supersonic flow. Near the surface, there is a laminar attached layer. The wedge changes the direction of the flow (the plane of symmetry of the

wedge is z=0). The shock wave from the leading edge of the wedge interferes with the attached layer on the plate. In this work, the interference away from the wedge surface is analyzed by using numerical results (see Figure 1).

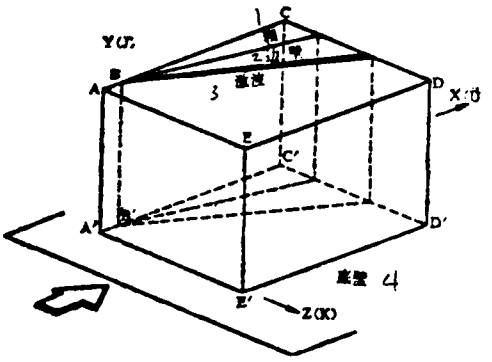

Figure 1. Computation Model

1. wedge
2. side wall
3. shock wave
4. bottom wall

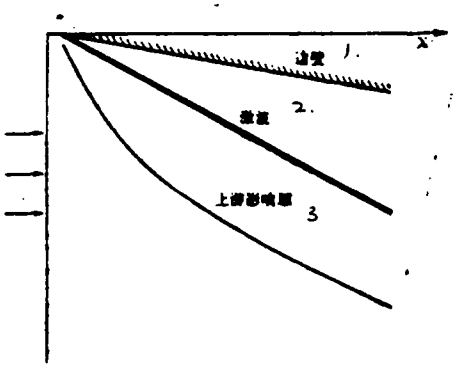

Figure 2. Upstream Affected Region in Interference Zone

1. side wall
2. shock wave
3. upstream affected area

The N-S equations were simplified by taking into account that the upward velocity component perpendicular to the bottom is small and the main flow is in the x-direction. In order to describe the flow characteristics in the interference in more detail, the y-direction coordinate was transformed. The simplified equations are in the one-step approximation scheme.

Manuscript received on June 11, 1984, revised manuscript received on September 3.

This one-step scheme has the advantages of appropriate accuracy, /76 ease of finding solution and good stability. In order to reduce the jumping effect in the numerical solution, a smoothing parameter is introduced. An adjustment factor is added in the difference equations to accelerate the converging process. The boundary conditions given are shown in reference [1].

In the flow field calculated, $M_\infty = 2.94$ and the shock wave angle is 27.82°. Two sets of calculations were made: one for $Re_\delta = 687.5$ and the other for $Re_\delta = 3000$. The mesh points in three directions are 25 x 31 x 31. The densifying factor in the coordinate transformation is b=25. Thus, there are approximately 10 mesh points in the attached layer. A stable solution can be obtained after 300 iterations.

3. Calculated Results and Analysis

Some results are shown in Figures 2-11. Figures 2-4 show the first set of results and Figures 5-11 are the second set. Figure 2 shows the upstream affected area due to interference between the shock wave and the attached layer. Figure 3 shows how the attached layer thickness varies. Based on this we know that the high pressure behind the shock wave makes the attached layer thinner. This suggests that there is an altitude in the interference region where the velocity component parallel to the inviscid shock wave and the base u_s is smaller in front of the wave than that trailing the wave. This is one of the reasons why the velocity mode changes in the interference region as we will discuss later. Figure 4 shows the lateral pressure distribution at I=20. On the surface j=1, a pressure plateau is obvious. Figure 5 shows the variation of velocity u (velocity component in x-direction) along y-direction on the cross-section I=20 at K=10, 15 and 20. K=10 is located behind the wave. In this case, u remains in a Blasius type of velocity distribution. K=15 is in the interference region. We can see the u is changing mode. Figure 6 shows y-direction velocity component v with changes in y at three different K points when I=20. We can see that in the wave front interference region (K=20), v is positive. In the wave tail region (K=10) v is negative. According to the pattern of u and v, we find that the fluid turns upward near the interference region and then deflects downward to flow through the interference zone. The z-direction velocity component w vs. y curve at I=20 is shown in Figure 7. In the inviscid region in

front of the wave (K=20), w=0. This means the flow moves along the x-direction. w is positive in the viscous layer. The fluid is deflected away from the wedge surface. In the inviscid region (K=10) behind the wave, the fluid moves parallel to the wedge surface. The flow above the viscous region is deflected toward the wedge. In the viscous region, it flows away from the wedge. This effect is ever more apparent.

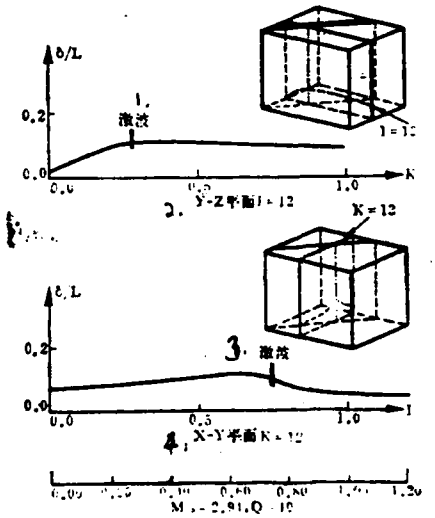

Figure 3. Variation of Attached Layer Thickness

1. shock wave
2. Y-Z plane I=12
3. shock wave
4. X-Y plane

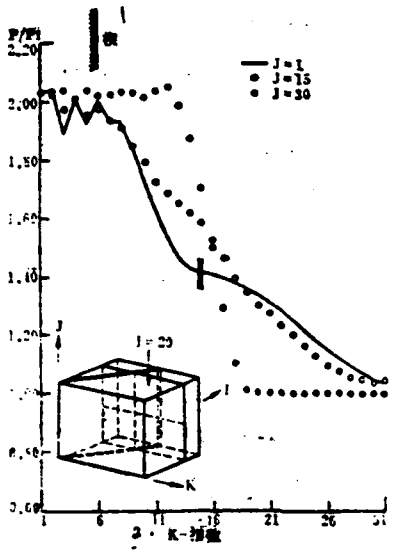

Figure 4. Pressure Distribution at I=20

1. wedge
2. K-index

Figure 8 shows the projection of velocity in the normal direction of the inviscid shock wave u_n against y at K=10, 16, and 22 when I=20. At K=16 and 22, we can see that u_n is negative near the surface. This indicates that the fluid flows backward in front of the inviscid shock wave above the viscous region. On the bottom, it flows forward. The u_n-v pattern recorded at I=20 (see Figure 9) illustrates the formation of flow separation. It resembles an ellipse. Its long axis is in the circulation zone pointing toward the surface. The high pressure behind the shock wave makes the latter half of the circulation zone stick to the surface.

/77

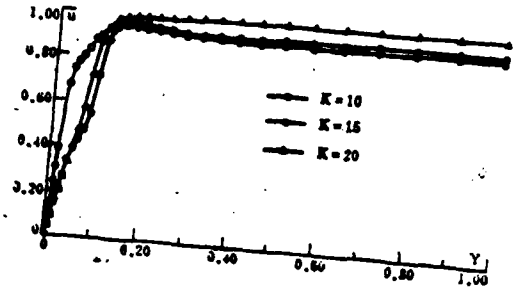

Figure 5. Velocity Models for u (I=20)

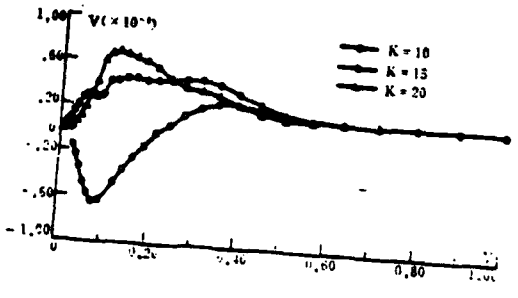

Figure 6. Velocity Models for v (I=20)

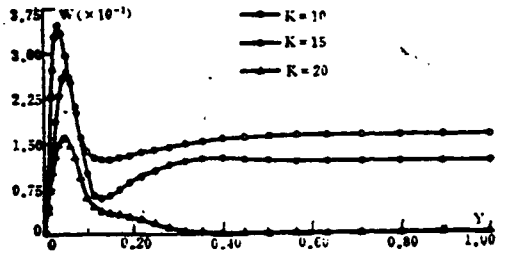

Figure 7. Velocity Models for w (I=20)

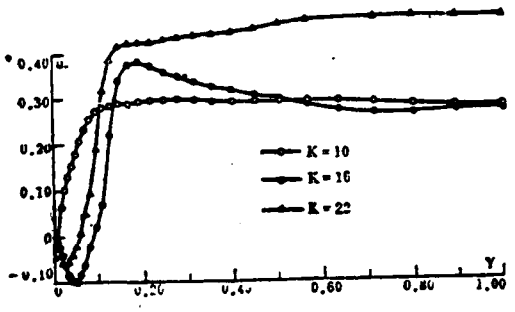

Figure 8. Velocity Models for u_n (I=20)

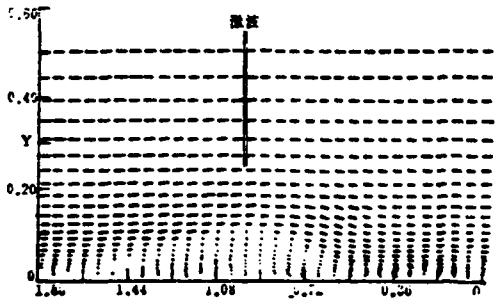

Figure 9. u_n-v Flow Field Pattern

In summary, based on the flow pattern, the mass in the upper half of the viscous layer moves downstream along the x-direction /78 and is slightly deflected upward after passing through the interference zone. Then, it is deflected downward and flows downstream parallel to the wedge surface. The mass in the inner layer moves downstream along the inviscid shock wave plane direction in a spiral form. Figure 10 shows u_s vs. y curves at various K values when I=20. u_s is the projection of velocity in the direction parallel to the inviscid shock wave and the base. It is obvious that u_s has modes other than the Blasius mode. It does not seem to be caused by error in computation and be interpreted physically. This change is caused by the thinning of the attached layer due to the high pressure of the latter half of the interference zone and the spiral motion in the interference zone. Because u_s is parallel to the shock wave, the value of u_s

is equal before and after the shock wave. In addition, because the attached layer near the high pressure region is thin, there is an altitude (Fig. 11) go at which the velocity u_s at point A_1 at this altitude level is less than the u_s at point B behind the inviscid wave front. It is also known that the mass inside the interference zone moves downstream in a spiral, thus a low velocity u_s mass point at A will penetrate the shock wave front and flow toward point B. This will slow the velocity at point B down (with respect to u_s at a point far away behind the wave at the same altitude). This is a reason why the model of u_s is changed.

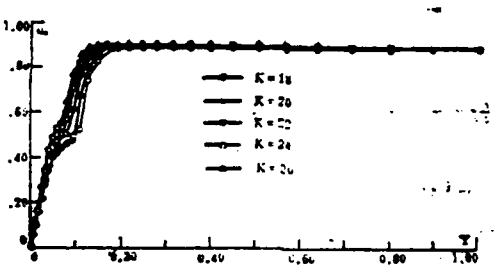

Figure 10(a) Velocity Model for u_s (I=20)

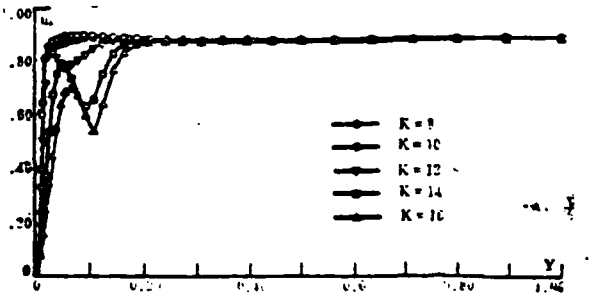

Figure 10(b) Velocity Model for u_s (I=20)

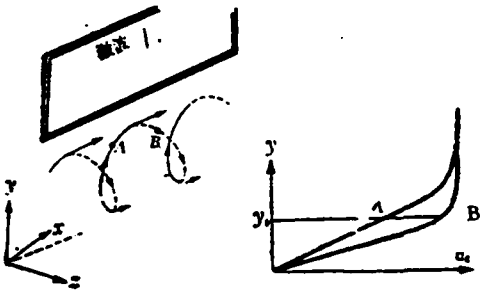

Figure 11. Schematic Diagram for Spiral Motion

1. shock wave

References

[1] Ma Yanwen and Cheng Xinyi, Journal of Aerodynamics, 2 (1983).

[2] Ma Yanwen, Computational Mathematics, 2 (1978).

Exact Vortex Solutions of the Navier-Stokes Solutions /80

Wu Jiezhi

(Chinese Institute of Aeronautics)

Since Rankine presented the two-dimensional vortex structure with vortex core in 1882, for over a hundred years only a few exact vortex solutions of NS equations were found. In addition to Oseen's work in 1912 which extended Rankine's vortex to unsteady viscosity, the next progress was made by Burgers[1] who extended the work to three-dimensional axisymmetric vortex and unsteady vortex[2,3], and by Sullivan[4] who extended the work to three-dimensional vortex with double cell structure (See Figure 1) and to unsteady cases[5]. Because it was found that a tornado has a double cell structure, Sullivan's vortex has attracted a lot of interest. Nevertheless, all the three-dimensional vortices discussed above have one assumption in common; i.e., the axial velocity $w=2az$. It becomes infinity when $z\to\infty$. At $z=0$, there is a stationary point which is not rational. The root of the problem is that the three velocity components are not properly coupled under realistic boundary conditions. As a matter of fact, the presence of a stationary point already suggests that a solid boundary should be introduced. With regard to the interaction between a semi-infinite straight vortex and an infinitive plane, because of the lack of a characteristic length, the solution should be similar to the conical case. Yih et al[6] proved that only the conical solution can provide a finite velocity at infinity. Hence, the conical solution may be more

realistic (except at the origin) than the axisymmetric solution. It is a natural tendency to study the conical vortex. It can be considered as the third stage of studying exact vortex solutions. In this paper, the author will briefly introduce the studies done in this area (details were reported in reference [7]).

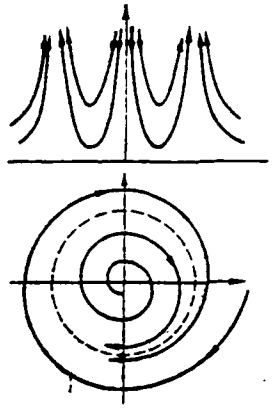

Figure 1. Sullivan's Double Cell Vortex

It was experimentally demonstrated[8] that only the vortex core of a turbulent vortex has a tendency to expand conically. It is not true for a laminar vortex. In addition, the viscosity of the turbulent eddy near the core is approximately constant. It was also demonstrated experimentally[9] that in order to make the vortex radius of Sullivan's solution realistic it is required to choose the dynamic viscosity v to be 480 times of the molecular viscosity. This suggests that we should consider the turbulent conical solution where the eddy viscosity is variable.

Let us assume that the flow field is steady. Based on the conical axisymmetric assumption, the velocity components in the α and θ direction of the spherical coordinate system (R, α, θ) can be written as

$$v_\alpha = \frac{F(x)}{r}, \quad v_\theta = \frac{\Omega(x)}{r}, \quad 0 \leqslant x \leqslant 1 \tag{1}$$

where $r = R\sin\alpha$ is the distance away from the z-axis ($\alpha=0$). $x=\cos\alpha$ is the only independent variable. The velocity component v_R

Manuscript received on June 14, 1984

can be expressed by a continuous function F(x). Let us assume /81 that the eddy viscosity ε is a function of x and denote $\varepsilon(x) = 1/2k\ \nu(x)$. The constant k is so chosen that $\nu(0)=1$. Furthermore, let $F=2\nu(1-x^2)f$. Then, after substituting equation (1) into the spherical incompressible NS equation, we can derive the following integral-differential equations:

$$\begin{cases} f' + f^2 = \dfrac{K(x)}{\nu^2(1-x^2)^2} & (2a) \\ \Omega'' + \left(2f + \dfrac{\nu'}{\nu\sqrt{1-x^2}}\right)\Omega' + \dfrac{2\nu' x}{\nu(1-x^2)^{3/2}}\Omega = 0 & (2b) \end{cases}$$

where

$$K(x) = k^2 G(x) + H(x), \tag{3a}$$

$$G(x) = 2(1-x)^2\int_0^x \frac{t\Omega^2}{(1-t^2)^2}dt + 2x\int_x^1 \frac{\Omega^2}{(1+t)^2}dt -$$

$$-[\Omega^2(0)+P](x-x^2)+Q(1-x) - \frac{x}{k^2}H(1) \tag{3b}$$

$$H(x) = \int_0^x \left\{ 2\left[(x+t) + \frac{t(x-t)^2}{(1-t^2)^{3/2}}\right]\nu' - (x^2-2xt+1)\nu''\right\}(1-t^2)\nu f\,dt \tag{3c}$$

Because we integrated three times when deriving equation (2a), and we employed a no-sink and no-source condition at the vortex axis x=1, therefore, there are two integration constants P and Q. Let us further specify the following boundary conditions.

(1) On the solid wall (x=0), the adherence condition is met.

(2) On the vortex axis, the regularity condition is satisfied.

These two conditions lead to

$$\begin{cases} \Omega = f = f' = 0 & \text{at } x=0 \\ \Omega = 0, \ f \text{ is finite} & \text{at } x=1 \end{cases} \tag{4}$$

Based on equation (2b), $\Omega \equiv 0$ is always a solution satisfying equation (4). In order to find the non-trivial vortex solution, we must introduce (this is the only way) a normalization condition

$$\Omega' = -1 \quad \text{at } x=1 \tag{5}$$

We can prove that $\Omega'(1) = -wR^2$ and w is the vortex on the axis. Hence equation (5) suggests a mechanism which maintains the vortex on the axis invariant. In reality, this requires importing energy from the other end of the vortex axis to overcome viscosity loss. This is equivalent to a model in which the interaction between the tornado and the ground is observed by moving the tornado forming cloud to an infinitely high altitude.

Based on equations (4) and (5), we get Q=0 and $P=-M/k^2$ where $M=H'(1)-H(1)$. In addition, we can derive the pressure distribution formula. Especially at x=0 and 1, we get

$$\frac{p-p_\infty}{\rho} = \begin{cases} \dfrac{M}{2k^2r^2} & \text{at } z = 0 \\ 0 & \text{at z-axis} \end{cases} \tag{6}$$

AD-A174 599 ACTA AERODYNAMICA SINICA(U) FOREIGN TECHNOLOGY DIV WRIGHT-PATTERSON AFB OH Z HANXIN ET AL 03 NOV 86 FTD-ID(RS)T-0367-86 3/3

UNCLASSIFIED F/G 20/4 NL

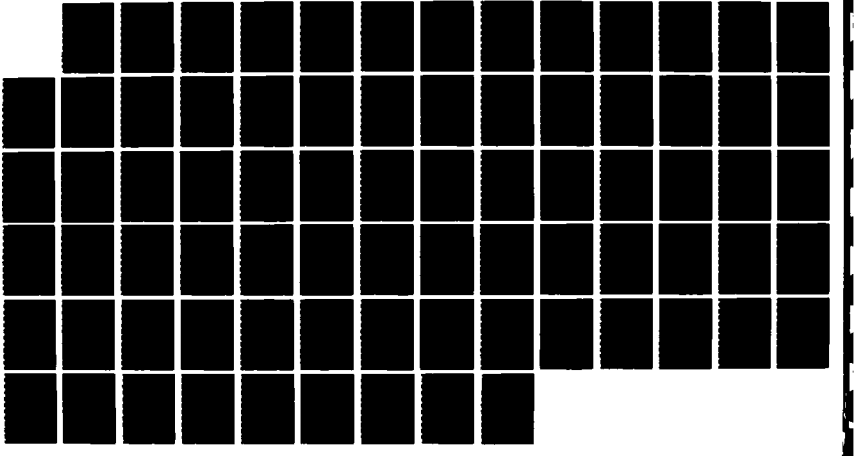

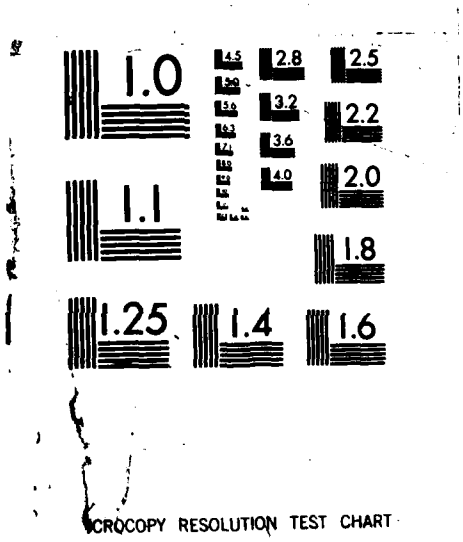
1.0
1.1
1.25
1.4
1.6
1.8
2.0
2.2
2.5
2.8
3.2
3.6
4.0
4.5
CROCOPY RESOLUTION TEST CHART

Up to this point, in addition to the parameter k which represents the Reynolds number, only the function v(x) remains to be defined.

Before we discuss the complicated situation for v, let us first review the case that v=const. Equation (2) was first /82 simplified by (Golvdshtik)[10] into the following elegant form:

$$\begin{cases} f'+f^2=\dfrac{k^2G(x)}{v^2(1-x^2)^2} & (7a) \\ \Omega''+2f\Omega'=0 & (7b) \end{cases}$$

Now, $H(x)\equiv 0$. Therefore, the right side of equation (7a) does not include f. G(x) is still expressed by equation (3b). Even more significant simplification occurs at equation (7b), which can be directly integrated. However, this simplification brings another fundamental difficulty. Equation (7b) only allows Ω to vary monotonically. Consequently, either $\Omega(0)=0$ or $\Omega(1)=0$ must be abandoned. Hence, we assume $\Omega(1)=1$ or $\Omega(0)=1$. These two new assumptions are both artificial. Therefore, either P or Q remains arbitrary and becomes another independent parameter. The assumption $\Omega(1)=1$ indicates that the adherence condition remains valid while vortex core has singularity. Serrin[11] established a complete mathematical theory for this case and proved the presence of a solution with respect to a parameter set (k, P). With respect to another (k,P) set, the solution did not exist. It was found that when the solution exists, various (k,P) subset flow fields have different shapes. There are single cell solution and double cell solution. On the other hand, the

assumption $\Omega(0)=1$ means that the regularity of the vortex core is maintained while the tangential velocity on the surface is allowed to be non-zero. Yih et al[6] used Serrin's method to study this situation and also obtained single cell and double cell solution with a certain (k,P) set (See Figure 2).

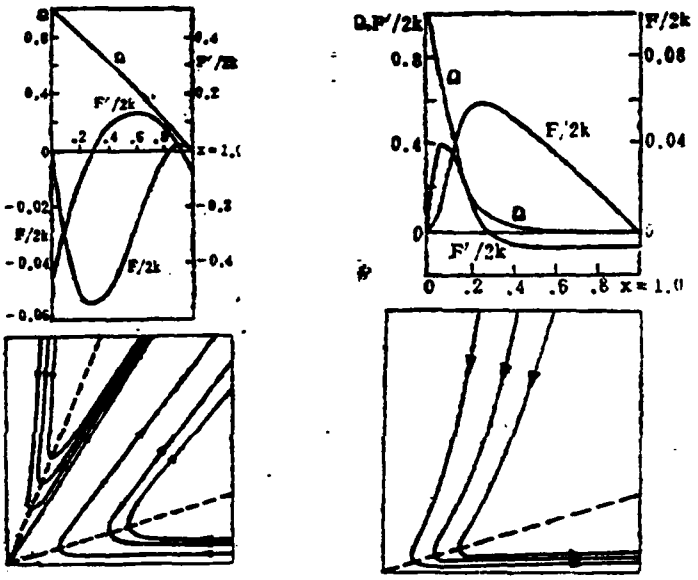

Figure 2. Laminar Conical Vortex Solution by Yih

Obviously, although these solutions are simple (numerical calculation is also required at the end), they are not satisfactory physically. Furthermore, the significance of the parameter P is not clear. In reality, their results proved that if steady conical vortex does exist in nature, it can only be

turbulent. This basic difficulty of the (Golvdshtik-Serrin) equations is the most important reason why we investigated variable viscosity. It is obvious from equation (2b) that variable $\nu(x)$ is a necessary condition for the existence of a solution of equation (4) and (5).

As for the functional form of $\nu(x)$, the only known limitation is the symmetry requirement $\nu'(1)=0$. Turner[12] and Serrin[11] believed that the turbulence in the tornado has a self-regulating mechanism. Hence, the problem becomes: What kind of form should $\nu(x)$ have so that a non-trivial solution exists for equation (2)-(5)? /83

Let us first assume f is fixed. Under conditions set by equation (4) and (5), equation (2b) leads to a singular eigenvalue problem. Through some expansion of existing second order eigenvalue theory[13], we proved that if

$$\frac{\nu'}{\nu}=\lambda\delta(x,\mu)$$

where μ is another positive parameter, then when $\delta(x;\mu)\leqslant 0$ $(0\leqslant x\leqslant 1)$ there is only a trivial solution. When $\delta(x;\mu)$ is non-negative and increases monotonically, there is a function $\delta(x;\mu)$ which makes $\mu\varepsilon[\mu_n,\mu_{n+1})$ have a finite series of eigenvalues $\lambda_0, \lambda_1,\ldots,$ $\lambda_i,\ldots,\lambda_n$. The corresponding eigen function $\Omega_i(x)$ has i zero points between (0,1).

Next, let us consider the entire set of equations (2). By using Schauder's non-moving point theory we proved that with specific parameters (k,μ), there is a set of solutions (Ω,f) where $f\geq 0$ $(0\leqslant x\leqslant 1)$. Therefore, it is a single-cell solution.

These existence theories are sufficient conditions. Hence, the possibility of a double-cell solution is not excluded. The final check will require numerical calculation.

It can also be proven that when v(x) is monotonically increasing between $0 \leq x \leq \varepsilon$ ($\varepsilon << 1$) and then remains constant, when $\varepsilon \to 0$, our solution approaches one of the single-cell solutions obtained by Yih[6]. In this case, the simplified equation (2a) can be used in the whole region. In $\varepsilon \leq x \leq 1$, equation (2b) is used. There is a boundary layer solution for Ω in $0 \leq x \leq \varepsilon$. It is only related to $\delta(x;\mu)$ and independent of f. This boundary layer solution behaves very differently from that of Serrin's solution at $x \to 0$. Therefore, Serrin's solution is not meaningful in maintaining the adherence condition. Yih's solution is more practical.

This is the first attempt over one hundred years to find the exact vortex solution of the NS equations (2)-(5) which satisfies all the physical boundary conditions (except the origin) by using an analytical method. This investigation using a simple model fully illustrates the complexity of the motion and its sensitivity to the boundary conditions.

Finally, it should be pointed out that if $\Omega(x)$ has i zero points between (0,1), then there are i co-axial alternating vortex loops which have not been observed in practice. They may be unstable.

References

[1] Burgers, J.M., Adv. Appl. Mech. 1 (1948), 197-199.

[2] Rott, N., Z.A.M.P. 96 (1958), 543-553.

[3] Rott, N., Z.A.M.P. 10 (1959), 73.

[4] Sullivan, R.D., J. Aero/space sci. 26 (1959), 767-768.

[5] Bellamy-Knight, P.G., J. Fluid Mech. 41 (1970), 673-687.

[6] Yih, C.-S. et al., Phys. Fluid 25 (1982), 2147-2158.

[7] Wu, J.Z., Preprint (I) (II) (1983), submitted for publication.

[8] Hoffman, E.R. & Joubert, P.N., J. Fluid Mech. 16 (1963), 395-411.

[9] Leslie, F.W. & Snow, J.T., AIAA J. 18 (1980), 1272-1274.

[10] (Гольдштик), М.А. (Прик.) Mat. Mex. 24 (1960), 610-621.

[11] Serrin, J., Phil. Trans. Roy. Soc., London A271 (1972), 325-360.

[12] Turner, J.S., J. Fluid Mech. 25 (1966), 377-400.

[13] Wu, J.Z., Preprint (1982).

Characteristic Analysis of Separated Flow

Fu Dexun

(Beijing Institute of Aerodynamics)

Abstract

The characteristics of three-dimensional separated flow are analyzed. In addition, starting from the fundamental physical phenomenon, based on the results of three-dimensional viscous separation provided by the numerical solution of the Navier-Stokes equations, as well as the experimental data, the necessary conditions for three-dimensional viscous flow separation and the definition of the separation streamline on the surface are presented.

1. The Problem

The separation of attached layer is an important phenomenon in fluid dynamics. It is also a frequently seen phenomenon in practice. As large computers are being developed, a great deal of progress has been made on this subject. Earlier, people thought $\tau_w=0$ on the surface is the separation point in a two-dimensional viscous flow. Later, Rott employed a numerical method to solve the Navier-Stokes equation and gave the flow field of a plate moving in a static fluid[1]. His results indicate that there is always a point where $\tau_w=0$. However, there is no separation or circulation region. In fact, it is not

sufficient to consider that the point at which $\tau_w=0$ in two-dimensional viscous flow is a separation point. We must require that a separation region exists behind this point because it is possible to have a flow where $\tau_w>0$ or $\tau_w\equiv 0$ in the entire flow[2]. Moore, Rott and Sear proposed the famous MRS criterion: in a coordinate system moving along with the separation point, the conditions for flow separation in a two-dimensional unsteady viscous flow are $u_0=0$ and $(\partial u/\partial y)_0=0$. These studies resulted in further understanding of the two-dimensional separated flow.

However, due to the complexity of three-dimensional viscous separated flow, many phenomena are still unclear. In recent years, many authors proposed various criteria for the separation of the three-dimensional attached layer. Most of them are not precise. In order to make the following discussion easier, four of them are listed below. (1) It was pointed out in reference [3] that the separation streamline of the three-dimensional attached layer is the boundary of the circulation zone where the fluid cannot penetrate. (2) References [4,5] pointed out that the separation streamline is the envelop of the limiting streamline. Furthermore, it is the singular streamline of the three-dimensional attached layer equation. (3) Reference [6] pointed out that the separation streamline is the limiting streamline passing through the point $\tau_w=0$. (4) Reference [7] pointed out that the necessary conditions for the three-dimensional attached layer separation are $\tau_w.\mathrm{grad}P=0$ and $U_1.\mathrm{grad}P>0$, where P is pressure, U_1 is the external flow speed and τ_w is the surface frictional drag. It should be pointed out that one

of our interests in studying the conditions for the separation of viscous flow to take place is the problem itself. On the other hand, we hope to determine whether separated flow exists based on the flow characteristics near the separation streamline. It is not difficult to realize that the first three criteria cannot meet this goal. Moreover, they are somewhat limited and are not general criteria for the three-dimensional separated flow. For example, in the viscous flow around a sliding cylinder of finite length, there is attached layer separation. However, there is no envelop of the limiting streamline. Nor is there a point where $\tau_w=0$. We believe the latter criterion is better. Nevertheless, it does not clearly define the separation streamline. In the following, based on the physical properties of separated flow, the necessary conditions for the separation of three-dimensional attached layer and the definition of the separation streamline are discussed.

Manuscript received on June 12, 1984. Revision received on September 10.

2. Characteristics of Three-dimensional Attached Layer Separation and Its Necessary Conditions /86

(1) Definitions

Let us consider a three-dimensional viscous flow around a curved solid wall. Let us establish a perpendicular coordinate system (x,y,z) where z is the normal direction of the curved surface. x and y are on the tangential plane of the curved surface (See Figure 1).

In order to facilitate the analysis, let us introduce the following definitions:

(i) Wall Frictional Drag: In a three-dimensional viscous flow, wall frictioning is a vector:

$$\vec{\tau}_w = \{\tau_{wx}, \tau_{wy}\}$$
$$\tau_{wx} = \mu_w \left(\frac{\partial u}{\partial z}\right)_{z=0} \qquad (1)$$
$$\tau_{wy} = \mu_w \left(\frac{\partial v}{\partial z}\right)_{z=0}$$

where u and v are velocity components in x and y direction, and μ_w is the wall viscosity coefficient.

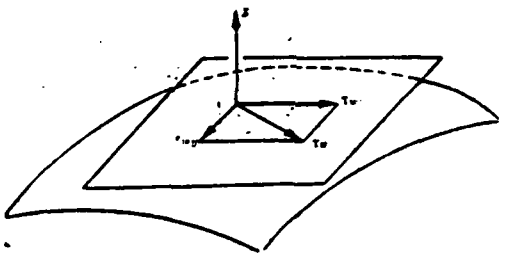

Figure 1. Schematic Diagram of the Coordinate System

(ii) Limiting Streamline: We realize that the solid wall has no flow. There is no streamline on the wall surface. The streamline immediately next to the wall is defined as the limiting streamline. The slope of this streamline on the wall can be defined by the following equation:

$$\frac{dx}{dy} = \frac{u}{v} \qquad (2)$$

Let us expand u and v into Taylor series at z=0:

$$\begin{cases} u=\left(\frac{\partial u}{\partial z}\right)_{z=0}\cdot z+\frac{1}{2}\left(\frac{\partial^2 u}{\partial z^2}\right)_{z=0}\cdot z^2+O(z^3) \\ v=\left(\frac{\partial v}{\partial z}\right)_{z=0}\cdot z+\frac{1}{2}\left(\frac{\partial^2 v}{\partial z^2}\right)_{z=0}\cdot z^2+O(z^3) \end{cases} \tag{3}$$

By substituting equation (3) into equation (2) and taking equation (1) into account, the following expression applies to the limiting streamline ($z\to 0$):

$$\frac{dx}{dy}=\frac{\tau_{wx}}{\tau_{wy}} \tag{4}$$

Based on equation (4) we know that the tangential direction of the limiting streamline coincides with that of the vector $\vec{\tau}_w$.

(iii) Accelerated Flow and Retarded Flow: The momentum equation for an ideal inviscid flow has the following form:

$$\frac{dU^2}{dt}=-2U\cdot \text{grad}\, P/\rho \tag{5}$$

We can see that when U.gradP<0, the velocity is in an increasing mode and when U.gradP>0, the velocity is in a decreasing mode. We define that in viscous flow that U.gradP<0 is accelerated flow and U.gradP>0 is retarded flow. Here, U is the velocity of the point mass, P is the pressure and ρ is the density.

(2) Properties of Two-dimensional Attached Layer Separation and Its Criterion

As a fluid flows around a solid wall, when the Reynolds number is sufficiently high, its viscosity effect is primarily exhibited in the attached layer near the wall. The cause of flow

separation can be simply described as follows: due to frictional losses, when the residual kinetic energy of the fluid in the attached layer near the wall is not sufficient to overcome the /87 pressure to let the fluid flow into the high pressure area downstream, the fluid is separated from the wall. At the same time, the mass outside the attached layer still flows forward. Based on this we know that the two major factors causing the separation of the attached layer are the friction drag $\vec{\tau}_w$ and pressure gradient gradP and their relationship with the kinetic energy of the fluid. In three-dimensional flow, when the fluid flows along an arbitrary curved surface, the streamline of the ideal flow is curved. Moreover, the direction of the pressure gradient and that of the velocity of the inviscid ideal flow U_1 do not coincide (See Figure 2 in which the x and y direction velocity modes are plotted).

Under such a pressure gradient, the fluid mass inside the attached layer is deflected more than that outside the attached layer. On top of it, due to friction, the kinetic energy of the mass near the wall is gradually decreasing due to friction. When the kinetic energy of the mass cannot resist the forward movement due to the negative pressure gradient, separation takes place. At this time, the projection of the velocity of the point mass near the wall is less than or equal to zero in the gradP direction; i.e., $U.gradP \leq 0$. Hence, the necessary condition for attached layer separation to take place is that such a flow area exists. In this region, the flow is accelerated inside the attached layer and it is retarded outside this layer. The

projection of the boundary of this region on the wall is the separation streamline. Taking into account that the tangential direction of the limiting streamline coincides with $\vec{\tau}_w$, the necessary condition for the separation of the three-dimensional attached layer was written in the following form in reference [7]:

$$\vec{\tau}_w \cdot \text{gradP} = 0, \qquad U_1 \cdot \text{gradP} > 0 \tag{6}$$

Here, U_1 is the velocity vector outside the attached layer. The separation streamline will be discussed as follows. Because grad $P \neq 0$, based on equation (6) we can see that there are two situations where the first condition is valid:

(1) $|\tau_w| = [\tau_{wx}^2 + \tau_{wy}^2]^{1/2} = 0$, 即 $\tau_{wx} = \tau_{wy} = 0$; (2) $\vec{\tau}_w \perp \text{grad}P$

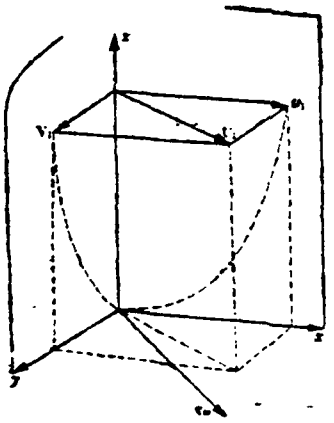

Figure 2. Schematic Diagram of the Velocity Model

We believe that the wall streamline is the limiting streamline whose tangential direction is perpendicular to gradP.

When at least one $|\tau_w|=0$ point exists, the separation streamline is an approximation of the limiting streamline passing through this point. For instance, in the zero attack angle viscous flow around a slender body, the pressure gradient goes along the surface. Therefore, the separation streamline is an approximation of the limiting streamline perpendicular to the object. Every point on the separation line corresponds to $|\vec{\tau}_w|=0$. However, when an attack angle exists for the same flow, two points on the separation line correspond to $|\tau_w|=0$; i.e., the two intersects between the separation streamline and the plane of symmetry. When there is no $|\tau_w|=0$ point, the separation streamline may be an approximation of the limiting streamline perpendicular to gradP. It may also be a limiting streamline. In the latter case, near the separation streamline, all limiting streamlines are perpendicular to gradP.

References

[1] Rott, N., Quarter 1 Appl. Math. 13 (1956), 444-451.

[2] Sears, W.R., Telionis, D.P., SIAM J. Appl. Mach., 28 (1975), 215-235.

[3] Moore, F.K., Adv. Appl. Mech., 4 (1956), 159-228.

[4] Peake, D.J., Rainbird, W.J. and Atraghji, E.G., AIAA J. 10 (1972), 567-580.

[5] Kenneth, F.S., AIAA, J. 10 (1972), 642-648. /88

[6] Avduyevskiy,V.S., Medvedev,K.I. Izvestiya AN SSSR, MZhG, (1966), No. 2

[7] G.M. Bam-Zemekovich. Izvestia AN SSSR, MZhG, 1970, No. 2

A Method Computing Viscous/Inviscid Interaction With Laminar Separation /89

Chen Zelin
(Beijing Institute of Aerodynamics)

Wu Jianmin
(University of Tennessee Space Institute)

Abstract

Based on the viscous/inviscid interaction model and the integral boundary layer equations, the equations for two-dimensional and three-dimensional incompressible laminar viscous/inviscid interaction are derived. These equations can be used in mild cases of separation and re-attachment. The method and examples are given in this paper. The two-dimensional results agree with other computational and experimental results. This method has the advantage of being simple and fast.

1. Introduction

It is well known that viscous/inviscid interaction in separated flow is very important. Although, in principle, this problem can be solved by Navier-Stokes equations, however, it is a very expensive and time-consuming way in practice. In recent years, a great deal of progress has been made in developing methods to calculate viscous/inviscid interaction based on boundary layer theory. These methods include direct and inverse techniques. Goldstein et al[1-3] pointed out that near the two-

dimensional separation point and re-attachment point, direct boundary layer methods will have singularity. Thus, direct methods cannot be applied to separated flow. In the inverse method, a given displacement thickness or wall shear force distribution can be used to avoid singularity[4-6]. The major characteristics of direct and inverse methods are shown in Figure 1.

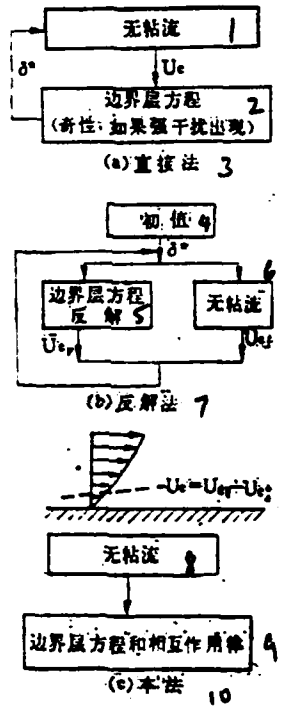

Figure 1. Schemes of Direct and Inverse Methods and This Technique

1. inviscid flow
2. boundary layer equation (singularity, if strong interference appears)
3. (a) direct method
4. initial value
5. inverse method for boundary layer equation
6. inviscid flow
7. inverse method
8. inviscid flow
9. interaction pattern and boundary layer equation
10. this method

Stewartson[7] introduced the three layer theory. On this basis, Veldman[8,9] presented an interacting boundary layer model. In this model, the velocity at the outer fringe of the boundary layer U_e is not known. Instead, it is a part of the solution. Furthermore, he assumed that U_e is a linear combination of the potential flow solution U_{e_0} and the perturbation velocity U_{e_δ}* due to viscosity, i.e.:

Manuscript received on March 17, 1984. Revised manuscript received on September 5.

$$U_e = U_{e_0} + U_{e_\delta}^* \qquad (1)$$ /90

He employed a difference method to calculate the two-dimensional laminar boundary layer with separation. Based on Veldman's interacting model, together with an integral form, the authors[10,11] presented an approximate method to calculate the two-dimensional or three-dimensional incompressible laminar or turbulent flow with separation and inviscid/viscous interaction (see Figure 1). This method will be described in detail in this paper. New examples are given. For ease of discussion, only laminar flow is involved. Please refer to references [10,11] for turbulent flow.

2. Computation of Two-dimensional Interacting Boundary Layer With Separation

(1) Integral Equation

The two-dimensional incompressible laminar boundary layer integral equation can be written as:

$$\frac{d\theta}{dx}+\frac{\theta}{U_e}(2+H)\frac{dU_e}{dx}=\frac{C_f}{2} \tag{2}$$

where U_e is the velocity at the outer fringe of the boundary layer, θ is the momentum thickness, H is the shape factor, and C_f is the local surface friction coefficient. We employed Thwaites' method[12]. The parameter λ is defined as:

$$\lambda=\frac{\theta^2}{\nu}\frac{dU_e}{dx} \tag{3}$$

where ν is the dynamic viscosity coefficient. In addition, the viscous/inviscid interaction pattern, equation (1), is adopted. Veldman[8,9] pointed out that in many cases it is only necessary to use the approximate expression for $U_{e\delta^*}$. If we adopt the incompressible thin wing theory,

$$U_{e\delta^*}=\frac{1}{\pi}\oint_{x_b}^{x_e}\frac{d}{d\xi}(U_e\delta^*)/(x-\xi)\,d\xi \tag{4}$$

Here, $[x_b,x_e]$ represents the important area for interaction. Equations (1) - (3) form the basic equations for the two-dimensional laminar viscous/inviscid interaction. After

mathematical operations, these equations can be written as:

$$\frac{d\lambda}{dx}=F_1\,;\quad \frac{dU_e}{dx}=F_2\,;\quad \frac{d\delta^*}{dx}=F_3 \tag{5}$$

Here, F_1, F_2, and F_3 are functions of boundary layer parameters (such as H, δ^*, C_f, etc.). The details are shown in reference [10] or the appendix of this paper.

(2) Computing Method

The initial condition of the above equations is that all parameters of the initial point are given. Because F_1 contains the unknown δ^*, iterations are required. First, an assumed value of $\delta^*(x)$ is given (usually the δ^* distribution of the laminar plate boundary layer is used). The equations can be pushed downstream by the Runge-Kutta method. The above procedure is repeated until δ^* converges. The iteration equation is

$$\delta^{*(n+1)}=\omega\,\bar{\delta}^{*(n+1)}+(1-\omega)\,\delta^{*(n)} \tag{6}$$

Here, $\bar{\delta}^*$ is the newest value of δ^* and ω is a relaxation parameter. Usually, super relaxation can be employed, e.g., $\omega=1.5$.

(3) Calculated Results and Discussion

The shape calculated - a "ditch" is shown in Figure 2. The shape of the ditch is given by the following equation:

$$y=-0.03\,\mathrm{sech}\,4(x-2.5)\qquad 1\leqslant x\leqslant 4$$

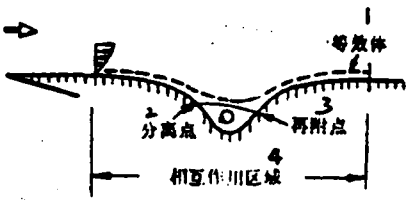

Figure 2. Profile Used in the Calculation

1. equivalent body
2. separation point
3. re-attachment point
4. interacting region

The calculation begins at x=1. The results are shown in Figure 3. The results of δ^* agree very well with Veldman's result[9]. The pressure coefficient, C_p, distribution are essentially in agreement with the results obtained by Veldman[9] as well as those by Carter and Wornom[13]. The calculation is rapid. It only took 4 seconds to calculate this example on a VAX-11.

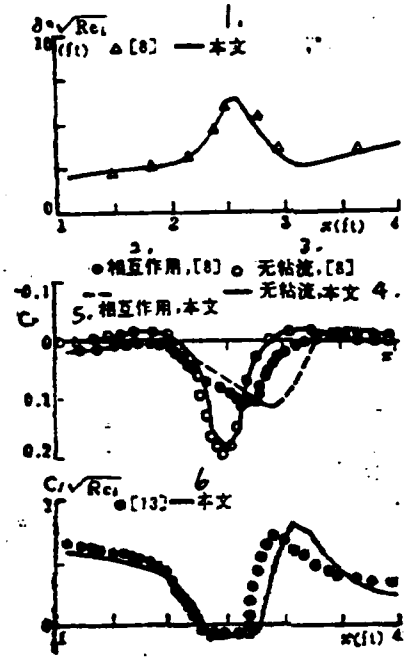

Figure 3. Results of Laminar Separation at the Ditch

1. this work
2. interaction
3. inviscid
4. inviscid, this work
5. interaction, this work
6. this work

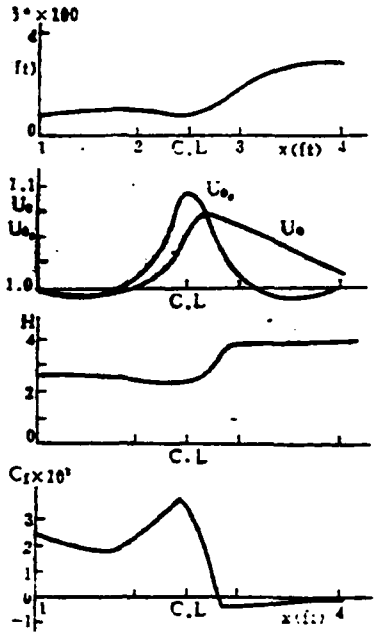

Figure 4. Separation of Plate Attachment Layer Under Cylinder

Another example is to calculate the plate laminar boundary layer under a cylinder. The calculation did not include the effect of the wake behind the cylinder. The separation conditions at two locations are shown. Figure 4 shows the separation bubble behind the cylinder center. Figure 5 shows that separation bubbles can appear in front and behind the cylinder center. In this case, the cylinder is very close to the plate. The example demonstrated the ability of this method to deal with some complex flows.

3. Calculation of Three-dimensional Interacting Boundary Layer With Separation

(1) Integral Method

A rectangular coordinate (x y z) is used. In this work, x is the free flow direction. The shape of the object is given by y=f(x,z). The momentum integral equations of the three-dimensional incompressible boundary layer in x and z direction are:

$$\frac{\partial \Theta_{11}}{\partial x}+\Theta_{11}\left[\frac{2}{U_e^2}\left(V_1\frac{\partial V_1}{\partial x}+W_1\frac{\partial W_1}{\partial x}\right)\right]\frac{\partial \Theta_{12}}{\partial z}+\Theta_{12}\left[\frac{2}{U_e^2}\left(V_1\frac{\partial V_1}{\partial z}+W_1\frac{\partial W_1}{\partial z}\right)\right]$$
$$+\Delta_1\left(\frac{1}{U_e}\frac{\partial V_1}{\partial x}\right)+\Delta_2\left(\frac{1}{U_e}\frac{\partial V_1}{\partial z}\right)=\frac{C_{f_x}}{2} \qquad (7)$$

$$\frac{\partial \Theta_{21}}{\partial x}+\Theta_{21}\left[\frac{2}{U_e^2}\left(V_1\frac{\partial V_1}{\partial x}+W_1\frac{\partial W_1}{\partial x}\right)\right]\frac{\partial \Theta_{22}}{\partial z}+\Theta_{22}\left[\frac{2}{U_e^2}\left(V_1\frac{\partial V_1}{\partial z}+W_1\frac{\partial W_1}{\partial z}\right)\right]$$
$$+\Delta_1\left(\frac{1}{U_e}\frac{\partial W_1}{\partial x}\right)+\Delta_2\left(\frac{1}{U_e}\frac{\partial W_1}{\partial z}\right)=\frac{C_{f_z}}{2} \qquad (8)$$

/92

Where Θ_{11}, Θ_{12}, Θ_{21}, Θ_{22}, Δ_1 and Δ_2 are defined in the conventional sense. U_e is the combined velocity at the outer fringe of the boundary layer. Its components in x and z direction are V_1 and W_1, respectively. C_{f_x} and C_{f_z} are the surface friction coefficients in x and z direction, respectively.

Based on the concept of Lighthill[14], the three-dimensional equivalent displacement thickness δ^* obeys the following equation:

$$\frac{\partial}{\partial x}\left(\delta^*\frac{V_1}{U_e}-\Delta_1\right)+\left(\delta^*\frac{V_1}{U_e}-\Delta_1\right)\frac{\partial U_e}{U_e\partial x}+\frac{\partial}{\partial z}\left(\delta^*\frac{W_1}{U_e}-\Delta_2\right)$$
$$+\left(\delta^*\frac{W_1}{U_e}-\Delta_2\right)\frac{\partial U_e}{U_e\partial z}=0 \qquad (9)$$

The viscous/inviscid interaction pattern is the same as the two-dimensional case; i.e., equation (1). It is written in a component form:

$$V_1 = V_{1_0} + V_{1_\delta}^* \qquad (10)$$

$$W_1 = W_{1_0} + W_{1_\delta}^* \qquad (11)$$

By using the thin wing theory approximation

$$V_{1_\delta}^* = \frac{1}{2\pi}\iint\frac{\partial(U_e\delta^*)}{\partial\xi}\frac{(x-\xi)}{r^3}\,d\xi d\eta \qquad (12)$$

$$W_{1_\delta}^* = \frac{1}{2\pi}\iint\frac{\partial(U_e\delta^*)}{\partial\xi}\frac{(z-\eta)}{r^3}\,d\xi d\eta \qquad (13)$$

Where $r=\sqrt{(x-\xi)^2+(z-\eta)^2}$. ξ and η are in the x and z direction, respectively. The integration region covers all the viscous/inviscid interaction significant region.

(2) Velocity Cross-section and Equations

In order to solve the above equations, velocity cross-section and auxiliary equations are the key. Usually, the velocity cross-section is decomposed into flow direction and transverse direction components. Coles[15] pointed out that the flow direction velocity cross-section of the three-dimensional

flow has the properties of the two-dimensional flow. In this work, we employed Thwaites' method to treat the flow direction velocity cross-section. The transverse velocity cross-section is more complicated. There is no general expression available to date. In this work, we used Mager's[16,17] incompressible transverse velocity cross-section. Thus, all transversal integral thickness is related to the momentum thickness in the flow direction θ_{11}. Their relationship is shown in reference [16].

By performing a geometric transformation from the streamline coordinate system to the rectangular coordinate system and using Mager's expression for the transverse flow, equations (1), (7), (8) and (9) can be converted into the following[10]:

$$F_{11}\frac{\partial\theta_{11}}{\partial x}+\theta_{11}F_{11}\frac{\partial\gamma}{\partial x}+\frac{\theta_{11}}{U_e}\left(-F_{11}\frac{W_1}{U_e}+2F_{11}\frac{V_1}{U_e}+F_1\right)\frac{\partial V_1}{\partial x}+\frac{\theta_{11}}{U_e^2}\times$$
$$\times\left(F_{11}V_1+2F_{11}W_1\right)\frac{\partial W_1}{\partial x}=S_1$$

$$F_{21}\frac{\partial\theta_{11}}{\partial x}+\theta_{11}F_{21}\frac{\partial\gamma}{\partial x}+\frac{\theta_{11}}{U_e^2}\left(-F_{21}W_1+2F_{21}V_1\right)\frac{\partial V_1}{\partial x}+$$
$$+\frac{\theta_{11}}{U_e}\left(F_{21}\frac{V_1}{U_e}+2F_{21}\frac{W_1}{U_e}+F_1\right)\frac{\partial W_1}{\partial x}=S_2$$
$$\frac{V_1}{U_e}\frac{\partial\delta^*}{\partial x}-F_1\frac{\partial\theta_{11}}{\partial x}-\theta_{11}F_1\frac{\partial\gamma}{\partial x}+\left(\theta_{11}F_1\frac{W_1}{U_e^2}-\theta_{11}F_1+\frac{\delta^*}{U_e}\right)\frac{\partial V_1}{\partial x}+ \quad (14)$$
$$+\frac{\theta_{11}}{U_e^2}\left(F_1V_1+F_1W_1\right)\frac{\partial W_1}{\partial x}=S_3$$
$$\frac{\partial V_1}{\partial x}-K_1U_e\frac{\partial\delta^*}{\partial x}=\frac{\partial V_{1e}}{\partial x}+S_4$$
$$\frac{\partial W_1}{\partial x}-K_2U_e\frac{\partial\delta^*}{\partial x}=\frac{\partial W_{1e}}{\partial x}+S_5$$

/93

Here, α is the angle between the streamline and the x-axis and γ is the angle between the outer fringe velocity of the boundary layer and the frictional force line. V_1 and W_1 are the velocity components at the outer fringe of the boundary layer which are "floating" as unknowns. They are determined by the viscous/inviscid interaction. V_{1_0} and W_{1_0} correspond to the inviscid velocity components. U_{e_0} is the overall inviscid velocity. Because the right side of the equation contains the unknown δ^*, it requires iterations to solve this equation. At each mesh point, there are 5 unknowns; i.e. θ_{11}, γ, V_1, W_1 and δ^*. There are five equations. The boundary condition is to give all parameters at the upstream boundary and the side boundary where the gas flow enters the stream.

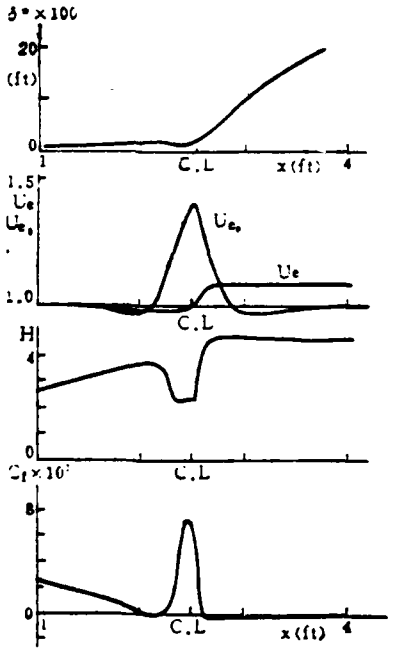

Figure 5. Plate Attached Layer Separation Under Cylinder (II)

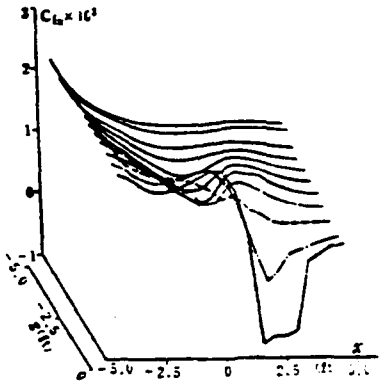

Figure 6. Plate Attached Layer Separation Under Sphere

(3) Computational Method

The procedures to solve the above equations are as follows: First, assume the δ^* distribution. Usually, a laminar plate δ^* distribution is adopted. Next, calculate the partial derivatives with respect to z. Here, we must consider the direction of the transversal flow. On the side boundary, use a forward or backward difference scheme. Then, use the Runge-Kutta method to proceed in the x-direction. Each step uses the new value of δ^*. /94 After reaching the downstream boundary, it is re-calculated until the δ^* distribution becomes convergent. The iteration equation is still equation (6). In most cases, it is required to use low relaxation, such as $\omega=0.5$.

(4) Results and Discussion

The example calculates the plate boundary layer under a sphere. Similarly, the effect of the wake is neglected. Figure 6 shows the local friction coefficient distribution along the x-direction. We can see that the computation illustrates the local separation case.

As mentioned above, δ^* iteration requires low relaxation which is different from the super relaxation case in the two-dimensional case. In that case, only one velocity component must be derived from δ^*. In the three-dimensional case, however, two velocity components must be formed based on δ^*. Hence, these two velocity components are coupled. Therefore, in the three-dimensional case, the number of iterations required far exceeds that in the two-dimensional case.

4. Conclusions

This paper introduces an approximate method to calculate the viscous/inviscid interaction with separation based on basic boundary layer assumptions. The results indicate that the velocity correction $U_{e_\delta}^*$ due to viscous perturbation can reach the same order of magnitude as the potential flow velocity; i.e., $O(U_{e_\delta}^*) \sim O(U_{e_0})$. Hence, this method can treat medium separation. The solution thus obtained, including the circulation zone, is rational. In the two-dimensional case, the results agree with other computational results and experimental data.

As compared to conventional methods to calculate

viscous/inviscid interaction, the time and capacity required by this method are significantly less because there is no need to repeat the inviscid portion in the iterations. The use of integral boundary layer equation also helps to reduce the demand on the computer. We believe that it can be applied to a variety of complex flow situation due to its simplicity and adaptability.

Appendix: Based on reference [10], the two-dimensional incompressible interacting boundary layer equations are:

$$\frac{d\lambda}{dx}=\left[\frac{\lambda v}{\theta^2}-R_{i_1}+\frac{v}{\theta U_e}Ha_{i1}\left(\lambda(H+2)-1\right)\right]\Big/a_{i1}\theta\frac{dH}{d\lambda}$$

$$\frac{d\theta}{dx}=\left[\frac{vl}{U_e\theta}-\frac{\theta}{U_e}(H+2)\left(R_{i_1}+a_{i1}\theta\frac{dH}{d\lambda}\frac{d\lambda}{dx}\right)\right]\Big/\left(1+\frac{\theta}{U_e}(H+2)Ha_{i1}\right)$$

$$\frac{d\delta^*}{dx}=H\frac{d\theta}{dx}+\theta\frac{dH}{d\lambda}\frac{d\lambda}{dx} \qquad \text{(A1)}$$

$$\frac{dU_e}{dx}=R_{i_1}+a_{i1}\frac{d\delta^*}{dx}$$

where

$$\frac{C_f}{2}=\frac{vl(\lambda)}{U_e\theta}\ ,\quad a_{i1}=\beta U_{e_{i_1}}C_{i1}\ ,\quad \beta=(\pi h)^{-1}\ ,\quad C_{i1}=-\frac{1}{(i-j)^2-\frac{1}{4}}\ ,$$

$$R_i=\beta R_i^*\ ,\quad R_i^*=-\frac{A_0}{i-\frac{1}{2}}+\frac{A_N}{i-N-\frac{1}{2}}\ ,\quad A_i=(U_e\delta^*)_i\ ,\quad A_N=(U_{e_0}\delta^*)_N\ ,$$

$$R_{i_1}=\frac{dU_{e_{0_1}}}{dx}+\frac{dR_i}{dx}+\sum_{j=1}^{i-1}a_{i1}\frac{d\delta_i^*}{dx}-\sum_{j=i+1}^{N}a_{i1}\frac{d\delta_i^*}{dx}$$

h is the step. $(\ )_0$ and $(\ )_N$ represent the starting point and the ending point, respectively.

References /95

[1] Goldstein, S., The Quarterly J. of Mechanics and App. Math, 1, 1, pp. 43-69 (1948).

[2] Brown, S.N. and Stewartson, K., Ann. Rev. Fluid Mech., 1, pp. 45-72 (1969).

[3] Moulden, T.H. and Wu, J.M., ZAMM, 52, pp. 248-249 (1972).

[4] Catherall, D. and Mangler, K.W., JFM, 26, pp. 163-182 (1966).

[5] Keller, H.B. and Cebeci, T., J. of Computational Physics, 10, pp. 151-161 (1972).

[6] Carter, J.E., NASA TR-R-447 (1975).

[7] Stewartson, K., Advances in App. Mech., 14, pp. 145-239 (1974).

[8] Veldman, A.E.P., NLR TR 79023 U (1979).

[9] Veldman, A.E.P., AIAA J., 19, 1, pp. 79-85 (1981).

[10] Chen, Z.L. and Wu, J.M., AIAA Paper 84-0267 (1984).

[11] Wu, J.M., Chen, Z.L. and Moulden, T.H., Proc. of the Southeastern Conf. on Theo. and App. Mech., Callaway Gardens, Pine Mountain, Georgia (1984).

[12] Cebeci, T. and Bradshaw, P., "Momentum Transfer in Boundary Layers", Hemisphere Pub. pp. 108-110 (1977).

[13] Carter, J.E. and Wornom, S.F., NASA SP-347, pp. 125-150 (1975).

[14] Lighthill, M.J., JFM, 4, pp. 383-392 (1958).

[15] Coles, D., JFM, 1, pp. 191-226 (1956).

[16] Smith, P.D., ARC R&M 3739 (1974).

[17] Mager, A., NACA R. 1067 (1952).

Numerical Computation of Extended Kalman Filter and Its Application to Aerodynamic Parameter Identification of a Reentry Satellite

Chen Qiongkang and Jiang Quanwei

(China Aerodynamic Research and Development Center)

Abstract

This paper describes several numerical computation problems to identify aerodynamic parameters by using an extended Kalman filter. The ultimate goal is to save computer time and memory to the extent possible and to improve the speed of computation. It is discussed in the following parts: optimization of numerical algorithm to solve the covariance matrix differential equations, computation of the Kalman gain and its correction, an algorithm to calculate the process noise in order to save computer time, and an independent verification method using numerical derivatives. These methods have been applied to the identification of aerodynamic parameters based on the reentry flight data of a certain satellite and the results obtained are satisfactory.

1. Introduction

To use an extended Kalman filter to identify aerodynamic parameters by numerical computation, there are generally three requirements:

(1) Fast Computing Speed. Because a great deal of computation is required for model selection, performance study and error analysis, increasing computing speed has significance in both computing efficiency and economic benefit. If we investigate real time estimation of aerodynamic properties by an on-board computer, then computing speed and memory storage become especially important. In this paper, an optimized numerical algorithm to solve the covariance differential matrix equation and to calculate the Kalman gain and its correction is introduced in Sections 2 and 3. As compared to unoptimized algorithms, the speed can be improved by five fold and the storage can be reduced by three fourths.

(2) Good Filter Characteristics. Due to various errors such as mathematical model, measurement and numerical computation, the aerodynamic parameter identified by an extended Kalman filter is divergent in some cases. In addition, if there is no process noise, the filter is more sensitive to computational error. In the fourth section of this paper a method to add process noise is introduced. The focus is placed on a numerical method to calculate this process noise to save computing time. It is a variable separation method.

(3) Accuracy of Filter Computation. In the extended Kalman filter computation for a large non-linear system with several variables, it is necessary to calculate a large number of partial derivatives. Their derivations are more complicated and mistakes are easily made. Next, the quality of the filter, to a large extent, depends on the variations of these partial derivatives in

their variable range (dynamic variables and parameters). In the fifth section of this paper, a numerical method is presented to calculate the partial derivatives which can independently verify the accuracy of an analytical partial derivative. It also can reflect the linearity of the dynamic system.

In this work, we combined our effort reported in reference [1] and referred to recent foreign publications [2], [3], [4], [5] and [6] to study the problems mentioned above. Our optimized numerical method is explained. A FORTRAN program was compiled. Many results were obtained on a Model 320 computer. Moreover,

Manuscript received on February 25, 1984, revision received on September 16.

it has already been applied to aerodynamic parameter /97
identification of satellite reentry with satisfactory results.

2. Optimized Numerical Method for Covariance Matrix Differential Equations

The non-linear random differential equation to determine the state of the system is given as follows:

$$\dot{\underline{X}}(t) = \underline{f}[\underline{X}(t), t] + \underline{W}(t) \qquad (1)$$

The measurement equation is a non-linear function of the state vector $\underline{X}(t)$ in a discrete form:

$$\underline{Z}_K = \underline{h}_K[\underline{X}(t_K)] + \underline{V}_K \qquad (2)$$

where $\underline{W}(t)$ is the Gauss white noise whose mean value is zero. the frequency spectrum density is $Q(t)$. $\underline{V}_K$ is the independent Gauss random sequence whose mean value is zero. The covariance matrix is R_K and K is the sampling sequence. The state vector $\underline{X}(t)$ comprised of the dynamic quantity $\underline{Y}(t)$ and the extended coefficient parameter $\underline{C}(t)$, i.e.

$$\underline{X}(t) = \begin{bmatrix} \underline{Y}(t) \\ \underline{C}(t) \end{bmatrix} \tag{3}$$

Therefore, equation (1) can also be written as

$$\dot{\underline{X}}(t) = \begin{bmatrix} \dot{\underline{Y}}(t) \\ \dot{\underline{C}}(t) \end{bmatrix} = \begin{bmatrix} \underline{g}[\underline{Y}(t), \underline{C}, t] \\ \underline{0} \end{bmatrix} + \begin{bmatrix} \underline{W}(t) \\ \underline{0} \end{bmatrix} \tag{4}$$

where $\underline{g}[\underline{Y}(t), \underline{C}, t]$ is a non-linear vector function. The superscript "." represents a derivative with respect to time t. The subscript "-" represents a vector.

In extended Kalman filter computation, it is necessary to solve a non-linear ordinary differential equation and an error covariance matrix differential equation:

$$\dot{\underline{X}}(t) = \underline{f}[\underline{X}(t), t] \tag{5}$$

$$\dot{P}(t) = F(t)P(t) + P(t)F^{T}(t) + Q(t) \tag{6}$$

where

$$F(t) = \frac{\partial \underline{f}}{\partial \underline{X}}\Big|_{\underline{X}=\hat{\underline{X}}(t)} \tag{7}$$

which is called the state matrix. $P(t)$ is a non-negative fixed matrix. The superscript "T" represents a matrix transformation $\hat{\underline{X}}(t)$ is the estimated value of the state vector.

In order to save computing time and storage, two important

properties of equation (6), i.e., the sparseness of the state matrix. F(t) and the symmetry of P(t) and $\dot{P}(t)$, are used to optimize the numerical method to solve equation (6). It is illustrated as follows:

The state matrix F(t) is a sparse matrix. Its non-zero elements are distributed in 1-S rows; i.e.:

$$F(t)=\begin{bmatrix} F_{ss} & F_{s\bullet} \\ 0 & 0 \end{bmatrix} \tag{8}$$

Here, F_{SS}(S x S) and F_S (S x a) are sparse matrices where S + a=N. S and a are the dimensionals of $\underline{Y}$ and $\underline{C}$, respectively. N is the order of the state matrix F(t). First, we employed the method reported in reference [3] to solve equation (6) by blocks. It takes less time than other conventional methods. However, the objective of maximum savings in computing time and storage is not met. To this end, we used the characteristics of the sparse matrix. The algorithm is to compress M non-zero elements into a /98 series of one-dimensional numbers AN. Furthermore, two series IA and JA are used to describe the data structure of the matrix F(t). AN and JA have M components each. IA has N + 1 components. Hence, there are 2M + N + 1 storage elements in this algorithm[7]. Based on the relation between these components in matrix operation, it is possible to find F(t)•P(t). By treating the non-zero elements of the matrix F(t) as vectors, the number of operations is the least.

Based on the calculated F(t)P(t) and the symmetry of P(t), we get $P(t)F^T(t) = [F(t)P(t)]^T$, i.e., $P(t)F^T(t)$ can be determined

by transformation. With the process noise Q(t), and numerical integration, we can find the solution P(t) of the covariance matrix equation (6). Due to the symmetry of equation (6), all calculations were made in the upper triangle of the matrix.

In the meantime, equation (5) is also numerically integrated. The integrated between two sampling points must be done in several steps. The solutions of equation (5) and (6) at the K^{th} sampling point are denoted as $\hat{\underline{X}}_K(-)$ and $P_K(-)$, respectively (K=1,2,.....), which are used as the estimated values.

3. Kalman Gain and Its Correction

The estimated state quantity and covariance matrix $\hat{\underline{X}}_K(-)$ and $P_K(-)$ must be corrected to obtain the corrections $\hat{\underline{X}}_K(+)$ and $P_K(+)$ at the K^{th} sampling point. The equations are:

$$K_K = P_K(-)H_K^T[H_K P_K(-) H_K^T + R_K]^{-1} \qquad (9)$$

$$\hat{\underline{X}}_K(+) = \hat{\underline{X}}_K(-) + K_K[\underline{Z}_K - \underline{h}_K(\hat{\underline{X}}_K(-))] \qquad (10)$$

$$P_K(+) = (I - K_K H_K) P_K(-) \qquad (11)$$

where K_K is the Kalman gain matrix. I is an N^{th} order unity matrix.

$$H_k = \left.\frac{\partial \underline{h}_k(\underline{X})}{\partial \underline{X}}\right|_{\underline{X}=\hat{\underline{X}}_k(-)} \qquad (12)$$

It is a measurement matrix, as well as a sparse matrix.

This section is concentrated with matrix operations. The same method as used in the previous section is used to store and

compute the non-zero elements of the sparse matrix H_K. The matrix $P_K(-)H_K^T$ is obtained and stored. Because equation (9) is used in two places, its transpose will be used in equation (11).

Due to the symmetry of $P_K(-)$ and R_K, computing $[H_K P_K(-) H_K^T + R_K]$ is carried out on one side of the main diagonal line. Its inverse is obtained by Cholesky decomposition in this paper. For a positive definite matrix A, we have $A=LL^T$. Here, L is a lower triangular matrix. Based on $A^{-1}=(LL^T)^{-1}=(L^{-1})^T L^{-1}$, after decomposing the matrix A, it is only required to find the inverse of the lower triangular matrix. The amount of computation is relatively small.

In order to simplify the program and to reduce the number of cycles, after the inverse matrix $[H_K P_K(-) H_K^T + R_K]^{-1}$ is obtained, we can sequentially calculate equations (9), (10) and (11) by using the results of each column vector of K_K. A FORTRAN program was written which consists of one external loop with four small loops.

4. A Time-saving Process Noise Computation Method

This work distributes six process noises into three force equations and three moment equations. The error of this mathematical model will be numerically integrated with other equations. Together with measurement noise, the simulated observation data for filter identification are obtained. Here, the process noise is considered as a stable Gauss process which is simulated by the following method[8]:

$$W_i(t) = \sum_{K=1}^{N_0} a_{iK} \sin(\omega_K t + \varphi_{iK}) \qquad (13)$$

$$i = 1,2,\ldots\ldots, 6$$

$W_i(t)$ represents the process noise, $\alpha_{iK} \sim N(0, \sigma_{ii}^2)$, φ_{iK} is a random number evenly distributed over $0 \sim 2\pi$, $\omega_K = (K-1/2) \times \omega_K/N_0$, ω_K, N_0, σ_{ii} are known.

It is obvious that equation (13) is the sum of N_0 terms of the sine series of the integral variable t. If we computer $W_i(t)$ directly, it takes a great deal of work in the forward problem. In order to save computer time, this article introduces a variable separation method to calculate the process noise (13). Specifically, equation (13) is expanded to separate the trigonometric function terms containing the time variable t from those that do not contain t; i.e.

$$W_i(t) = \sum_{K=1}^{N_0} (a_{iK} \cos\varphi_{iK} \sin\omega_K t + a_{iK} \sin\varphi_{iK} \cos\omega_K t) \qquad (14)$$

$$i = 1, 2 \ldots\ldots, 6$$

After the expansion, $\alpha_{iK}\cos\varphi_{iK}$, $\alpha_{iK}\sin\varphi_{iK}$ are independent of time, and can be calculated and stored. When numerically integrating equation (1), $\sin\omega_K t$, $\cos\omega_K t$ are two trigonometric functions related to time t. But, they are independent of the function number i. The number of times to call for sine and cosine functions is one third of that when directly calculating equation (13). In other words, this variable separation method can save two thirds of the computer.

5. Verification by Numerical Derivatives

As described above, two partial derivative matrices (7) and (12) must be calculated in filter equations. The partial derivatives are calculated using an analytic method. Its derivation is more complicated and it is more mistake prone.

In order to verify the accuracy of the analytical partial derivative, and to demonstrate the linearity between the non-linear functions $\underline{f}$ and $\underline{h}$, numerical partial derivative is sought in this work. For example, with respect to the matrix F, the computation formula is:

$$F_{ij} = \frac{f_i(\hat{X} + \Delta X_j) - f_i(\hat{X} - \Delta X_j)}{2\Delta X_j} \tag{15}$$

When Δx_j is chosen to be sufficiently small, equation (15) can accurately approximate the analytical partial derivative. When Δx_j is chosen to be the initial standard deviation of the state quantity, it is possible to show the linearity of the function $\underline{f}$ in the neighborhood of the initial standard deviation. Therefore, we choose $\Delta x_j = \alpha \sqrt{(P_{jj})_0}$ where α is a proportionality factor which is between 0.01~1.0, $\sqrt{(P_{jj})_0}$ is the initial standard deviation.

The computation shows that when α = 0.01~0.1 the analytical partial derivative agrees with the numerical partial derivative. When α = 1.0, the results are very close. This shows that the function $\underline{f}$ has a good linearity in the neighborhood of the chosen standard deviation. Similar computation can be made for H_{ij}.

6. Conclusions

This numerical method has been used in the identification of aerodynamic parameters based on the reentry flight data of a certain satellite. Major aerodynamic properties of the stars were identified based on high and low altitude data, respectively, including axial force, static stability and non-symmetric moment coefficient. The results are satisfactory.

In this work, we referenced the technical report by Comrade Xu Jinzhi on conventional methods. We wish to express our gratitude.

References /100

[1] Jiang Quanwei et al, "Determination of Aerodynamic Parameters of Reentry Object by Using Kalman Filter", Journal of Aeronautics, Vol. 3, 1982.

[2] Kelsey, J.R., Sand 78-2032 Feb. (1979).

[3] Kain, J.E., Brown, Jr., Lee, J.G., AIAAA Paper 78-1341.

[4] Kelsey, J.R., Petersen, D.P., AIAA Paper 78-1686.

[5] Kain, J.E., Brown, C.M., AFATL-TR-77-129.

[6] Xu Jianhua et al, "Estimation of State and System Identification", Science Publishing Co., (1981).

[7] Linear Algebraic Computation Method, Edited by the Computational Mathematics Special Field, Mathematics Department, Nanjing University, Science Publishing Co., (1979).

[8] (Japan) Authorized by Xingu Sheng, translated by Chang Baoqi, "Random Vibration Analysis", Earthquake Publishing Co., (1977).

Relaxation Phenomenon Behind A Bow Shock Wave In Dusty Gas /101

Zhao Guoying (Institute of Mechanics, Chinese Academy of Sciences)
Zhing Xichang (Center of Computation, Chinese Academy of Sciences)

The supersonic flow behind the explosion wave often contains dust. When a Pitot pressure gage is used to measure its total pressure, the effect of the dusty motion should be considered. When an object is traveling at high speed in an atmosphere containing raindrops, ice particles and fog, the effect of solid and liquid micro particles should also be taken into account. This type of problem is called the supersonic dusty flow. Its flow pattern is as follows: A bow shock wave is formed in front of the dull body. The flow velocity drops to zero when reaching the surface. When a micro particle passes through the shock wave plane, its parameters remain unchanged. Afterward, due to its retardation by the gas and the heat exchange between them, the particle velocity decreases and its temperature rises. When it reaches the surface, the dust particle still has certain normal velocity. They will bounce off the surface and be smashed. They can even erode the surface.

When analyzing this type of flow, most authors neglected the effect of the particles on the gas dynamics and used the trajectory theory to perform numerical analysis. Only Chang[1] considered the effect of the particles on the flow. However, the direct method and series expansion technique used by him is only applicable to high Mach number flows. In addition, because the drag coefficient equation is wrong, his results are only

qualitative. Besides, his temperature relaxation process is not even qualitatively accurate.

In this work, a two-way flow model and the straight line method is used to study the relaxation phenomenon numerically. The relaxation process of a dusty gas behind a blow shock wave is discussed in detail.

1. Basic Equations and Boundary Conditions

Let us assume that the gas is an ideal gas whose isobaric heat capacity C_p and specific heat γ are constants. The dust particles are identical spheres, evenly distributed in the flow. In addition, the inside of the sphere is at a uniform temperature. The size of the dust particle is far larger than the mean free path of the gas molecules. Therefore, compared to the momentum transfer between the dust particles and the gas, the shock wave thickness of the gas can be neglected. The particles occupy a very small percentage of the volume. Collision between particles can be neglected. The amount of particles is sufficiently high in the volume of interest. Consequently, it can be treated as a continuous medium. There are only momentum and energy exchanges between the dust and the gas. There is no mass transfer.

Under the above assumptions, the axisymmetric flow equation of a dusty gas without inviscid stress effect can be written as follows by using the boundary layer coordinate (See Figure 1):

For the gas

$$\frac{\partial}{\partial x}(\sigma u r) + \frac{\partial}{\partial y}(\sigma v r h_s) = 0 \qquad \text{(A)}$$

Manuscript received on March 12, 1984, revision received on August 13.

$$(\sigma u/h_x)\frac{\partial u}{\partial x}+\sigma v\frac{\partial u}{\partial y}+\frac{\sigma uv}{R_b h_x}=-\frac{\partial p}{\partial x}\Big/h_x+F_{gx}$$

$$(\sigma u/h_x)\frac{\partial v}{\partial x}+\sigma v\frac{\partial v}{\partial y}-\frac{\sigma u^2}{R_b h_x}=-\frac{\partial p}{\partial y}+F_{gy}$$

$$\sigma C_g\left[(u/h_x)\frac{\partial T}{\partial x}+v\frac{\partial T}{\partial y}\right]=\frac{u}{h_x}\frac{\partial p}{\partial x}+v\frac{\partial p}{\partial y}+W_i+Q_g$$

$$p=\rho RT$$

where σ is the gas concentration. $h_x=1+y/R_b$ where R_b is the radius of curvature of the surface and R is the gas constant. For the dust

$$\frac{\partial}{\partial x}(\sigma_g u_g r)+\frac{\partial}{\partial y}(\sigma_g v_g r h_x)=0$$

$$(\sigma_g u_g/h_x)\frac{\partial u_g}{\partial x}+\sigma_g v_g\frac{\partial u_g}{\partial y}+\frac{\sigma_g u_g v_g}{R_b h_x}=-F_{gx}$$

$$(\sigma_g u_g/h_x)\frac{\partial v_g}{\partial x}+\sigma_g v_g\frac{\partial v_g}{\partial y}-\frac{\sigma_g u_g^2}{R_b h_x}=-F_{gy}$$

$$\sigma_g C_s\left[(u_g/h_x)\frac{\partial T_g}{\partial x}+v_g\frac{\partial T_g}{\partial y}\right]=-Q_g$$

Here, σ_p is the dust particle concentration. The mutual interaction force is

$$F_{gx}=\sigma_g\frac{u_g-u}{\tau_m},\qquad F_{gy}=\sigma_g\frac{v_g-v}{\tau_m}$$

where $\tau_m = 4d_p^2 \rho_s / 3\mu C_D Re$, $Re = \sigma\sqrt{(u_p-u)^2+(v_p-v)^2}\, d_p/\mu$

where d_p is the particle diameter and ρ_s is its density. As for the drag coefficient C_D, the spherical drag coefficient standard curve is used.

$$C_D = \begin{cases} \frac{24}{Re}(1+0.0625Re-3.508\times10^{-4}Re^2+8.914\times10^{-7}Re^3), & Re \leqslant 180 \\ \frac{24}{Re}(3.1+0.0167Re), & Re > 180 \end{cases}$$

The heat exchange between the two planes is

$$Q_s = \sigma_s C_s (T_s - T)/\tau_T$$

where C_s is the specific heat of the particle material.

$$\tau_T = d_p^2 \rho_s C_s / 6kNu$$

where k is the thermal conductivity of the gas.

$$Nu = 2.0 + 0.459Re^{0.55}Pr^{0.33}$$

The work done by the dust particles on the gas is

$$W_k = \sigma_p[(u_p-u)^2 + (v_p-v)^2]/\tau_m$$

The boundary conditions for the above equations are: the parameters behind the bow shock wave are given by Hugoniot correlations.

$$h + V_N^2/2 = h_\infty + V_{\infty,N}^2/2, \qquad p + \rho V_N^2 = p_\infty + \sigma_\infty V_{\infty,N}^2$$

$$u = u_\infty - \left(1-\frac{\sigma_\infty}{\sigma}\right) n_x V_{\infty,N}, \qquad v = v_\infty - \left(1-\frac{\sigma_\infty}{\sigma}\right) n_y V_{\infty,N}$$

where the subscript N is the normal direction of the shock wave plane. n_x and n_y are the components of the unit normal vector of the wave front in x and y directions, respectively. The flow /103 condition for the solid particle behind the bow shock wave is:

$$u_p=u_\infty, \qquad v_p=v_\infty$$

On the surface, the normal velocity of the gas is zero; i.e., $v|_{y=0}=0$. As for the solid particles, let us assume that they are absorbed by the surface after they collide with it. We do not consider their burning, crushing and eroding processes.

2. Solving the Equations, Results and Discussion

Let us assume that the object is a sphere and the gas is air. Let us use the radius of the sphere R_b, incoming flow velocity V_∞, $\sigma_\infty, \sigma_\infty V_\infty^2$ and V_∞^2/R as the characteristic scales to make length, velocity, concentration (density), pressure and temperature dimensionless, respectively*. Let us assume that the shock wave surface equation is $y=f_1(x)$ and the surface equation is $y=f_2(x)=0$. Let us introduce the following transformations $\xi=y/f_1(x)$ and $\eta=x$. We solved the above boundary value problem by a linear method. The major concept, details and problems of the linear method are discussed in reference [2].

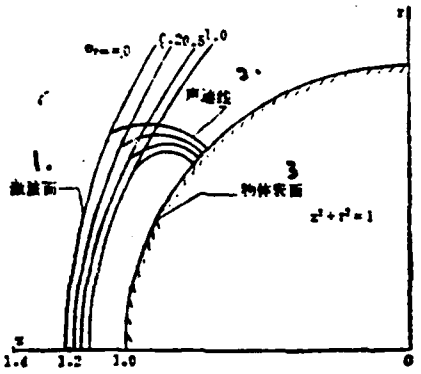

Figure 1. Shock Wave Shapes and Sonic Speed Streamlines at Various Particle Concentrations

1. shock wave plane
2. sonic speed streamline
3. surface

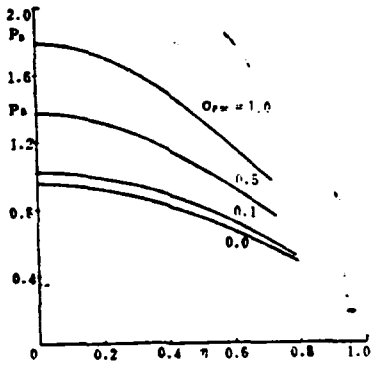

Figure 2. Pressure Distribution on Surface vs. Particle Concentration

In the stationary point zone, although a source term is added to the right side of the equation of motion due to the dust effect, the equation is still hybrid in nature. Therefore, there is no difficulty to use the straight line method to convert it into a boundary value problem of a regular differential equation. The dust particle equation is parabolic. Thus, as long as we do not consider particles bouncing off the surface, there is no problem to integrate it by the straight line method.

In this work, the above equations were solved by using the straight line method over a wide range of Mach number, $M_\infty(2\sim10^4)$, and $\sigma_{p\infty}(0\sim1.0)$. When there is order of magnitude difference between $B_1(=3C_D/4d_p\rho_s)$ and B_2 $(=8Nu/Re_\infty P_r C_D)$, due to the large difference between the relaxation distance of temperature and that of velocity, a stiff problem occurs in these equations. In our program, we employed the Treanor method[3] to eliminate this problem. We choose the situation $M_\infty=3$, $B_1=4.5$, $B_2=1.0$ (corresponding to $Re_\infty=6932$, $N_{u\infty}=54.6$), $\sigma_{p\infty}=0\sim1.0$, $C_p/C_s=1.0$ and $P_r=0.69$, the numerical results are shown in Figures 1-7 as well as in the table. Figure 1 shows the shock wave shapes and sonic streamlines at various $\sigma_{p\infty}$. The table lists the variation of separation distance Δ with $\sigma_{p\infty}$. As $\sigma_{p\infty}$ increases, the shock wave continues to get close to the surface. The sonic streamline moves upstream near the surface. When

*In the text below, with the expectation of quantities with *, others are dimensionless.

$\sigma_{p\infty}$ is small, the effect of particle motion on the gas flow field /104
is not significant. Figure 2 shows the variation of stationary point and surface pressure at different $\sigma_{p\infty}$. When $\sigma_{p\infty}$ increases, the surface pressure also increases. When $\sigma_{p\infty}$=1.0, the surface pressure increases one fold. Figure 3 shows the normal velocity of the gas and that of the particle. Although the relaxation process between them is similar to that in the normal shock wave case[4], and the only difference is located far away from the stationary streamline, despite both the gas and the particle having transversal velocity, yet the gas flow field has a transversal pressure gradient while it is not true for the particle flow field. Therefore, the relaxation process is much more complicated as compared to the normal shock wave case. Figure 4 shows the transversal velocity relaxation process using $\sigma_{p\infty}$=1.0 as an example. Far away from the stationary streamline, the transversal velocity relaxation distance is shorter than that near the stationary point. This is due to the effect of the gas pressure gradient. Near the surface, the transversal velocity of the gas is higher than that of the particle. The particle is carried by the gas.

Table Shock Wave Separation Distance vs. $\sigma_{p\infty}$ in Dusty Air When $M_\infty = 3$

$\sigma_{p\infty}$	0.0	0.01	0.10	0.50	1.00
Δ	0.2153	0.2137	0.2005	0.1618	0.1349
Δ/Δ_0	1.000	0.9926	0.9313	0.7515	0.6267

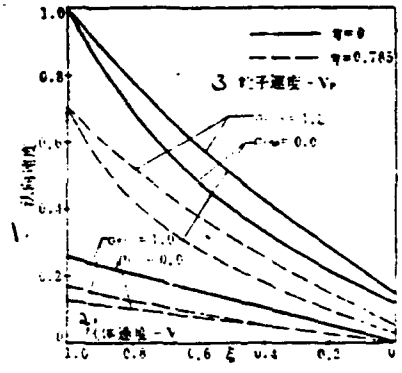

Figure 3. Variation of Normal Velocities of Gas and Particle

1. normal velocity
2. gas velocity
3. particle velocity

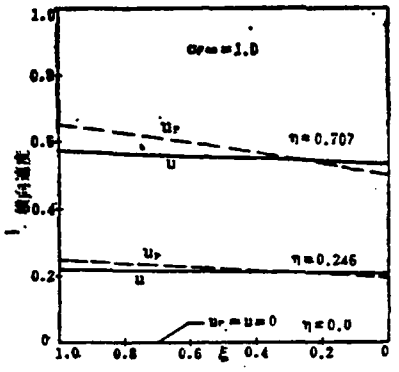

Figure 4. Variation of Transversal Velocities of Gas and Particle

1. transversal velocity

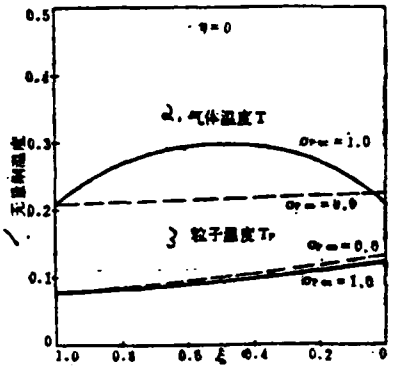

Figure 5. Gas and Particle Temperature Variation vs. σ_{p_∞}

1. dimensionless temperature
2. gas temperature T
3. particle temperature T

Figure 5 shows the relaxation process between the temperature fields of these two phases. Due to the fact that this is a slow process and the heat transferred from the gas to the particle behind the shock wave front is less than the frictional work done by the particle on the gas, the temperature rises when $\sigma_{p\infty}$ is not equal to zero. The particle temperature, however, does not vary significantly. (In the figure, the particle temperature is low when $\sigma_{p\infty}$=1.0, is attributed to the thinning of the shock wave layer.) This is different from Chang's results. Figure 6 shows /105 the particle concentration variation along the stationary streamline. It is apparent that its value is increased five fold. Away from the stationary streamline, the concentration increase is also more or less similar. Figure 7 shows the effect of the Mach number M_∞ and $\sigma_{p\infty}$ on the separation distance under the condition of B_1 and B_2 as described before.

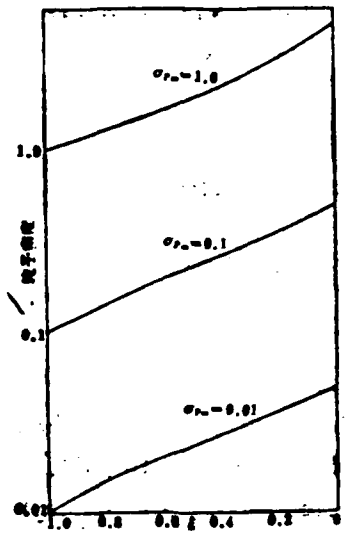

Figure 6. Variation of Particle Concentration Along Stationary Streamline at Various $\sigma_{p\infty}$

1. particle concentration

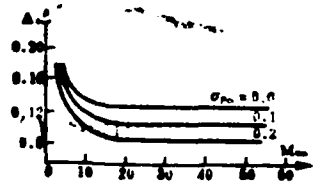

Figure 7. Variation of Separation Distance Δ With Different M_∞

Our computation shows that the relaxation process between these two phases is related to B_1 and B_2. B_1 controls the dynamic relaxation process and B_2 affects temperature relaxation. In the example given in this work, if B_1 and B_2 are increased, the relaxation process is gradually shifted near the shock wave. If B_1 and B_2 are decreased, the coupling of these two phases is reduced. As far as the effect of the particle on the gas flow field is concerned, we can use $\sigma_{p_\infty} B_1$ and $\sigma_{p_\infty} B_2$ as two combined parameters. Only when they are very small, we can solve the flow field in the stationary zone by single coupling. The entire computation shows that as long as B_1 and B_2 are equal, and σ_{p_∞} remains the same, the variation of the relaxation processes plotted in Figures 2~6 versus M_∞ is very small.

The method introduced here can be expanded to non-spherical head objects and non-axisymmetric flow. Non-equilibrium effects such as chemical reactions in the gas phase and phase transformation of the particles can also be concluded.

The authors wish to express their gratitude to comrade Yu Hongru for his guidance.

References

[1] Chang, S.S-H., Phys. Fluids, 18 (1975), 446.

[2] Zhu Youlan and Zhong Xichang, Difference Method and Flow For Initial Boundary Value Problem, Science Publishing Co., (1980).

[3] Treanor, C.E., Math. Comp., 20, 93 (1966), 39-45.

[4] Marble, F.E., Ann., Rev. Fluid Mech., 2, 397, (1970).

A Simple Formula of Drag Coefficient of Sphere in Rarefied Hypersonic Flow /107

Ma Jiahuan

(Institute of Mechanics, Academia Sinica)

Abstract

This paper presents a simple relationship of the spherical drag coefficient using the viscous parameter $K=M_\infty/\sqrt{Re_D}$, a variable which is suited for rarefied hypersonic flow. In the $Re_D = 5 \times 10^2 \sim 10^5$ and $M_\infty = 8 \sim 25$ range, it agrees with the experimental data. In addition, the dynamic pressures of calibrating spheres desired from the spherical drag coefficient based on this formula agree with those obtained by Pitot pressure measurements.

1. Introduction

The drag coefficient of a sphere in a rarefied hypersonic flow is a problem of great concern because it has many practical applications such as in estimating the drag and life of satellites and in high level atmospheric density measurements. We are concerned about this issue because the dynamic pressure is usually obtained by using a collaborating sphere when a model is tested in a hypersonic pulse wind tunnel. Thus, the drag coefficient of the sphere under the experimental conditions must be known ahead of time. Hence, it is necessary to provide a simple and accurate spherical drag coefficient formula.

As we all know, in a continuous hypersonic flow, the spherical drag coefficient is almost a constant. However, the flow region is not the concern. Once the flow enters the so-called skidding and transition regions, the spherical drag coefficient not only varies with the Reynolds number but also relates to the Mach number. In these flow regions, many experiments have been conducted abroad[9-11]. Nevertheless, at high Mach numbers, these formulas cannot totally reflect the variation of the drag coefficient. To this end, this paper presents a simple formula using the viscosity parameter $K = M_\infty\sqrt{Re_D}$ as a variable.

2. Presentation of the Formula

The flow regions are divided based on the viewpoint expressed in reference [12]. The mean free molecular path to boundary layer thickness ratio is used to express the magnitude of viscosity. Regions with different flow characteristics are thus defined as follows. When the mean free molecular path to boundary layer thickness ratio is $\lambda/\delta < 0.01$, it is a continuous flow. When $0.01 < \lambda/\delta < 1$, it is in a skidding region. When $\lambda/\delta > 0$, it is a free molecular flow. Between the skidding zone and free molecular flow, it is a transition zone. These regions are divided as shown in Figure1. In addition, we also included the various model experimental states tested in a coordinate system comprised of the Reynolds number and Mach number of a free flow using the calibrating sphere diameter as a characteristic length. In most

cases, as we can see, the free flying calibrating sphere does not belong to the continuous flow category. Of course, it is not proper if the same spherical drag coefficient is selected as in the continuous flow case.

Manuscript received on March 12, 1984. Revision received on September 29.

Table 1. Comparison of Dynamic Pressures Obtained by Free Flying Calibrating Sphere to Pitot Measurements /108

设备	M_∞	Re_∞(1/m)	Re_D	C_D	由标定球得 q_s(kg/cm²)	由皮托压力得 q_∞(kg/cm²)
JF4A	8.2	1.2×10^8	4.56×10^4	0.919	0.143	0.149
	8.2	5.6×10^8	2.13×10^4	0.928	0.129	0.110
	8.5	1.3×10^8	4.94×10^4	0.921	0.178	0.200
JF8	9.6	1.7×10^8	6.46×10^4	0.919	0.182	0.160～0.173
	13.5	4.5×10^8	1.71×10^4	0.952	0.043	0.042
JF4B	9.1	2×10^7	1.74×10^3	0.911	0.539	0.54
	9.9	1×10^7	1.40×10^3	0.913	0.292	0.291

1. equipment
2. q_s(kg/cm^2) obtained from calibrating sphere
3. q_∞(kg/cm^2) obtained from Pitot pressure

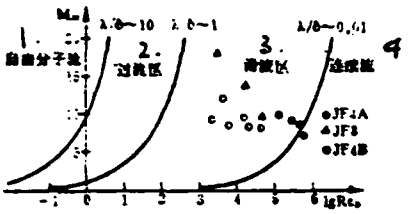

Figure 1. Division of Flow Regions

1. free molecular flow
2. transition region
3. skidding region
4. continuous flow

How should we choose the spherical drag coefficient value in this region? Based on the recommendation of reference [10], we made corrections by an increment $\Delta C_D \approx 1/\sqrt{Re_D}$ in the skidding zone ($Re_D = 10^2 \sim 10^4$). A great deal of experimental data was summarized in that paper. However, most experimental results were obtained in supersonic range. The formula of the drag coefficient of a sphere is given as follows:

$$C_D = 0.95 + 5/\sqrt{Re_D} \qquad (1)$$

where Re_D is the Reynolds number of the flow based on a characteristic length equal to the diameter of the sphere and C_D is the total drag coefficient of the sphere. The linking of the experimental value of the drag coefficient in hypersonic continuous flow is considered primarily based on the result reported in reference [13] = $C_D = 0.915$. Hence, we recommended the following formula in reference [14].

$$C_D = 0.899 + 5/\sqrt{Re_D} \qquad (2)$$

It is obvious that this equation cannot reflect the effect of Mach number. When the Reynolds number is still relatively large, such as $Re_D \geq 10^4$, the effect of viscosity is a small correction term because inertia is still the primary force; the formula can still be used without causing major deviations. However, in a hypersonic flow, when the Reynolds number is even smaller, the limitation of this equation, same as that of equation (1), is even more obvious.

Let us introduce the spherical drag relationship presented in reference [11] which is also a result of an analysis of a great deal of experimental data, particularly the target data measured by A.B. Bailey and J. Hiatt[5]. It is a new relationship derived based on a theoretical analysis to calculate the drag coefficient of a sphere. It incorporates the effect of wall temperature and considers the applicability of the entire flow region. In the hypersonic region, it can be expressed as:

/109

$$C_D = \frac{0.9 + \frac{0.34}{M_\infty^2} + 1.86\left(\frac{M_\infty}{Re_D}\right)^{1/2} \times \left[2 + \frac{1}{S_\infty^2} + \frac{1.058}{S_\infty}\left(\frac{T_W}{T_\infty}\right)^{1/2} - \frac{1}{S_\infty^4}\right]}{1 + 1.86\left(\frac{M_\infty}{Re_D}\right)^{1/2}} \qquad (3)$$

Where S is the molecular speed ratio; $S_\infty = M_\infty \cdot \sqrt{\gamma/2}$; γ is the specific heat of the gas; T_W is the wall temperature of the sphere and T_∞ is the temperature of the incident flow.

This formula takes various factors influencing the drag coefficient of the sphere into account. Nevertheless, its applicable range is limited to the supersonic region where $M_\infty < 6$. In the hypersonic case, let us first examine the variation of the

spherical drag coefficient in the region (See Figure 2). This figure comes from reference [9] which uses Re_D as a variable parameter. It shows the pattern how drag coefficient varies Mach number. The solid lines are the distribution patterns obtained by a large number of data points.

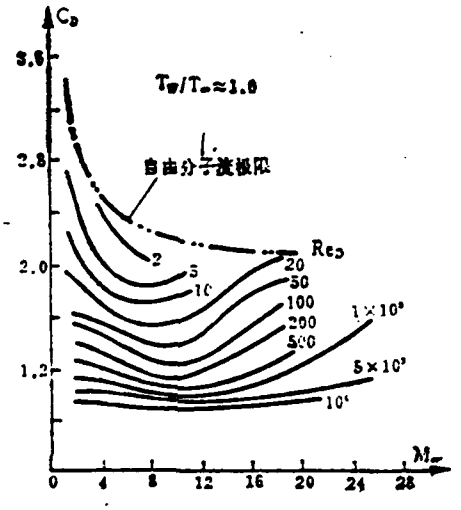

Figure 2. Hypersonic Spherical Drag Coefficient Over a Large Range

1. free molecular flow limit

As we can see, when $M_\infty < 6$, the drag coefficient of the sphere decreases as M_∞ increases. This is consistent with the trend given by equation (3). After $M_\infty > 10$, however, the drag coefficient increases as M_∞ increases. This trend is especially obvious when Re_D is very small. In this case, equation (3) cannot reflect this trend. We believe that the reason why the drag coefficient of a sphere in a rarefied hypersonic flow increases rapidly with

increasing Mach number is because the shock wave is adhered closer to the surface at hypersonic speeds. In addition, because the gas stream is rarefied, the boundary layer thickness is larger. Therefore, a viscous interference between the shock wave and the boundary layer, similar to that frequently found in the hypersonic flow around a dull slender body, will take place. Consequently, the drag coefficient is significantly increased. For this reason, we suggest to use the viscous parameter $K=M_\infty/\sqrt{Re_D}$ to express the drag coefficient, similar to the division of flow characteristic region. Through an order of magnitude analysis, in the range of concern $Re_D>>1$, we know that the viscous parameter K is proportional to λ/δ. We use $K=M_\infty/\sqrt{Re_D}$ to express the variation /110 of drag coefficient of a sphere in a rarefied hypersonic flow. Furthermore, we consider the fact that there should be no discontinuities in this formula in the case of continuous flow where the viscosity effect is minimal. Thus, the following equation is given:

$$C_D=0.9+\frac{1}{2}\cdot\frac{M_\infty}{\sqrt{Re_D}} \tag{4}$$

The applicable range of this formula is

$$M_\infty = 8\sim25, \qquad Re_D = 5 \times 10^2\sim10^5 \tag{5}$$

It corresponds to K=0.025~1.10. The formula is simple and neat. It can reflect the variation of drag coefficient in hypersonic rarefied flow over a large range. The trend of increase in the M_∞ drag coefficient calculated based on this formula agrees with that reflected by a great deal of experiments at high Mach numbers.

Only when $Re_D = 1 \times 10^3$, its deviation becomes significant. The maximum deviation can reach 14%. In other situations, the deviation is much smaller. Especially when $Re_D > 10^4$, the calculated results agree well with the experimental points.

Now, let us compare the spherical drag coefficients in hypersonic rarefied flows measured in shock tube wind tunnels in references [7] and [15] to the values calculated based on this equation. They are shown in Figure 3 using the viscous parameter $K = M_\infty / \sqrt{Re_D}$ as the coordinate. The straight line in the figure 3 is derived from equation (4) which is very close to the experimental values obtained at four Mach numbers.

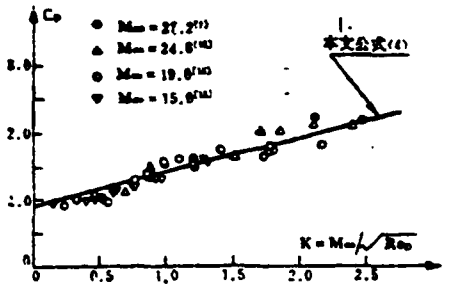

Figure 3. Comparison of Spherical Drag Coefficient to Experimental Data

1. equation (4) in this paper

In addition, the drag coefficients derived from equation (4) also agree with the dynamic pressures obtained with free flying calibrating spheres and Pitot force measurements in shock tubes and cannon wind tunnels (See Table 1).

Finally, it should be pointed out that the ratio of the wall temperature of the sphere to the flow temperature has an effect on its drag coefficient. Reference [16] was dedicated to studying this problem. Its result shows that the effect of wall temperature is relatively small when the Reynolds number is high. In the applicable range of the equation, as long as the wall temperature is not much higher than the flow temperature, this effect can be neglected. As for other factors, such as the effect of sphere material and surface condition investigated in reference [7], no influence was found within the accuracy of measurement. As a simple formula, the effect of secondary factors is not reflected in this work.

3. Conclusions

In this work a simple formula to calculate the drag coefficient of a sphere in hypersonic rarefied flow is introduced. A viscous parameter, $K = M_\infty/\sqrt{Re_D}$, is used as a convection factor to reflect the changes of the drag coefficient with Re and M_∞. In the applicable range of the formula: $M_\infty = 8\sim25$; $Re_D = 5 \times 10^2 \sim 10^5$, the calculated results are in agreement with a vast number of experimental data.

Furthermore, the formula also agrees with the dynamic

pressures measured by calibrating spheres and with Pitot pressures. We believe that this formula offers a convenient way to calculate the drag coefficient with good accuracy when we make measurement of free flights in rarefied hypersonic flows.

References /111

[1] Kane, E.D., J.A.S. Vol. 18 No. 4 (1951.4).

[2] May, A. & Witt, W.R., J.A.S. Vol. 20 No. 9 (1953.9).

[3] May, A., J.A.P. Vol. 28 No. 8 (1957.8).

[4] Kinslow, M. & Potter, J.L., AIAA J. Vol. 1 (1963).

[5] Bailey, A.B. & Hiatt, J., AEDC TR 70-291 or AD 721208 (1971.3).

[6] Phillips, W.M., AIAA J. Vol. 9 No. 7 (1971.7).

[7] Kussoy, M.I. et al., AIAA J. Vol. 8 No. 11 (1970.11).

[8] Bailey, A.B., AEDC TR 66-59 (1966.5).

[9] Bailey, A.B. & Hiatt, J., AIAA J. Vol. 10 No. 11 (1972.11).

[10] Hoerner, S.F., Fluid Dynamic Drag (1965).

[11] Henderson, C.B., AIAA J. Vol. 14 No. 6 (1976.6).

[12] Qian Xuesheng, J.A.S., Vol. 13 No. 12 (1946.12).

[13] Hodges, A.J., J.A.S. Vol. 24 No. 10 (1957.10).

[14] Ma Jiahuan, Tang Zongheng and Zhang Wanqing, Information on Mechanics, (1976) Vol. 4.

[15] Kussoy, M.I. & Horstman, C.C., AIAA J. Vol. 8 No. 2 (1970.2).

[16] Whitfield, D.L. & Smithson, H.K., AEDC TR 71-83 or AD726092 (1971).

Alleviation and Control of Asymmetric Load at High Angle of Attack

Yang Yongnian

(Northwestern Polytechnical University)

Abstract

This paper introduces several methods to alleviate and control asymmetric load at high angles of attack, as well as their research status and typical results. Comments on active control of asymmetric load in a wind tunnel are presented.

Symbols

a	angle of attack	C_y	lateral force coefficient
a_{onset}	onset angle	C_n	yawing moment coefficient
C_l	rolling moment coefficient	C_u	blowing coefficient

1. Introduction

In recent years a great deal of work on the aerodynamic characteristics at high attack angles has been done by scholars in the field. In particular, a large number of reports have been published to describe the occurrence and development of asymmetric load at high angles of attack, and the visualization and measurement of flow patterns in leeward areas, through experimental research. The results of these studies show that when an aircraft is flying symmetrically at a high angle of attack, asymmetric loads which vary according to a complicated

pattern will occur which is unfavorable. In addition, after stalling, the rudder efficiency drops. the maneuverability and operability of the aircraft will deteriorate. In this case, the asymmetric load at high attack angles may be used to improve the lateral maneuverability and controllability of the aircraft. Thus, the subject of alleviation and control of asymmetric load was brought up. It is necesary to find an appropriate way not only to alleviate the deleterious effect of asymmetric load at high angles of attack but also to improve the performance of the aircraft. Various methods of alleviation and control were presented. The concept of active control was introduced. Due to the complexity of this problem, it is still in the feasibility stage. Nevertheless, it is a topic of importance for further research.

This paper reviews several methods presented in recent years to alleviate and control asymmetric load at high angle of attack and presents their typical results. These methods are: installing transition strips at the nose, installing rings or fixed strakes at the nose, changing nose shape, rotating nose, controlled strakes and blowing vortex control. Finally, some ideas on active control in wind tunnels are also presented.

The methods mentioned above and the typical results are briefly described as follows:

2. Transition Strip

The most commonly used method to alleviate the asymmetric

load at high angles of attack is to install a transition strip at a suitable place on the nose to change the attached layer to a turbulent attached layer to reduce the separation zone. Thus, the onset of the asymmetric vortex in the leeward region is delayed and its asymmetry is weakened[1~4]. Typical results are shown in Figure 1a.

Manuscript received on June 14, 1984, revision received on September 18.

3. Ring on the Nose or Fixed Strake /113

Reference [5] reported the wind tunnel experimental results of the nose of a rotating body installed with a ring or a fixed strake. The results showed that asymmetric load could be reduced by adding a ring or a fixed strake at the nose and the onset angle was increased. The experimental results are shown in Figures 1b and 1c, respectively.

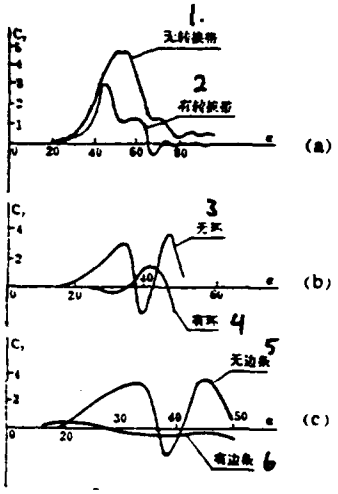

Figure 1. Typical Experimental Results of Transition Strip, Ring and Fixed Strake

1. without transition strip
2. with transition strip
3. without ring
4. with ring
5. without strake
6. with strake

4. Changing Nose Shape

References [6] and [7] pointed out that the geometric shape of the nose has an important effect on the asymmetric load. Major parameters affecting the asymmetric load include: aspect ratio of the nose, baseline shape, radius of curvature at the tip of the nose, and the cross-sectional shape of the nose. Experimental results show that reducing the aspect ratio of the nose,

increasing the radius of curvature at the tip, increasing the concave curvature of the baseline and increasing the horizontal width of the nose (i.e. locating the major axis of the ellipse horizontally) can reduce the asymmetric load and increase the onset angle. Typical results are shown in Figure 2.

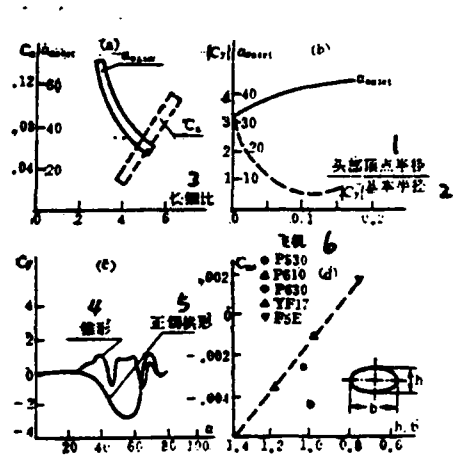

Figure 2. Effect of Nose Shape on Asymmetric Load

1. radius of nose tip
2. base radius
3. aspect ratio
4. cone
5. normal arch
6. aircraft

5. Rotating Nose Device

Reference [3] introduced the concept of rotating nose. A portion of the nose is rotating at a constant speed in a fixed direction around its axis to reduce or even eliminate the asymmetry in leeward flow. Experimental results pointed out that the asymmetric lateral force could be significantly reduced when the rotating speed is higher than 8 rev/sec. A schematic diagram of this rotating device and its typical results are shown in Figure 3. Its effect on the pitch moment is not very high.

6. Controlled Strake

Reference [8] introduced the concept of hinged strake. The strake is connected to the body by hinges. With varying angle of attack, the strake angle can vary symmetrically or asymmetrically according to a specific pattern to alleviate the deleterious effect caused by the breakdown of strake vortex to improve the aerodynamic properties of the strake. The results showed that it is possible to find a better reverse angle on the strake (-30° on both right and left strakes) so that the lateral force and yawing moment are essentially zero in the attack angle range of $0^{\circ}\sim40^{\circ}$ (See Figure 4a). In addition, the longitudinal characteristics are also improved. The experimental results show that asymmetric /114
yawing of the strakes can provide higher rolling moments (See Figure 4b). Therefore, using asymmetric strakes is an effective device for lateral force control of aircraft at high angle of attack.

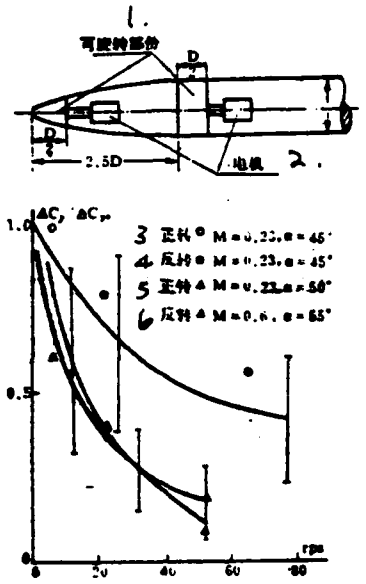

Figure 3. Schematic Diagram of Rotating Nose and Its Typical Results

1. rotating part
2. motor
3. forward
4. reverse
5. forward
6. reverse

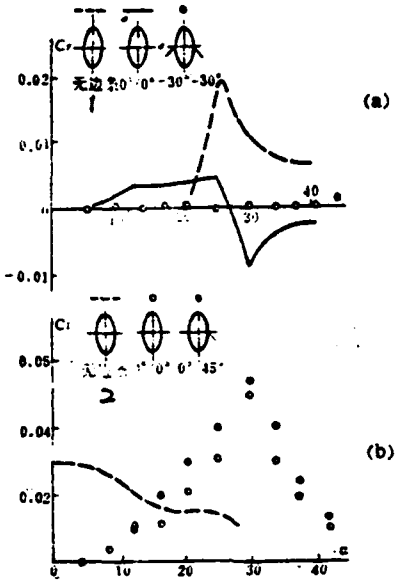

Figure 4. Typical Results of Asymmetric Strakes

1. without strake
2. without strake

7. Active Blowing Device

References [4], [9], [10] and [11] presented various schemes of blowing in various directions (along the surface tangentially downstream or upstream, blowing in normal direction) to destroy the asymmetric flow in the leeward region to make it symmetric. Thus, the asymmetric load is alleviated or eliminated. Or, its direction even changed. Figures 5a and b show the typical results

of normal blowing[4] and tangential blowing[10], respectively. The results show that blowing is very effective in alleviating asymmetric load. Reference [11] pointed out that the axial position of the nozzle should be placed as close to the nose as possible. The circumferential position of the nozzle should be at the onset of the separation vortex. Thus, the blowing efficiency can be improved.

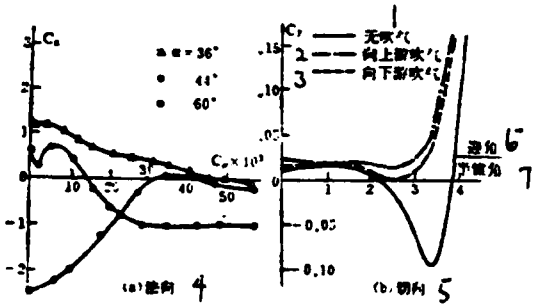

Figure 5. Typical Blowing Results

1. without blowing
2. blowing upstream
3. blowing downstream
4. normal direction
5. tangential direction
6. angle of attack
7. semi-conical angle

8. Comments

In the methods discussed above, the alleviation of asymmetric load by the nose transition strip, ring and fixed strake, and changing geometric shape of the nose cannot be automatically adjusted based on the flight condition. Therefore, they belong to the passive control category. These methods are relatively simple and effective in specific ranges. More studies are currently being conducted on these methods as well. Rotating nose, controlled strake and active blowing device can automatically be /115 changed based on different flight conditions. They belong to the active control category. These methods are more complex and are more difficult to realize. They are still in a research stage. A great deal of theoretical analyses and experimental work will be needed. The following specific problems must be addressed in performing experiments on active control systems at high attack angles in wind tunnels:

1. We must understand the correlation between the active control parameters and the asymmetric load in order to optimize the parameters of the active control device.

2. In the design and adjustment of the control system, we must resolve problems such as the selection of sensors and execution mechanism, determining the control law, and the design, fabrication and adjustment of the control circuit.

3. In terms of model design, because sensors and active control device must be installed on the model, model design is very difficult.

4. In formulating the experimental protocol, we should first consider the control with a single factor, test its feasibility and resolve all the technical problems. Then, we will consider the overall effect on the performance of the aircraft. In addition, after an active control device is added, the movement of the load and the control device becomes a dynamic problem. It is required to consider the dynamic effect of the model. In this case, rigid degree of freedom of the aircraft must be simulated.

In conclusion, active control of the asymmetric load at high angles of attack is a technically complicated but rewarding research subject. It is still in its infancy. It should attract people's attention for further exploration.

References

[1] Pick, G.S., J. Spacecraft 9, 6, 1971.

[2] Keener, E.R. et al., NASA TMX-3437 Feb. 1977.

[3] Fidler, J.E., AIAA Paper 80-182.

[4] Almosnino, D. et al., J. Spacecraft 18, 5, 1981.

[5] Yu Xinshi et al, SEcond Asian Fluid Dynamic Meeting Paper, 1983.

[6] Chapman, G.T. et al., AGARD CP-199, June, 1976.

[7] Keener, E.R., AIAA Paper 76-66.

[8] Rao, D.M., J. Aircraft 19, 4, 1982.

[9] Moss, G.F., AGARD CP-247.

[10] Peake, D.J., NASA TM 7802.

[11] Moore, W.A., AIAA Paper 80-173

DISTRIBUTION LIST

DISTRIBUTION DIRECT TO RECIPIENT

ORGANIZATION	MICROFICHE
A205 DMAHTC	1
A210 DMAAC	1
B344 DIA/RTS-2C	9
C043 USAMIIA	1
C500 TRADOC	1
C509 BALLISTIC RES LAB	1
C510 R&T LABS/AVRADCOM	1
C513 ARRADCOM	1
C535 AVRADCOM/TSARCOM	1
C539 TRASANA	1
C591 FSTC	4
C619 MIA REDSTONE	1
D008 NISC	1
E053 HQ USAF/INET	1
E404 AEDC/DOF	1
E408 AFWL	1
E410 AD/IND	1
E429 SD/IND	1
P005 DOE/ISA/DDI	1
P050 CIA/OCR/ADD/SD	2
AFIT/LDE	1
FTD	
CCN	1
NIA/PHS	1
LLNL/Code L-389	1
NASA/NST-44	1
NSA/1213/TDL	2
ASD/FTD/TQIA	1

END

1-87

DTIC